UNIVERSITY OF CINCINNATI

Date: 4 March 2009

I, Marshall Christopher Galbraith,

hereby submit this original work as part of the requirements for the degree of:

Master of Science

in Aerospace Engineering

It is entitled:

Implicit Large Eddy Simulation of Low-Reynolds-Number Transitional Flow Past the SD7003 Airfoil

Student Signature: Marshall C. Galbraith

This work and its defense approved by:

Committee Chair: Dr. Paul D. Orkwis

Dr. Mark G. Turner

Dr. Shaaban A. Abdallah

Dr. Miguel R. Visbal

Approval of the electronic document:

I have reviewed the Thesis/Dissertation in its final electronic format and certify that it is an accurate copy of the document reviewed and approved by the committee.

Committee Chair signature: Dr. Paul D. Orkwis

Implicit Large Eddy Simulation of Low-Reynolds-Number Transitional Flow Past the SD7003 Airfoil

by

Marshall Christopher Galbraith

B.S., University of Cincinnati, 2006

A thesis submitted to the

Faculty of Graduate School of the

University of Cincinnati

in partial fulfillment

of the requirements for the degree of

MASTERS OF SCIENCE

Department of Aerospace Engineering and Engineering Mechanics

of the College of Engineering

Committee Chair: Paul D. Orkwis

March 4, 2009

Abstract

A laminar separation bubble is known to be detrimental to the performance of airfoils operating at low Reynolds numbers ($Re < 10^5$). With increasing interest in Micro Air Vehicles (MAV), a clear understanding of the formation and subsequent turbulent breakdown of laminar separation bubbles is required for improved handling, stability, and endurance of MAV's. A computational investigation of flow past the SD7003 airfoil over the Reynolds number range $10^4 < Re < 9x10^4$ is presented. This airfoil was selected due to its robust laminar separating bubble and the availability of high-resolution experimental data. A high-order implicit large-eddy simulation (ILES) approach capable of capturing the laminar separation and subsequent three-dimensional breakdown is shown. The ILES methodology also predicts, without change in parameters, the passage into full airfoil stall at high incidence. In addition, computed separation, reattachment, and transition locations, as well as aerodynamic loads generally agree well with experimental data. Finally, a blowing/suction slot positioned near the leading edge was shown to energize the two-dimensional mode and reduced spanwise instabilities of the shear layer. This caused transition to occur further downstream and effectively eliminated the time mean laminar separation bubble.

Acknowledgements

The author extends his gratitude to a number of people at Computational Sciences Center of Wright Patterson Air Force Base (WPAFB). In particular, much gratitude is reserved for Dr. Donald Rizzetta and Dr. Philip Morgan for providing many hours of insight and guidance on how to use the FDL3DI flow solver effectively. Furthermore, the author thanks Dr. Scott Sherer for efforts to expand the overset capabilities of the FDL3DI solver. This thesis would not have been possible without his contributions to high order interpolation and grid decomposition.

Thanks are due for Dr. Michael Ol of WPAFB and Dr. Rolf Radespiel and Jan Windte of Technical University of Braunschweig for generously providing their experimental measurements for direct comparison. In particular, the author thanks Dr. Ol for his straightforward discussions of details regarding his experimental data.

Besides financial support through the cooperative education program at WPAFB, the author is grateful for, and honored by, the funding provided by fellowships from Ohio Space Grant Symposium and the American Institute of Aeronautics and Astronautics.

Appreciation is extended to members of the Gas Turbine Simulation Laboratory at the University of Cincinnati. Specifically, Michael List, Daniel Galbraith (my brother), and Jason Nimersheim contributed significantly with their wok on parallel post-processing and ray tracing visualization of Computational Fluid Dynamics (CFD) solutions.

Special recognition is reserved for Dr. Kirti N. Ghia and Dr. Urmila Ghia for introducing myself to the field of CFD my freshman year of college. It is thank to them that I have perused my current career and I have them to thank for keeping me on course. My advisors also deserve

recognition. It was Dr. Miguel Visbal whom suggested I use this project for a Masters thesis, and it was Dr. Paul Orkwis and Dr. Mark Turner whom gave me not only insight but also the freedom to complete this thesis. I must also thank Dr. Shaaban Abdallah for teaching me details of CFD that I will be using throughout my continued education.

Finally, I wish to thank my friends and family for their support over the years. I want to thank my father for always inspiring me and for introducing me to the field of Aerospace Engineering as a child, and I thank my mother for always looking out for me and my brother while keeping my feet firmly on the ground. I want them both to known that they have done their job well.

Table of Contents

List of Figures

List of Tables

List of Symbols

Symbol	Description
A	Disturbance amplitude
C	Chord length
C_L	Time- and spanwise-mean lift coefficient, $2\overline{L} / \rho_\infty U_\infty^2 C$
C_D	Time- and spanwise-mean drag coefficient, $2\overline{D} / \rho_\infty U_\infty^2 C$
Cp	Time- and spanwise-mean coefficient of pressure, $2(p_\infty - \overline{p}) / \rho_\infty U_\infty^2$
C_f	Time- and spanwise-mean skin friction coefficient, $2\frac{\mu}{\mathrm{Re}}\frac{\partial u}{\partial n}$
D	Drag
E_t	Total specific energy
F_I, G_I, H_I	Inviscid vector fluxes
F_v, G_v, H_v	Viscous vector fluxes
F^+	Non-dimensional frequency, $1/t = U_\infty / C$
H_k	Kinematic shape factor, δ^*/θ
I, J, K	Coordinate grid indices in the circumferential, surface normal, and spanwise directions
J	Jacobian of coordinate transformation
L	Lift
M	Reference Mach number
N_{crit}	Critical N-factor used by XFOIL to determine transition to turbulence
Pr	Prandtl number; 0.72 for air
Q	Vector of dependent variables
Re	Reference Reynolds number, $\rho_\infty U_\infty C / \mu_\infty$
T	Non-dimensional static temperature
U, V, W	Contravariant velocity components
U_∞	Freestream reference speed
U_t	Velocity tangential to the airfoil surface
U_e	Boundary layer edge velocity
X, Y, Z	Non-dimensional Cartesian coordinates
h_b	Maximum laminar separation bubble height
k	Heat transfer coefficient
n	Airfoil wall normal direction
p	Non- dimensional static pressure
q_i	Component of heat flux vector
s	Body fitted airfoil surface coordinate
t	Non-dimensional time C / U_∞
u, v, w	Non-dimensional Cartesian velocity components in x, y, z directions
$\overline{u'v'}$	Reynolds stress $\overline{uv} - \overline{u}\,\overline{v}$
x_s, x_t, x_r	Separation, transition, and reattachment locations

y^+	Non-dimensional boundary layer distance $\frac{Y}{\nu}\sqrt{\mathrm{Re}\frac{\tau_{wall}}{\rho}}$

Greek Symbol	Description
Δt	Non-dimensional time step
α	Angle of attack
α_f	Filter optimization parameter $\left(\left\|a_f\right\| < 0.5\right)$
γ	Specific heat ratio; 1.4 for air
δ	Kronecker delta function
δ^*	Boundary layer displacement thickness
δ_{995}	Boundary layer thickness based on 99.5% of U_e
$\delta_{\xi 2}$, $\delta_{\eta 2}$, $\delta_{\zeta 2}$	Second- and sixth-order finite difference operators in ξ, η, and ζ directions
$\delta_{\xi 6}$, $\delta_{\eta 6}$, $\delta_{\zeta 6}$	
θ	Boundary layer momentum thickness
μ	Non-dimensional molecular viscosity coefficient
ν	Non-dimensional kinematic viscosity coefficient μ / ρ
ξ, η, ζ	Computational coordinates
ξ_t, ξ_x, ξ_y, ξ_z,	Metric coefficients of the coordinate transformation
η_t, η_x, η_y, η_z,	
ζ_t, ζ_x, ζ_y, ζ_z	
ρ	Non-dimensional density
τ	Shear stress
ϕ	Generic scalar quantity
ϕ'	Derivative of ϕ
$\overline{\phi}$	Filtered ϕ

Subscripts	Description
∞	Freestream reference conditions
wall	Solid wall quantities
max	Maximum value of a computational coordinate

Superscripts	Description
–	Time- and spanwise-mean quantities
‘	Fluctuating components

Operators	Description
∇^2	Laplace Operator

1 Introduction

Low Reynolds flow has been of interest for model airplane designers for decades. As a result, a large database of experimental and numerical data for fixed wing airfoils has been compiled. Several investigators, such as F. Schmitz[1], R. Eppler[2], and S. Selig[3], have contributed with a vast number of experimental measurements and advanced aerodynamic design methodologies. Interest for developing small Unmanned Air Vehicles, including Micro Air Vehicles (MAV), capable of performing a wide range of missions has grown in recent years with the development of micro system technologies, such as batteries and sensors. Due to their small size and low air speed, these vehicles typically operate at a Reynolds number on the order of 10^4 to 10^5. At these low Reynolds numbers, the flow may remain laminar over a significant portion of the airfoil rendering it susceptible to separation from even mild adverse pressure gradients. For moderate incidence, separation leads to the formation of a closed laminar separation bubble (LSB) which reattaches through transition into turbulence. The LSB moves toward the leading edge with increasing angle of attack and shortens in streamwise extent. Eventually, as the stall angle is exceeded, the turbulent flow is unable to reattach the flow and bubble bursting ensues. The onset and successive breakdown of the LSB at low Reynolds numbers is known to be detrimental to the performance, endurance, and stability of MAV's.

The first investigation into the behavior of LSB's was conducted by Sir Melvill Jones[4] in the 1930's. Early studies concentrated on how one or more of the parameters such as angle of attack, Reynolds number, surface roughness, and freestream turbulence level affect bubble characteristics and length.[5–11] General features of a time-mean two-dimensional transitional separation bubble are given in Figure 1.1. A separation bubble is formed when a sufficient adverse pressure gradient causes the laminar boundary layer to separate. Downstream of the

separation location, the time-mean flow can be roughly divided into two regions. The bubble is formed below a dividing streamline as a relatively slow recirculating region. The region above the reversed flow of the recirculation region, bounded by the boundary layer edge, is a free shear layer. This shear layer undergoes a transition due to disturbance amplifications in the unstable laminar layer. The subsequent turbulent flow entrains high momentum fluid causing the free shear layer to reattach to the airfoil and the separation bubble to close in the time-mean. A turbulent boundary layer continues to develop downstream of the reattachment. Increasing either angle of attack or Reynolds number will move the transition location further upstream, hence diminishing both streamwise extent and height of the separation bubble. At a critical Reynolds number, the transition location will coincide with the separation location and the formation of a bubble is prevented through turbulent mixing. This critical Reynolds number is dependent on many factors such as adverse pressure gradient, surface roughness, freestream turbulence, acoustic noise, etc. In fact, passive flow control techniques typically rely on increasing surface roughness upstream of the separation to induce turbulent mixing and thereby eliminate the separated flow.

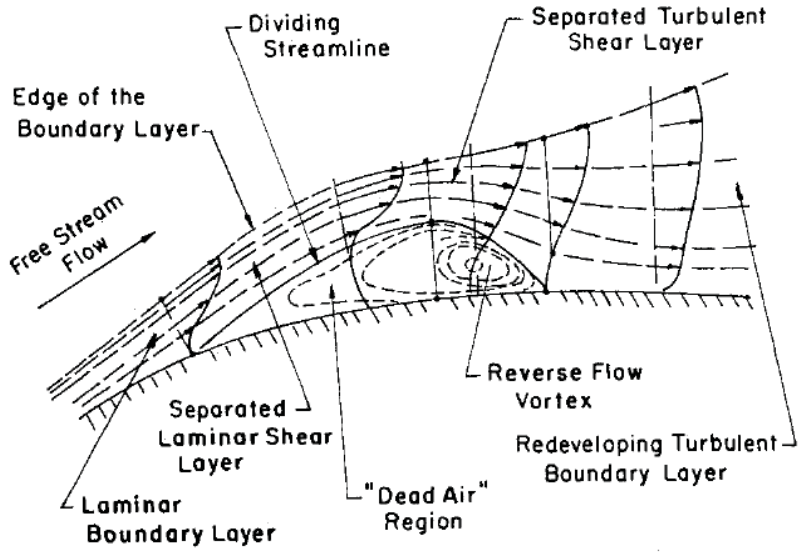

Figure 1.1: Time-mean flow field about a transitional laminar separation bubble[12]

Separation bubbles have been classified as either short or long. Short bubbles only extend a few percent of the chord and have little overall effect on the flow field. Such bubbles do not drastically influence the flow over the airfoil, hence lift and drag can typically be approximated reasonably well with inviscid calculations. Furthermore, several empirical methods for predicting separation and reattachment locations exist that are only valid for small separation bubbles.[12] Conversely, long bubbles exhibit a pressure distribution that inviscid theory is unable to predict. As illustrated in Figure 1.2, the pressure distribution measured from a long separation bubble exhibits a lower pressure peak, a characteristic pressure plateau between separation and transition locations, and a relatively sharp pressure recovery to the inviscid prediction at the reattachment point. Relative to inviscid theory, the pressure distribution resulting from the long bubble leads to drastically different airfoil lift, drag, and pitching moment characteristics. As a result, aircraft scaled down to lower Reynolds numbers may exhibit a notably altered behavior compared with their higher Reynolds numbers counterpart where viscous effects may be less influential.

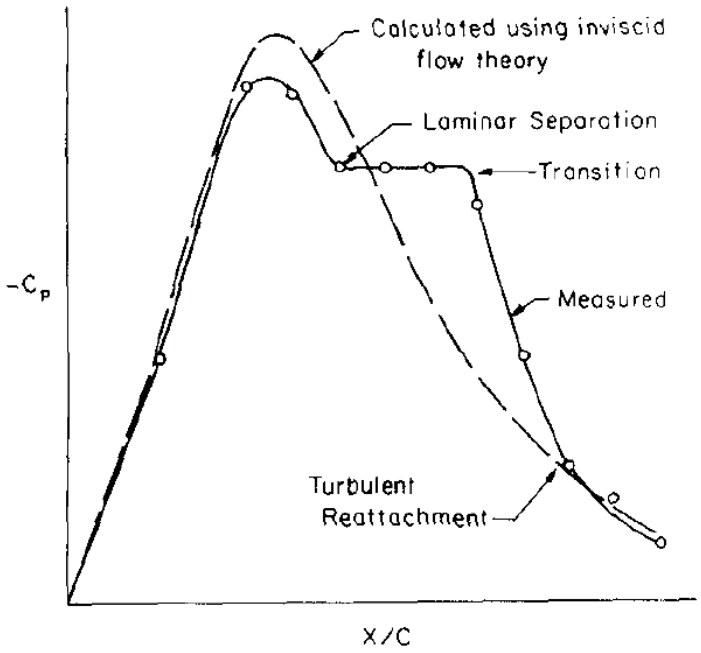

Figure 1.2: Charachteristic pressure plateu of a long laminar separation bubble[13]

1.1 Previous Calculations of Laminar Separation Bubbles on Airfoils

One of the first two-dimensional laminar solutions of the Navier-Stokes equations over an airfoil at near stall conditions was obtained by Hodge et al.[14] Although this work focused on automated curvilinear grid generation, it illustrated some key issues when computing separated low Reynolds number laminar flow. Hodge et al. obtained a solution for the NACA 6412 airfoil at 10° angle of attack and Reynolds number 4.14×10^4. The computations predicted a highly unsteady flow with relatively large spanwise vortices forming on the suction surface of the airfoil and traversing downstream. Streamlines revealed that these vortical structures did not dissipate until they reached the coarser region of the mesh in the wake where grid resolution was inadequate to resolve them. Unfortunately, time-mean quantities were not computed for comparison with experimental measurements. However, instantaneous streamlines indicated a larger separated region than observed in the experimental smoke visualization.[15] In addition, the large shedding vortices were not observed in the experiment. Rather, experimental smoke lines blurred downstream of the separation as a result of transition into turbulence. Instead of capturing the turbulent breakdown of the shear layer, two-dimensional computations tend to over predict the coherency of spanwise vortices as they do not inherently account for vortex stretching and spanwise instabilities that breakdown the vortex. While the Navier-stokes equations are capable of modeling turbulence directly, grid resolution requirements for such three-dimensional Direct Numerical Simulations (DNS) are prohibitive for practical applications.

To improve the accuracy of two-dimensional transitional flow simulations, researchers have coupled Reynolds Averaged Navier-Stokes (RANS) solvers with turbulence transition models. A laminar separation is typically obtained by suppressing the turbulence model upstream of the transition location predicted by the transition model. Downstream of the transition location, the

turbulence model is responsible for producing the pressure rise as well as boundary layer thickening and reattachment. This coupling method requires both accurate transition and turbulence models to achieve a physically representative solution. Much research has been dedicated to both areas over the past decades.

As transition is affected by a wide range of parameters such as wall roughness, freestream turbulence, pressure gradient, acoustic noise, etc., a comprehensive transition model that accounts for all factors has not been developed in the literature. Instead, transition is typically predicted with models that only consider one or two parameters. For example, the first transition model was conceived by Von Doenhoff.[16] Von Doenhoff assumed that the boundary layer separated along a tangential path and that transition takes place at a constant Reynolds number based on the distance from the separation. Furthermore, it was assumed that the turbulence spread out at a constant wedge angle; which permitted the reattachment location to be determined using simple geometric relationships. Unfortunately, this simple model was only valid in a few cases and is generally not applicable.

Transition models range from simple empirical methods based on linear stability theories, to linear or non-linear parabolized stability equations, and finally more comprehensive Navier-Stokes models. A design-oriented approach adapted by many researchers is the e^N method[17, 18] which is based on linear stability analysis and boundary layer theory. Here, local growth rates of unstable waves based on velocity profiles are evaluated by solving the Orr-Sommerfeld equation. Transition is assumed to occur when the amplification of the most unstable Tollmien-Schlichting waves reach a specified critical threshold; known as the critical N-factor. This method is used, for instance, to predict transition location in the popular airfoil-design code XFOIL[19].

Coupling of a RANS solver and transition model was first archived by Hegna[20]. Incompressible Reynolds Averaged Navier-Stokes equations were solved with an algebraic eddy viscosity turbulence model for the NACA 0012 airfoil at a chord Reynolds number of 1.7×10^5. The turbulence model incorporated modifications to account for separated adverse pressure gradient flows. Prediction of the transition location was achieved through a transition model developed by Green et al.[21] Despite limited computational resources, Hegna was able to obtain solutions that agreed favorably with available experimental data. However, these experiments did not exhibit a strong adverse pressure gradient or a significant pressure plateau. In addition, solutions were not obtained in post stall conditions.

More recently, Radespiel et al.[22], Lian and Shyy[23], and Yuan et al.[24] successfully coupled modern RANS solvers, equipped with a number of turbulence models, with the e^N method to predict laminar to turbulent transition on low Reynolds number airfoils. While the RANS-e^N solutions were dependent on both critical N-factors for the transition model and the choice of turbulence model, the method has been shown capable of accurately capturing the time-mean LSB up to stall. Post stall calculations tended to over predict the lift and drag of the airfoil.[23] However, because the post stall flow does not undergo a traditional laminar separation and transition process, the discrepancy in lift and drag is related to the turbulence model rather than the transition and turbulence coupling technique.

While this technique of coupling transition and turbulence models is computationally efficient; it is limited by its inherent assumptions of two-dimensional parallel steady velocity profiles and thin boundary layers. These limitations are acceptable in many situations (particularly for airfoil-design purposes); however full three-dimensional MAV configuration

analysis is beyond the scope of such approaches. Even though the e^N method has been extended to three-dimensions, a physical interpretation of the method in this situation is unclear[25]. The flow field over a low Reynolds number finite wing incorporates a number of additional features not present when analyzing a two-dimensional airfoil. As shown in the sketch in Figure 1.3, a finite wing not only exhibits a three-dimensional laminar separation region, additional complexity is introduced by the tip vortices. Furthermore, for MAV's with flapping motions, high angle of attack excursions may promote the development of leading-edge dynamic stall and leading-edge vortices whose stability falls outside of the aforementioned transition prediction framework. Due to current limitations associated with the transition and turbulence modeling techniques, it is imperative that other solution methods are explored. Such methods could provide alternative solution techniques and/or additional insights to improve transition and turbulence modeling techniques.

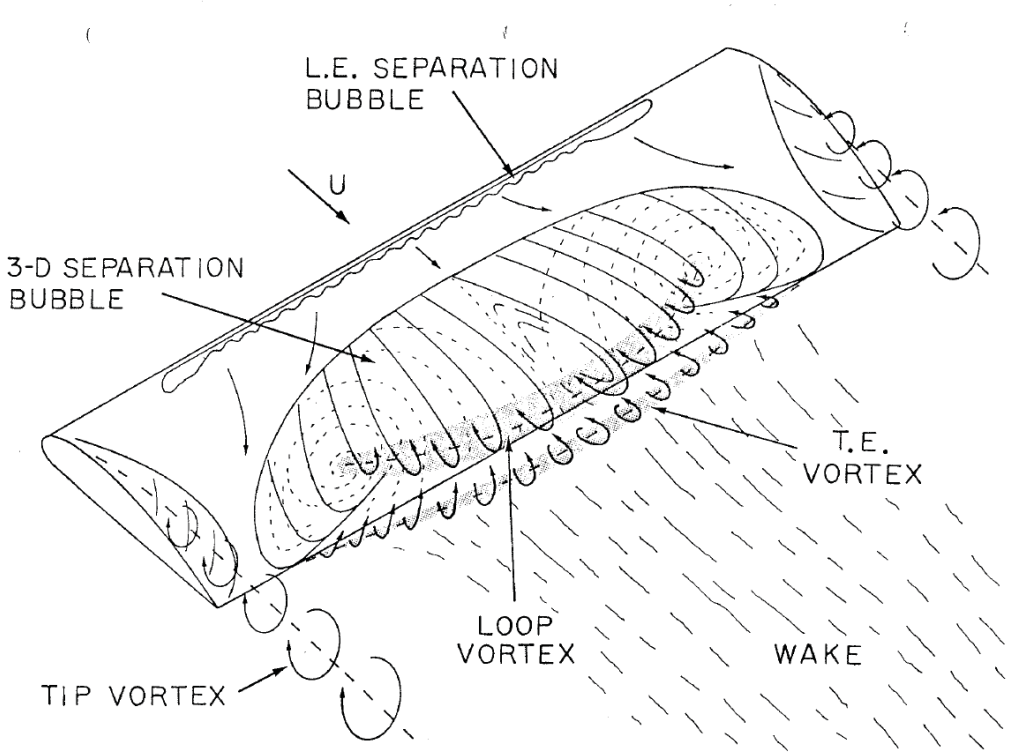

Figure 1.3: Model of laminar separation on a finite wing[26]

1.2 Present Computations

The present work investigates the feasibility of an Implicit Large-Eddy Simulation (ILES) approach to predict LSB formation and transition for low Reynolds–number airfoil applications. This technique solves the Navier-Stokes equations without the addition of a turbulence model. Hence, it relies on grid resolution to capture the relevant flow physics, such as separation, transition, and closure of the LSB. The ILES approach, previously introduced in Refs. 27 and 28, is based on higher-order compact schemes for the spatial derivatives and a Pade-type low-pass filter to provide stability. The high-order scheme allows for accurate capturing of the separation and transition process, whereas the highly-discriminating low-pass filter is used in lieu of a standard sub-grid-scale (SGS) model to enforce regularization in turbulent regions. This approach is very appealing as it provides a seamless methodology for mixed laminar, transitional, and turbulent three-dimensional flows. A re-interpretation of this ILES approach in the context of an Approximate Deconvolution Model[29] has been provided by Mathew et al.[30].

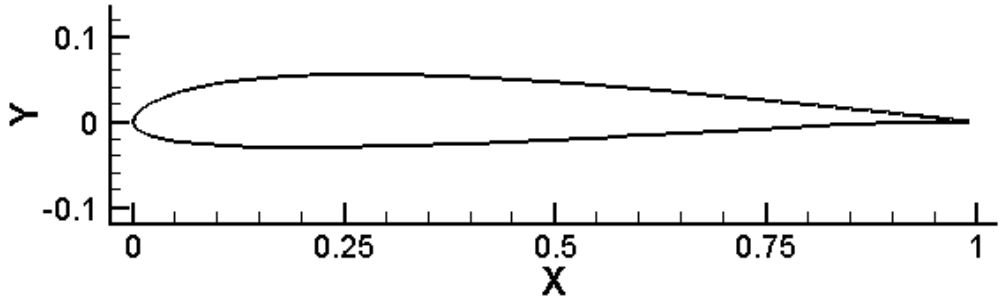

Figure 1.4: The SD7003 airfoil.

Results are presented for flow over a SD7003 airfoil section[31], shown in Figure 1.4. This airfoil has a maximum thickness and camber of 8.5% and 1.48% respectively. The SD7003 airfoil was chosen due to the relatively large LSB that forms on the suction side of the airfoil at low Reynolds numbers and the available high quality experimental Particle Image Velocimetry (PIV) data for comparison. High resolution velocity and Reynolds stress measurements have

been provided by Radespiel[22]. Experiments were conducted in a water channel, as well as a low-noise wind tunnel at the Technical University of Braunschweig (TU-BS). Freestream turbulence intensities were 0.08% and 0.8% for the wind tunnel and water channel respectively. Measurements are available for Reynolds number $6x10^4$ at 4° angle of attack in the wind tunnel, and at 8° and 11° in the water channel. PIV measurements for the SD7003 airfoil were also obtained by Ol et al.[32] at the Wright Patterson Air Force Base (WPAFB) water channel with a freestream turbulence intensity of less than 0.1%. Aerodynamic load measurements are also available from Ol et al.[32] and Selig et al.[33, 34]

Due to the adverse affect that LSB's have on airfoil performance, a limited investigation was performed to assess the sensitivity of the shear layer to a leading edge disturbance. The disturbance was introduced as zero-net-mass-flow blowing/suction slot near the leading edge driven at a frequency near the dominant natural frequency of the shear layer. Despite the small amplitude of the disturbance, 1% of the freestream velocity, the disturbance was able to effectively eliminate the LSB in the time-mean sense. However, rather than tripping the flow to turbulence, the leading edge disturbance energized the two-dimensional mode of the shear layer and reduced spanwise instabilities which in turn delayed the transition into turbulence.

Chapter 2 describes the solution methodology, including the numerical code FDL3DI used to obtain ILES solutions. The mesh and boundary conditions used for the computations are described in Chapter 3. Chapter 4 discusses numerical considerations regarding spatial discretization, spanwise extent of the computational domain, and reference Mach number. A comparison between the computed solutions and experimental measurements is given in Chapter 5. In addition, the effects of both Reynolds number and angle of attack are investigated in this chapter. To end this chapter, the sensitivity of the separated shear layer to the small leading edge

disturbance is investigated. Finally, Chapter 6 summarizes the key findings of this work and presents recommendations for future research.

2 Solution Methodology

Current computations utilize the flow solver FDL3DI, a higher-order accurate, parallel, Chimera, Implicit/SGS Large Eddy Simulation solver from Wright Patterson Air Force Base. FDL3DI has been proven reliable for many steady and unsteady fluid flow problems.[35–41] The following sections will describe the underlying methodologies of this solver.

2.1 Implicit vs. Subgrid-Scale Model LES

The underlying concept of LES simulations assumes that flow structures can be separated into two categories, large scale eddies which are generated by geometry, and small scale dissipative eddies. It is assumed that the large scale structures carry a majority of the Reynolds stresses and therefore must be computed directly. Conversely, the small scale eddies are weaker, contribute less to the Reynolds stresses, and are therefore less critical. In addition, the small scales are nearly isotropic with universal characteristics lending them to modeling. Thus, a traditional LES simulation relies on so called sub-grid scale models to capture the effect of small scale eddies that are under-resolved by the computational mesh. These models are incorporated as additional terms in the Navier-Stokes equations much like the source terms in RANS equations. Unlike the RANS equations, the SGS terms are obtained through a filtering process rather than an averaging process. The first SGS model was conceived by Smagorinsky[42] in 1963 and is commonly used for LES calculations due to its relative simplicity. Another commonly used model is the dynamic SGS model where the coefficient in the original Smagorinsky is updated with the solution.[43]

In an Implicit LES scheme, unlike the traditional LES approach, no additional subgrid-scale terms are appended to the governing Navier-Stokes equations. Instead, a high-order low-pass filter operator serves to incorporate the additional dissipation associated with the under-resolved eddies. In other words, the filtering process is applied numerically to the computed solution during each time step rather than analytically to the Navier-Stokes equations. This filtering procedure has produced accurate results for several turbulent flows on LES level grids, and provides an attractive alternative to the use of standard sub-grid-scale models. For example, Visbal and Rizzetta[27] used a 6^{th}-order compact scheme with a 10^{th}-order filter to simulate an isotropic decaying turbulent flow both with and without a Smagorinsky or dynamic SGS model. Time histories of the turbulent kinetic energy of these computations are compared with spectral DNS calculations of Spyropoulos and Blaisdell[44] in Figure 2.1. The 6^{th}-order compact scheme required filtering both with and without the SGS model to maintain numerical stability. However, the computation without an SGS model tracks the turbulent decay remarkably well considering that the mesh consists of 32^3 points as compared with the DNS calculation with 128^3 points. However, the addition of an SGS model introduced excess dissipation. This excess dissipation stems from the SGS model's inability to discriminate between resolved and under-resolved scales.[45] While the higher-order filter only filters out the under-resolved high wave numbers, the SGS models have a tendency to dissipate energy over a wide range of wave numbers. This deficit in SGS models is inherit in the approach and cannot be corrected by adjusting the constant in the models. Besides the favorable results, computations without the SGS model are significantly less intensive as the SGS models require the evaluation of numerous additional derivatives.

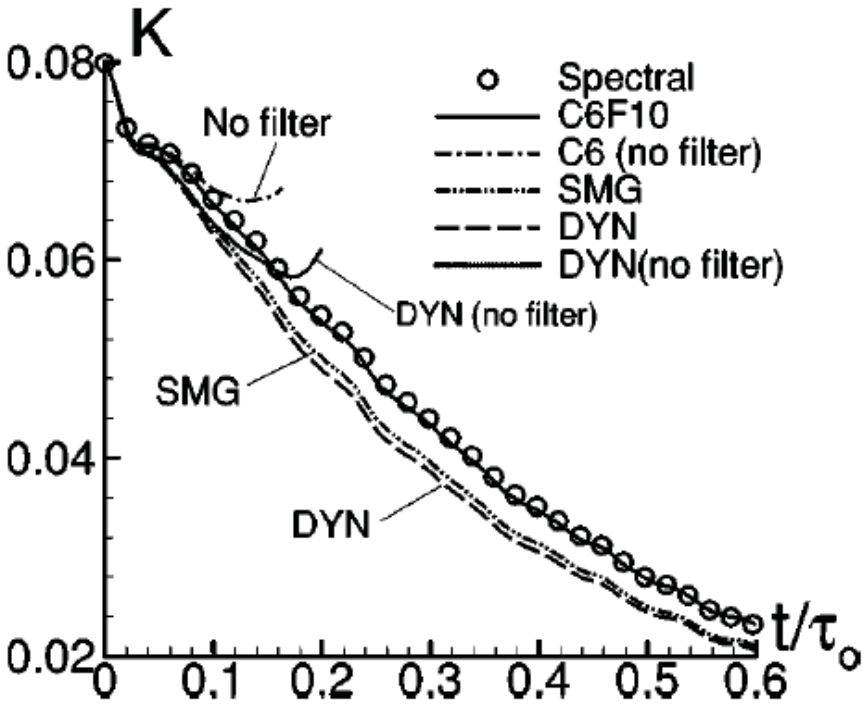

Figure 2.1: Time history of turbulent kinetic energy for a decaying isotropic turbulence using serveral SGS models (32^3 mesh)[27]

The higher-order scheme costs approximately twice that of an explicit 2nd-order scheme in terms of CPU time per grid point per time step. However, a mesh size of 128^3 is required to achieve the same results shown in Figure 2.1 with a 2nd-order explicit scheme.[27] This is an increase in computational cost of approximately 32 times over the compact scheme. Thus the compact scheme with the higher-order filter has the promise of both accuracy and computational efficiency. The ILES technique has been incorporated into the FDL3DI flow solver and applied to a range of complex flow problems such as turbulent channel flow[39], laminar separation over a low pressure turbine blade[35], vortex breakdown over a delta wing[37], and a full UAV1303 model[41].

2.2 Governing Equations

The FDL3DI code solves the three-dimensional, unsteady, unfiltered, compressible Navier-Stokes equations expressed in curvilinear coordinates

$$\frac{\partial Q}{\partial t}+\frac{\partial F_I}{\partial \xi}+\frac{\partial G_I}{\partial \eta}+\frac{\partial H_I}{\partial \zeta}=\frac{1}{\mathrm{Re}}\left[\frac{\partial F_v}{\partial \xi}+\frac{\partial G_v}{\partial \eta}+\frac{\partial H_v}{\partial \zeta}\right] \tag{2.1}$$

where the vector of dependent variables is expressed as

$$Q=\frac{1}{J}\left[\rho \quad \rho u \quad \rho v \quad \rho w \quad \rho E_t\right]^T \tag{2.2}$$

The inviscid flux vectors are

$$F_I=\frac{1}{J}\begin{bmatrix}\rho U\\ \rho uU+\xi_x p\\ \rho vU+\xi_y p\\ \rho wU+\xi_z p\\ \rho E_t U+p\widetilde{U}\end{bmatrix},\ G_I=\frac{1}{J}\begin{bmatrix}\rho V\\ \rho uV+\eta_x p\\ \rho vV+\eta_y p\\ \rho wV+\eta_z p\\ \rho E_t V+p\widetilde{V}\end{bmatrix},\ H_I=\frac{1}{J}\begin{bmatrix}\rho W\\ \rho uW+\zeta_x p\\ \rho vW+\zeta_y p\\ \rho wW+\zeta_z p\\ \rho E_t W+p\widetilde{W}\end{bmatrix} \tag{2.3}$$

where

$$\begin{aligned}U&=\xi_t+\xi_x u+\xi_y v+\xi_z w=\xi_t+\widetilde{U}\\ V&=\eta_t+\eta_x u+\eta_y v+\eta_z w=\eta_t+\widetilde{V}\\ W&=\zeta_t+\zeta_x u+\zeta_y v+\zeta_z w=\eta_t+\widetilde{W}\\ E_t&=\frac{T}{(\gamma-1)M_\infty^2}+\frac{1}{2}\left(u^2+v^2+w^2\right)\end{aligned} \tag{2.4}$$

The viscous flux vectors are

$$F_v = \frac{1}{J}\begin{bmatrix} 0 \\ \xi_{x_i}\tau_{i1} \\ \xi_{x_i}\tau_{i2} \\ \xi_{x_i}\tau_{i3} \\ \xi_{x_i} b_i \end{bmatrix},\ G_v = \frac{1}{J}\begin{bmatrix} 0 \\ \eta_{x_i}\tau_{i1} \\ \eta_{x_i}\tau_{i2} \\ \eta_{x_i}\tau_{i3} \\ \eta_{x_i} b_i \end{bmatrix},\ H_v = \frac{1}{J}\begin{bmatrix} 0 \\ \zeta_{x_i}\tau_{i1} \\ \zeta_{x_i}\tau_{i2} \\ \zeta_{x_i}\tau_{i3} \\ \zeta_{x_i} b_i \end{bmatrix} \tag{2.5}$$

where

$$\begin{aligned} \tau_{ij} &= \mu\left(\frac{\partial\xi_k}{\partial x_j}\frac{\partial u_i}{\partial\xi_k} + \frac{\partial\xi_k}{\partial x_i}\frac{\partial u_j}{\partial\xi_k}\right) - \frac{2}{3}\mu\delta_{ij}\frac{\partial\xi_l}{\partial x_k}\frac{\partial u_k}{\partial\xi_l} \\ b_i &= u_j\tau_{ij} + \frac{k}{(\gamma-1)\Pr M_\infty^2}\frac{\partial\xi_l}{\partial x_i}\frac{\partial T}{\partial\xi_l} \end{aligned} \tag{2.6}$$

Compact notation x_i, i = 1, 2, 3 is used to represent x, y, and z coordinates respectively and similarly ξ_i, for ξ, η, and ζ. Dependent variables have been non-dimensionalized by their respective reference values, except for pressure which was non-dimensionalized by $\rho_\infty U_\infty^2$. All length scales are non-dimensionalized by the chord length of the airfoil. This choice of non-dimensionalization infers that time and total energy were non-dimensionalized by C/U_∞ and U_∞^2 respectively. Sutherland's law for molecular viscosity

$$\mu = T^{3/2}\left(\frac{1+S_1}{T+S_1}\right),\ S_1 = 0.38 \tag{2.7}$$

as well as the perfect gas law

$$p = \frac{\rho T}{\gamma M_\infty^2} \tag{2.8}$$

are used to close the Navier-Stokes equations. It should be noted that the above governing equations correspond to the original *unfiltered* Navier-Stokes equations, and are solved without change in laminar, transitional, or fully turbulent regions of the flow.

2.3 Numerical Discretization

2.3.1 Time Integration

Time accurate solutions of Eq. 2.1 are obtained with the implicit approximate-factorization algorithm of Beam and Warming[46] augmented with Newton-like subiterations to achieve second order time accuracy. The implicit system is written in delta form as

$$\begin{aligned}
&\left[\left(\frac{1}{J}\right)^{p+1} + \phi^i \Delta t \delta_{\xi 2}\left(\frac{\partial F_I^p}{\partial Q} - \frac{1}{\mathrm{Re}}\frac{\partial F_v^p}{\partial Q}\right)\right] J^{p+1} \\
&\times\left[\left(\frac{1}{J}\right)^{p+1} + \phi^i \Delta t \delta_{\eta 2}\left(\frac{\partial G_I^p}{\partial Q} - \frac{1}{\mathrm{Re}}\frac{\partial G_v^p}{\partial Q}\right)\right] J^{p+1} \\
&\times\left[\left(\frac{1}{J}\right)^{p+1} + \phi^i \Delta t \delta_{\zeta 2}\left(\frac{\partial H_I^p}{\partial Q} - \frac{1}{\mathrm{Re}}\frac{\partial H_v^p}{\partial Q}\right)\right] \Delta Q \\
&= -\phi^i \Delta t\left[\left(\frac{1}{J}\right)^{p+1} \frac{(1+\phi)Q^p - (1+2\phi)Q^n + \phi Q^{n-1}}{\Delta t} + Q^p\left(\frac{1}{J}\right)_t^p\right. \\
&\left. + \delta_{\xi 6}\left(F_I^p - \frac{1}{\mathrm{Re}}F_v^p\right) + \delta_{\eta 6}\left(G_I^p - \frac{1}{\mathrm{Re}}G_v^p\right) + \delta_{\zeta 6}\left(H_I^p - \frac{1}{\mathrm{Re}}H_v^p\right)\right]
\end{aligned} \tag{2.9}$$

where

$$\phi^i = (1+\phi)^{-1},\ \Delta Q = Q^{p+1} - Q^p \tag{2.10}$$

Here, at the n + 1 time level, Q^{n+1} is approximated by $Q^{p+1} = \Delta Q + Q^p$. For p = 1, $Q^p = Q^n$. First order Euler-implicit and 2nd-order three-point backward schemes are given by setting $\phi = 0$ and $\phi = 1/2$ respectively. The 2nd-order accurate formulation was used for the present computations. The implicit left-hand side of the algorithm is discretized with 2nd-order

central differencing for all spatial derivatives and utilizes non-linear artificial dissipation to augment stability.[47] The efficiency of the implicit algorithm was increased by solving the factorized equations in diagonal form.[48] In order to maintain temporal accuracy, which can be degraded by the diagonal form, three sub-iterations were utilized within a time step. This technique is commonly used to reduce errors due to linearization, factorization, and explicit application of boundary conditions. This implicit time marching scheme has been successfully applied to unsteady vortical flow by Visbal and Gaitonde[49].

2.3.2 Spatial Discretization

The right-hand side of Eq. 2.9 is discretized with a 6th-order accurate compact scheme based on the pentadiagonal system of Lele[50] and is capable of obtaining spectral-like resolution. The method is described using a one-dimensional computational mesh consisting of N points with unit spacing as shown in Figure 2.2. For body fitted meshes, a coordinate transformation $\xi = \xi(x)$ is required to cast the physical coordinates into computational mesh coordinates. Furthermore, let $\phi = \phi(\xi)$ be a scalar quantity known at the point location as ϕ_j, $j \in [1, N]$. A stencil of five points is required in order to achieve a 6th-order accurate central compact scheme. Because the interior stencil can be utilized up to the third point off the boundary, special treatment is required at the first two boundary points. A limited description of the discretization of interior and boundary points implemented in FDL3DI is given in the following two sections. Detailed descriptions and additional compact schemes are referred to Ref. 51.

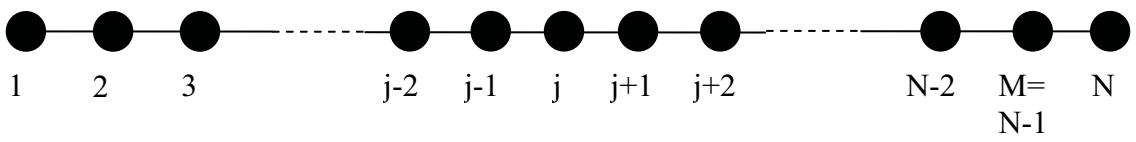

Figure 2.2: Notation for interior and boundary points

2.3.2.1 Interior Points

In general, the interior central differentiation formulation can be expressed as

$$\alpha\phi'_{j-1} + \phi'_j + \alpha\phi'_{j+1} = a\left(\frac{\phi_{j+1} - \phi_{j-1}}{2}\right) + b\left(\frac{\phi_{j+2} - \phi_{j-2}}{4}\right) \tag{2.11}$$

where ϕ'_j is the derivative of ϕ at point j and α, a, and b are constants that determine the order of accuracy of the scheme. To choose the appropriate coefficients, Taylor series approximations about point j are inserted into Eq. 2.11 and terms of appropriate order are set to zero. This leads to the following three equations[50]

$$\begin{aligned} O(h^2): &\quad 1 - a + 2\alpha - b = 0 \\ O(h^4): &\quad -a + 6\alpha - 4b = 0 \\ O(h^6): &\quad -a + 10\alpha - 16b = 0 \end{aligned} \tag{2.12}$$

Solutions to this system of equations can lead to both explicit and compact schemes. By setting α = 0, the left hand side of Eq. 2.11 is decoupled yielding an explicit expression for the derivative at point j. With this choice, two explicit schemes are obtained by determining a and b from the first two equations of Eq. 2.12. If only the first equation of Eq. 2.12 is solved with α = 0 and b = 0, an explicit 2nd-order scheme is obtained. Solving the first two equations gives an explicit 4th-order scheme. Thus the order of the scheme is one less than the number of stencil points.

Alternatively, allowing α ≠ 0 couples the derivative at point j with its neighbors on the left hand side of Eq. 2.12. This coupling of derivatives produces a tri-diagonal system that must be solved to implicitly obtain the derivatives. With the assumption of α ≠ 0, solving the first two equations of Eq. 2.12 with b = 0 yields a 4th-order compact scheme while the solution to all three equations leads to a 6th-order compact scheme. The term 'compact scheme' refers to the fact that

the scheme is one order higher than the number of stencil points. Higher than 6^{th}-order compact schemes can be derived but would require additional stencil points on either side of the Eq. 2.11.

A summary of the coefficients for both explicit and compact schemes is given in Table 2.1. Here, E2 and E4 stand for explicit 2^{nd} and 4^{th}-order accurate schemes respectively, while C4 and C6 represent compact 4^{th} and 6^{th}-order accurate schemes.

Table 2.1: Coefficients for interior compact finite differentiation

Scheme	α	a	b	Stencil Size	$O(h^*)$
E2	0	1	0	3	2
E4	0	$\frac{4}{3}$	$\frac{-1}{3}$	5	4
C4	$\frac{1}{4}$	$\frac{3}{2}$	0	3	4
C6	$\frac{1}{3}$	$\frac{14}{9}$	$\frac{1}{9}$	5	6

A wave number analysis reveals insight to which wave numbers are resolved by the differencing schemes in Table 2.1. To derive the equation for the modified wave number of the differencing schemes, a periodic Fourier expansion of ϕ is introduced at point *j*, expressed as

$$\widetilde{\phi}(x) = \sum_{k=0} b_k \exp\left(\frac{2\pi i k x}{L}\right), \text{ where } 0 \le x \le L, \quad i = \sqrt{-1} \tag{2.13}$$

By defining the scaled wave number

$$\omega = \frac{2\pi i k x}{L} \tag{2.14}$$

and the scaled wave coordinate

$$s = \frac{x}{\Delta x} \tag{2.15}$$

the Fourier expansion in Eq. 2.13 is rewritten as

$$\widetilde{\phi}(s) = \sum_{k=0} b_k e^{i\omega s} \tag{2.16}$$

Furthermore, the exact derivative of the Fourier expansion is given by

$$\widetilde{\phi}'(s) = \frac{d}{ds}\widetilde{\phi}(s) = \sum_{k=0} i\omega b_k e^{i\omega s} \tag{2.17}$$

In other words, the expansion coefficients of the derivative are given by

$$b_k' = i\omega b_k \tag{2.18}$$

To obtain the modified wave number, the Fourier expansion and is derivative are substituted into Eq. 2.11

$$\alpha\widetilde{\phi}'(-1) + \widetilde{\phi}'(0) + \alpha\widetilde{\phi}'(1) = a\left(\frac{\widetilde{\phi}(1) - \widetilde{\phi}(-1)}{2}\right) + b\left(\frac{\widetilde{\phi}(2) - \widetilde{\phi}(-2)}{4}\right) \tag{2.19}$$

After algebraic manipulation, the differencing schemes yields an approximation to the coefficients of the derivates as

$$b_k' = i\omega' b_k \tag{2.20}$$

where ω' is the modified wave number given by

$$\omega'(\omega) = \frac{a\sin(\omega) + (b/2)\sin(2\omega)}{1 + 2\alpha\cos(\omega)} \tag{2.21}$$

The modified wave numbers for the differencing schemes are shown in Figure 2.3. The extent to which the modified wave number follows the exact line is an indication of the wave numbers resolved by the differencing scheme. Increased order of accuracy of the differencing

scheme leads to a resolution of higher wave numbers. Wave numbers associated with the modified wave numbers that deviate from the exact line are under-resolved and can introduce phase errors which lead to dispersion.

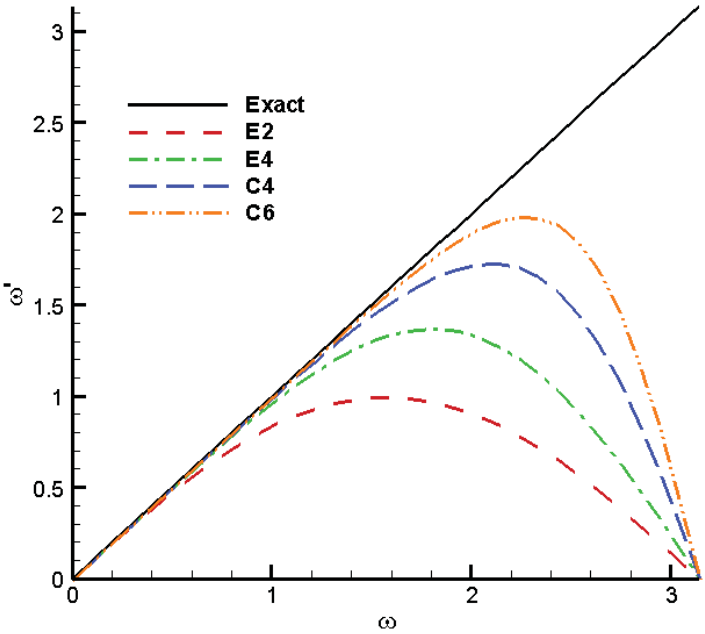

Figure 2.3: Modified wave number for finite difference schemes

2.3.2.2 Boundary Points

To preserve the tridiagonal nature of the interior scheme, the general equation for the first boundary point is

$$\phi_1' + \alpha_1\phi_2' = a_1\phi_1 + b_1\phi_2 + c_1\phi_3 + d_1\phi_4 + e_1\phi_5 + f_1\phi_6 + g_1\phi_7 \tag{2.22}$$

Similar to the interior points, a set of equations is obtained by inserting a Taylor series expansion about point 1 and matching coefficients. Resulting coefficients from solving this system of equations are listed in Table 2.2. Similar to Table 2.1, E stands for explicit and C stands for compact. Note that the scheme C2 is identical to that developed in Ref. 52.

Table 2.2: Coefficients for the first boundary point

Scheme	α_1	a_1	b_1	c_1	d_1	e_1	f_1	g_1	Stencil Size	$O(h^*)$
E1	0	-1	1	0	0	0	0	0	2	1
E2	0	$\frac{-3}{2}$	2	$\frac{-1}{2}$	0	0	0	0	3	2
E3	0	$\frac{-11}{6}$	3	$\frac{-3}{2}$	$\frac{1}{3}$	0	0	0	4	3
E4	0	$\frac{-25}{12}$	4	-3	$\frac{4}{3}$	$\frac{-1}{4}$	0	0	5	4
E5	0	$\frac{-137}{60}$	5	-5	$\frac{-10}{3}$	$\frac{-5}{4}$	$\frac{1}{5}$	0	6	5
E6	0	$\frac{-49}{20}$	6	$\frac{-15}{2}$	$\frac{20}{3}$	$\frac{-15}{4}$	$\frac{6}{5}$	$\frac{-1}{6}$	7	6
C2	1	-2	-2	0	0	0	0	0	2	2
C3	2	$\frac{-5}{2}$	2	$\frac{1}{2}$	0	0	0	0	3	3
C4	3	$\frac{-17}{6}$	$\frac{3}{2}$	$\frac{3}{2}$	$\frac{-1}{6}$	0	0	0	4	4
C5	4	$\frac{-37}{12}$	$\frac{2}{3}$	3	$\frac{-2}{3}$	$\frac{1}{12}$	0	0	5	5
C6	5	$\frac{-197}{60}$	$\frac{-5}{12}$	5	$\frac{-5}{3}$	$\frac{5}{12}$	$\frac{-1}{20}$	0	6	6

For the second boundary point, the general formula is given by

$$\alpha_{21}\phi_1' + \phi_2' + \alpha_{22}\phi_3' = a_2\phi_1 + b_2\phi_2 + c_2\phi_3 + d_2\phi_4 + e_2\phi_5 + f_2\phi_6 + g_2\phi_7 \tag{2.23}$$

In general both sides of Eq. 2.23 are asymmetric about point 2. Several possible solutions exist for solving the system of equations formed from the Taylor series expansion about point 2 depending on the choice of the relationship between α_{21} and α_{22}. Four options for these relationships are given in Table 2.3.

Table 2.3: Possible relationships between α_{21} and α_{22}

Option	Relationship	Remarks
A	$\alpha_{21} = \alpha_{22} \neq 0$	This will set the left hand side of Eq. 2.23 to be symmetric about point 2.
B	$\alpha_{21} \neq \alpha_{22} \neq 0$	Due to the extra degree of freedom, a higher order of accuracy is obtained than in option A for the same stencil size.
C	$\alpha_{21} = 0, \alpha_{22} \neq 0$	This compact formulation does not give the derivative on the boundary.
D	$\alpha_{21} = \alpha_{22} = 0$	This produces an explicit scheme that also does not give the derivative at the boundary.

Option A has been used traditionally in most applications of FDL3DI and has become the standard even though a methodical comparison of the different options has not been conducted. The coefficients for Option A are given in Table 2.4.

Table 2.4: Coefficients for second boundary point with $\alpha_{21} = \alpha_{22}$

Scheme	α_{21}	α_{22}	a_2	b_2	c_2	d_2	e_2	f_2	g_2	Stencil Size	$O(h^*)$
AC4	$\frac{1}{4}$	$\frac{1}{4}$	$\frac{-3}{4}$	0	$\frac{3}{4}$	0	0	0	0	3	4
AC5	$\frac{3}{14}$	$\frac{3}{14}$	$\frac{-19}{28}$	$\frac{-5}{42}$	$\frac{6}{7}$	$\frac{-1}{14}$	$\frac{1}{84}$	0	0	5	5
AC6	$\frac{2}{11}$	$\frac{2}{11}$	$\frac{-20}{33}$	$\frac{-35}{132}$	$\frac{34}{33}$	$\frac{-7}{33}$	$\frac{2}{33}$	$\frac{-1}{132}$	0	6	6

For the second to last boundary point, the general equation is similar to that for the second boundary point

$$\alpha_{M1}\phi'_N + \phi'_{N-1} + \alpha_{M2}\phi'_{N-2} = a_M\phi_N + b_M\phi_{N-1} + c_M\phi_{N-2} + d_M\phi_{N-3} + e_M\phi_{N-4} + f_M\phi_{N-5} + g_M\phi_{N-6} \tag{2.24}$$

In fact, the same coefficients given in Table 2.4 are used with the following corrections

i. $\alpha_{M1} = \alpha_{22}$

ii. $\alpha_{M2} = \alpha_{21}$

iii. Signs of coefficients *a* through *g* are reversed, i.e. $a_M = -a_2$, $b_M = -b_2$, …

The general equation for the last boundary point is also similar to the equation for the first boundary point

$$\phi'_N + \alpha_N\phi'_{N-1} = a_N\phi_N + b_N\phi_{N-1} + c_N\phi_{N-2} + d_N\phi_{N-3} + e_1\phi_{N-4} + f_1\phi_{N-5} + g_1\phi_{N-6} \tag{2.25}$$

Again, due to the similarities to the equation for the first boundary point, coefficients from Table 2.2 are used with the following corrections

i. $\alpha_N = \alpha_1$

ii. Signs of coefficients *a* through *g* are reversed, i.e. $a_N = -a_1$, $b_N = -b_1$, …

2.3.3 Low Pass Spatial Filtering

While the higher order compact scheme addresses the issue of accuracy, an equally important property of a numerical scheme is stability. Like other centered schemes, in practice, high order collocated compact schemes are nondissipative and susceptible to numerical instabilities due to the growth of unstable high frequency modes. Theoretical stability analysis of higher order compact schemes is not straightforward. Analysis is only readily available on the

simplest cases of linear equations on infinite domains with an even mesh and explicit time integration.[53] In practice, problems typically involve non-linear equations, bounded domains, body fitted curvilinear meshes, and implicit time integration.

Furthermore, stability analysis seldom accounts for physical approximations such as the zero normal pressure gradient at a solid wall $(\partial p/\partial n = 0)$. This is derived from boundary layer theory but can potentially incur significant errors near separation and reattachment locations. Implementation of such a boundary condition is often approximated with $\partial p/\partial n \cong \partial p/\partial \eta = 0$ where η is the curvilinear coordinate emanating from the wall and may not coincide with the wall normal. In fact, boundary conditions derived on an evenly spaced mesh may not be stable on a general curvilinear mesh.[54]

To stabilize the overall higher order scheme, after each sub-iteration, the conservative variables are passed through a high order non-dispersive low-pass spatial filter developed by Gaitonde et al.[55]. Only the poorly resolved high-frequency content of the solution is damped by this highly-discriminating filter. This method of filtering the conservative variables, known as Implicit LES, has shown to be more effective at maintaining both stability and accuracy on stretched curvilinear meshes than traditional explicitly added artificial dissipation.[49] A summary of the filtering approach is described for interior and boundary points in the following two sections. Further details can be found in Ref. 51.

2.3.3.1 Interior Points

A $2N$-order filter derived by Gaitonde et al. for interior points requires a stencil size of $2N+1$ and has the general formula

$$\alpha_f \bar{\phi}_{j-1} + \bar{\phi}_j + \alpha_f \bar{\phi}_{j+1} = \sum_{n=0}^{N} \frac{a_n}{2} \left(\phi_{j+n} + \phi_{j-n} \right) \tag{2.26}$$

Here, $\bar{\phi}$ represents filtered values of the scalar quantity ϕ. Similar to the compact finite difference scheme, the filtering is implicit and requires the solution of a tridiagonal system. To derive the characteristic spectral function of the filter, which is used to determine the coefficients in Eq. 2.26, the same periodic Fourier expansion (Eq. 2.17) used in the wave number analysis of the compact scheme is substituted into Eq. 2.26, yielding

$$\alpha_f \bar{\tilde{\phi}}(-1) + \bar{\tilde{\phi}}(0) + \alpha_f \bar{\tilde{\phi}}(1) = \sum_{n=0}^{N} \frac{a_n}{2} \left(\tilde{\phi}(n) + \tilde{\phi}(-n) \right) \tag{2.27}$$

Through algebraic manipulation, this further reduces to

$$\bar{b}_k = SF(\omega) b_k \tag{2.28}$$

where the spectral function $SF(\omega)$ of the filter is

$$SF(\omega) = \frac{\sum_{n=0}^{N} a_n \cos(n\omega)}{1 + 2\alpha_f \cos(\omega)} \tag{2.29}$$

This equation is representative of the attenuation the filter will apply to a given wave number. Coefficients in Eq. 2.29 must now be determined such that low frequencies are allowed to pass through with little attenuation while higher under-resolved frequencies are eradicated. Equation 2.29 has $N+2$ unknowns, namely α_f, a_0, a_1, …, a_N. To obtain the coefficients, the

highest frequency and odd-even modes are eliminated by enforcing the condition $SF(\pi)=0$ [50, 56]. In turn, this allows for the coefficients to be determined from a Taylor series expansion of ϕ about the point j. Even though the Taylor series expansion leads a complete system of equations, the parameter α_f is retained as a free parameter. This allows for an explicit formulation of the filter where the left hand side of Eq. 2.26 is decoupled by choosing $\alpha_f = 0$. Due to the form of the denominator in Eq. 2.29, an upper bound of $|\alpha_f| < 0.5$ is required to avoid division with zero. However, increasing the value of α_f reduces the attenuation of lower wave numbers. Coefficients for filters of up to 10th-order are given in Table 2.5. The formal order of accuracy of the filter is representative of the severity at which the filter damps low frequencies. Lower order filters will have a higher attenuation of low frequencies than higher order filters. This illustrated with the spectral functions for the different filtering orders of accuracy shown in Figure 2.4. The deviation from unity of the spectral function is representative of the attenuation applied to the corresponding wave number.

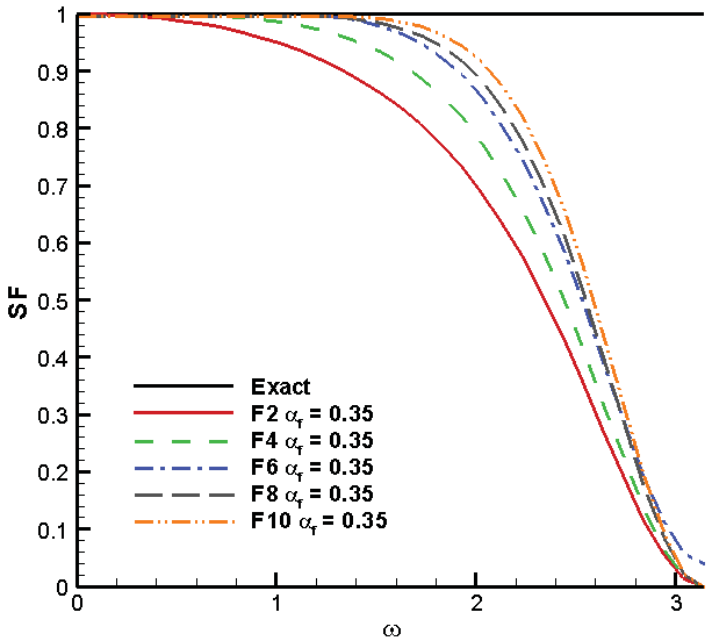

Figure 2.4: Frequency response characterisitics of implicit central filters with $\alpha_f = 0.35$

Table 2.5: Implicit Central Filter Coefficients $\left(\left|\alpha_f\right| < 0.5\right)$

Scheme	a_0	a_1	a_2	a_3	a_4	a_5	Stencil Size	$O(h^*)$
F2	$\frac{1}{2}+\alpha_f$	$\frac{1}{2}+\alpha_f$	0	0	0	0	3	2
F4	$\frac{5}{8}+\alpha_f\frac{3}{4}$	$\frac{1}{2}+\alpha_f$	$\frac{-1}{8}+\frac{\alpha_f}{4}$	0	0	0	5	4
F6	$\frac{11}{16}+\alpha_f\frac{5}{8}$	$\frac{15}{32}+\alpha_f\frac{17}{16}$	$\frac{-3}{16}+\alpha_f\frac{3}{8}$	$\frac{1}{32}-\frac{\alpha_f}{16}$	0	0	7	6
F8	$\frac{93+70\alpha_f}{128}$	$\frac{7+18\alpha_f}{16}$	$\frac{-7+14\alpha_f}{32}$	$\frac{1}{16}-\frac{\alpha_f}{8}$	$\frac{-1}{128}+\frac{\alpha_f}{64}$	0	9	8
F10	$\frac{193+126\alpha_f}{256}$	$\frac{105+302\alpha_f}{256}$	$\frac{-15+30\alpha_f}{64}$	$\frac{45-90\alpha_f}{512}$	$\frac{-5+10\alpha_f}{256}$	$\frac{1-2\alpha_f}{512}$	11	10

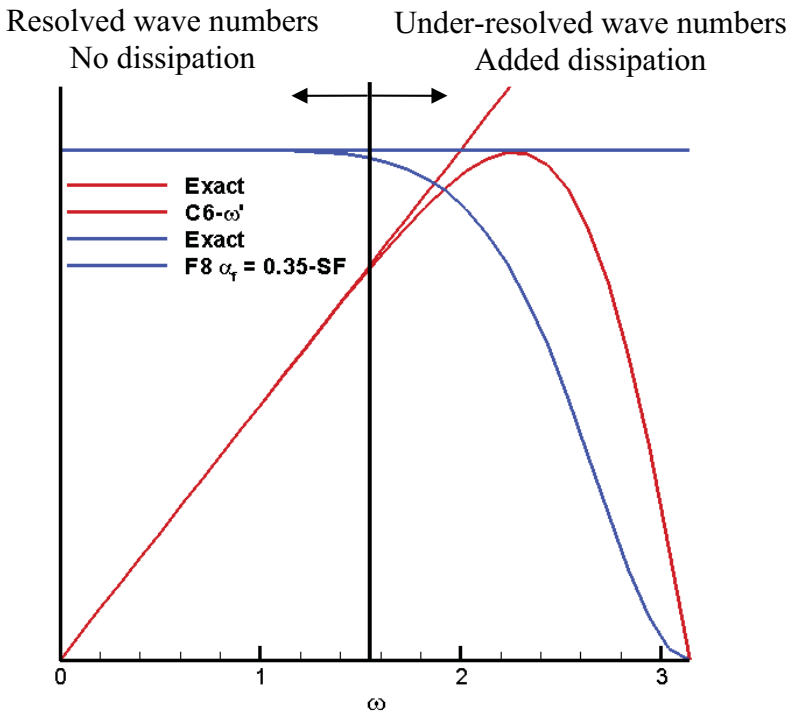

Figure 2.5: Combined differencing and filtering scheme

The combination of a 6th-order compact differencing and an 8th-order low pass filter is summarized in Figure 2.5. The filter has the desired effect of dissipating the under-resolved

higher wave numbers with no attenuation applied to the lower wave numbers resolved by the compact differencing scheme.

2.3.3.2 Boundary Points

Due to the large stencil requirement of the interior filtering scheme, in particular the 10^{th}-order filter with a stencil of 11 points, special treatment is required near boundaries. For the 10^{th}-order filter, points 1 through 5 and $N-4$ through N will have a stencil that extends beyond the boundary of the domain. Two approaches that address this issue have been developed.

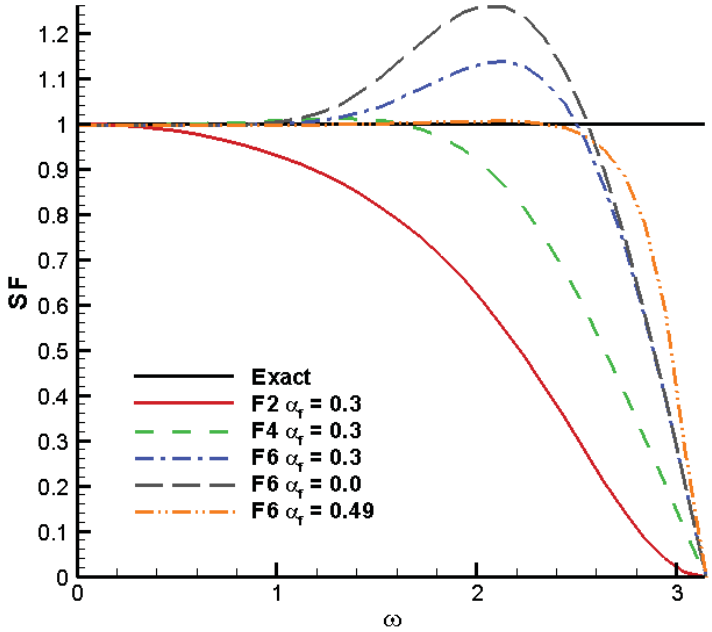

Figure 2.6: Frequency response characterisitics of one sided filters with different α_f

The first method uses one sided filters of similar order of the interior scheme to preserve the tridiagonal nature of the scheme. However, in this case for $0 < \alpha_f < 0.5$ the spectral function will be complex, which is an indication that the filter may introduce artificial dispersion. In addition, as demonstrated in Figure 2.6, the magnitude of the spectral function can exceed unity for a selection of wave numbers which will therefore be amplified. However, also as shown in Figure 2.6, the degree to which the magnitude of the spectral function extends beyond unity

diminishes as α_f approaches 0.5. Thus a value of α_f near 0.5 is recommended for the one sided filters. A complete listing of the coefficients for these filters is given in Ref. 51.

The second method reduces the order of the filter (and hence the stencil) at the j^{th} point from the boundary to the order $2j-2$. By reducing the order of the filter near the boundaries, a central filter can be maintained up to the boundary. It has been shown that as α_f approaches 0.5 for a lower order filter, the lower order filter will behave similar to that of a higher order filter. For example, as α_f approaches 0.5 for a 2^{nd}-order filter, it behaves similar to an 8^{th}-order filter as illustrated in Figure 2.7.[57] Thus, a low dissipative filter can be maintained near boundaries by reducing the order of the filter while ramping up α_f closer to a value of 0.5.

In both situations, no filtering is applied to the first boundary point as this information is determined by the boundary condition.

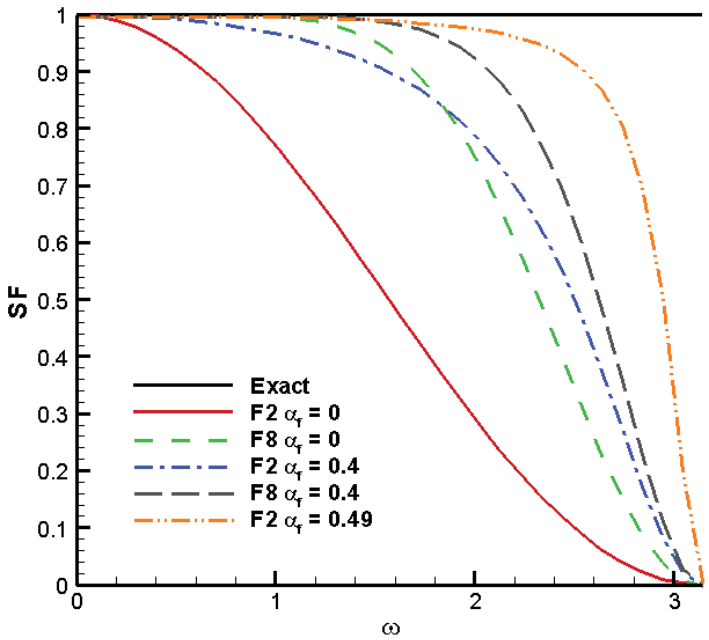

Figure 2.7: Frequency response characterisitics of central filters F2 and F8 with different α_f

2.4 Metric Calculations

Issues of freestream preservation and metric cancellation must be addressed when applying the higher order compact scheme to nontrivial three-dimensional geometries. If these issues are not properly handled, the resulting errors will have devastating effects on both 2nd and higher-order schemes. In two-dimensions, it has been found that metrics evaluated with the same higher-order compact finite difference formulations as the fluxes produce freestream preservation and metric cancellation errors similar to that of a standard second-order central difference method.[49, 58] As a side note, the application of *analytical* metrics can lead to unacceptable errors and should in general be avoided.[49]

It has been assessed in the literature that although this simple straight-forward approach is effective in two-dimensions, it fails to satisfy metric cancellation in three-dimensions.[59, 60, 61] Analytically, the metric relationships are

$$\begin{aligned} \frac{\xi_x}{J} &= y_\eta z_\zeta - y_\zeta z_\eta \\ \frac{\eta_x}{J} &= y_\zeta z_\xi - y_\xi z_\zeta \\ \frac{\zeta_x}{J} &= y_\xi z_\eta - y_\eta z_\xi \end{aligned} \tag{2.30}$$

$$\begin{aligned} \frac{\xi_y}{J} &= z_\eta x_\zeta - z_\zeta x_\eta \\ \frac{\eta_y}{J} &= z_\zeta x_\xi - z_\xi x_\zeta \\ \frac{\zeta_y}{J} &= z_\xi x_\eta - z_\eta x_\xi \end{aligned} \tag{2.31}$$

$$\frac{\xi_z}{J} = x_\eta y_\zeta - x_\zeta y_\eta$$
$$\frac{\eta_z}{J} = x_\zeta y_\xi - x_\xi y_\zeta \tag{2.32}$$
$$\frac{\zeta_z}{J} = x_\xi y_\eta - x_\eta y_\xi$$

The relationships of Eqs. 2.30, 2.31, and 2.32 may be associated with the x, y, and z components of the surface area vectors respectively. Corresponding to these metric equations are metric identities which were implicitly invoked while deriving the strong-conservation form of the curvilinear Navier Stokes equations

$$\left(\frac{\xi_x}{J}\right)_\xi + \left(\frac{\eta_x}{J}\right)_\eta + \left(\frac{\zeta_x}{J}\right)_\zeta = 0$$
$$\left(\frac{\xi_y}{J}\right)_\xi + \left(\frac{\eta_y}{J}\right)_\eta + \left(\frac{\zeta_y}{J}\right)_\zeta = 0 \tag{2.33}$$
$$\left(\frac{\xi_z}{J}\right)_\xi + \left(\frac{\eta_z}{J}\right)_\eta + \left(\frac{\zeta_z}{J}\right)_\zeta = 0$$

These metric identities represent the surface conservation of a closed cell. A fourth metric identity representing volume conservation, referred to as the geometric conservation law (GCL) in the literature, is

$$\left(\frac{1}{J}\right)_t + \left(\frac{\xi_t}{J}\right)_\xi + \left(\frac{\eta_t}{J}\right)_\eta + \left(\frac{\zeta_t}{J}\right)_\zeta = 0 \tag{2.34}$$

All of these identities must be satisfied numerically in order to guarantee freestream preservation. For static time independent meshes – only the identities of Eq. 2.33 are applicable.

Unfortunately, evaluating the derivatives in Eqs. 2.30, 2.31, and 2.32 with either explicit or compact finite differences will not satisfy the identities in Eq. 2.33; thus inducing mesh related errors in regions of significant mesh variations and singularities. These issues have been

resolved for traditional 2nd-order schemes with either a simple averaging technique by Pulliam and Steger[60] or with finite volume concepts as suggested by Vinokur[59]. While these techniques work very well on 2nd-order schemes, they are not easily extended to the higher-order compact schemes.

A less well known method for achieving metric cancellation was presented by Thomas and Lombard.[61] Rather than using averaging techniques or introducing any geometrical concepts, the metric equations are rewritten before discretization in a "conservative" form

$$\begin{aligned}
\frac{\xi_x}{J} &= \left(y_\eta z\right)_\zeta - \left(y_\zeta z\right)_\eta \\
\frac{\eta_x}{J} &= \left(y_\zeta z\right)_\xi - \left(y_\xi z\right)_\zeta \\
\frac{\zeta_x}{J} &= \left(y_\xi z\right)_\eta - \left(y_\eta z\right)_\xi
\end{aligned} \tag{2.35}$$

$$\begin{aligned}
\frac{\xi_y}{J} &= \left(z_\eta x\right)_\zeta - \left(z_\zeta x\right)_\eta \\
\frac{\eta_y}{J} &= \left(z_\zeta x\right)_\xi - \left(z_\xi x\right)_\zeta \\
\frac{\zeta_y}{J} &= \left(z_\xi x\right)_\eta - \left(z_\eta x\right)_\xi
\end{aligned} \tag{2.36}$$

$$\begin{aligned}
\frac{\xi_z}{J} &= \left(x_\eta y\right)_\zeta - \left(x_\zeta y\right)_\eta \\
\frac{\eta_z}{J} &= \left(x_\zeta y\right)_\xi - \left(x_\xi y\right)_\zeta \\
\frac{\zeta_z}{J} &= \left(x_\xi y\right)_\eta - \left(x_\eta y\right)_\xi
\end{aligned} \tag{2.37}$$

While this method was presented in the context of a 2nd-order scheme, the simpler averaging method has been favored in the literature. Even though this "conservative" method was not envisioned for higher-order compact schemes, it has been shown by Visbal and Gaitonde[62] to

satisfy both freestream preservation and metric cancellation on general three-dimensional curvilinear meshes.

2.5 Parallel Computation

Despite continuous advancement of computing technology, calculations on meshes consisting of millions of grid points over tens of thousands of iterations cannot be completed in an adequate time frame. To reduce the computational time, a parallel paradigm is introduced where solutions are obtained through simultaneous computations on multiple independent processors. This involves decomposing the computational domain into smaller blocks which are then distributed across multiple processors. In addition, a synchronization process is required to update block boundaries that were previously interior points. A schematic of this process for a one dimensional mesh is given in Figure 2.8. Here, the original mesh is decomposed into two blocks at point *j*. However, due to the five-point stencil required by the compact differencing scheme, a five point overlap with two fringe points is required. While this overlap incurs an additional overhead to the computation by increasing the total number of points; it is necessary in order to properly carry the solution across block boundaries.

The synchronization process has been implemented using a Message Passage Interface (MPI) library.[63] In the present schematic, this process is responsible for transferring the solution from points $N-4$ and $N-3$ on block 1 to points 1 and 2 respectively on block 2. The solution from points 4 and 5 on block 2 are then transferred to points $N-1$ and N on block 1. Hence, the values transferred from block 1 act as boundary conditions on block 2 and vice versa allowing for the solution to seamlessly continue across the interface and maintain the formal accuracy of the numerical scheme. For consistency, boundaries that rely on physical boundary conditions are also updated immediately after MPI synchronization. Two MPI and physical boundary condition

updates are performed for each Newton sub-iteration: once after the solution is updated from the time integration and once again after the solution is filtered.

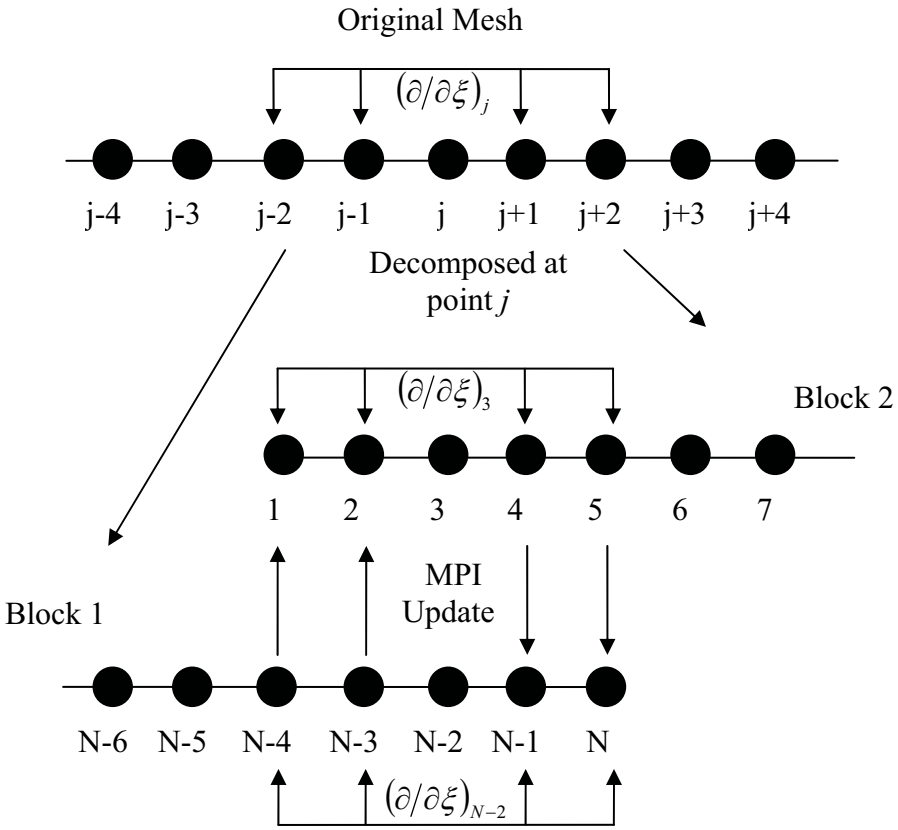

Figure 2.8: Schematic of domain decomposition with five point overlap

While a one-dimensional description is given here for the domain decomposition and MPI synchronization; the extension to higher dimensions is straight forward due to the use of structured meshes.

To achieve a high parallel efficiency, it is important to partition the mesh as evenly as possible across the processors. A well balanced partitioning was achieved with automated tools developed for FDL3DI.[64] These tools also guarantee that the minimum stencil requirement is satisfied on the partitions as discussed in the following section.

2.6 Chimera Overset Meshes and Hole Cutting

Structured meshes are suitable for a practical implementation of the compact differencing and filtering schemes due to the larger stencils and tridiagonal nature of the schemes. However, applying a single structured mesh for analysis of a complicated geometry can be prohibitive. In addition, structured meshes often inadvertently cluster grid points in regions of less interest resulting in an undesirable computational overhead.

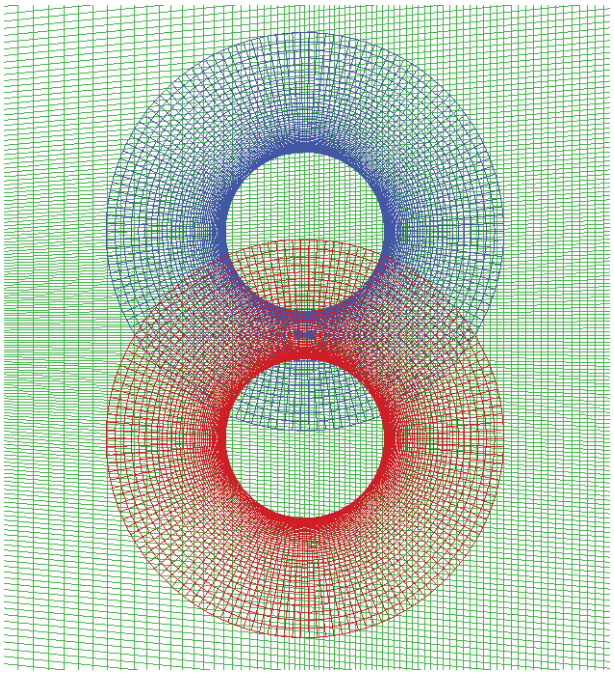

Figure 2.9: A Chimera overset mesh

To expand the usefulness and flexibility of structured meshes, Benek et al.[65] introduced the concept of Chimera overset meshes while solving the Euler equations. The fundamental concept of the Chimera overset technique is to use a collection of meshes with arbitrary overlapping regions, in place of a single mesh, to represent the geometry and computational domain. Thus, a complex geometry can be broken down into smaller and more manageable pieces. Often multiple body fitted meshes are used with a larger background mesh to tie together all the individual meshes. An example of a Chimera mesh for two cylinders is presented in Figure 2.9.

Here, two body-fitted meshes represent the cylinders with a background mesh coupling the system together.

Two significant problems exist with this system as it stands. First, a significant number of points from the background mesh lie within the solid walls of the cylinders where a solution is not desired. Secondly, two overlying solutions will exist in regions where the body fitted meshes overlap the background mesh.

To resolve these issues, Benek et al. suggested a hole cutting technique. Here, all points are flagged to either be valid points for calculations or hole points where the solution is invalid. A simple modification to an implicit scheme is required to account for holes in the mesh. Consider the exemplary algebraic system of equations typical of the compact finite difference scheme,

$$A\phi = F \tag{2.38}$$

where A is the tridiagonal matrix, ϕ is an unknown vector of derivatives, and F is the known right-hand side vector. A general representation of the system is given in Figure 2.10. Suppose that points $j-1$, j, and $j+1$ are flagged as hole points. A simple modification to the implicit matrix A is now required to decouple the hole points from the system of equations. This is done by removing the off diagonal coefficients from the matrix at the hole points and treating points $j-3$, $j-2$, $j+2$, and $j+3$ as boundary points by modifying their off diagonal coefficients (see Figure 2.11). Also, f_{j-3}, f_{j-2}, f_{j+2}, and f_{j+3} must be recomputed with an appropriate boundary stencil so that the invalid solution of the hole points is not used to form the right-hand side. Finally, f_{j-1}, f_j, and f_{j+1} are set to zero so that the derivatives in the holes are set to zero. Similar modifications are required for the implicit matrix of the filtering scheme and implicit time integration matrix of Eq. 2.9. Note that because the hole points are not actually removed

(just decoupled from the system of equations), they become a computational overhead. Thus, while hole cutting is powerful, it should be used with caution and the number of hole points should be kept at a minimum when possible.

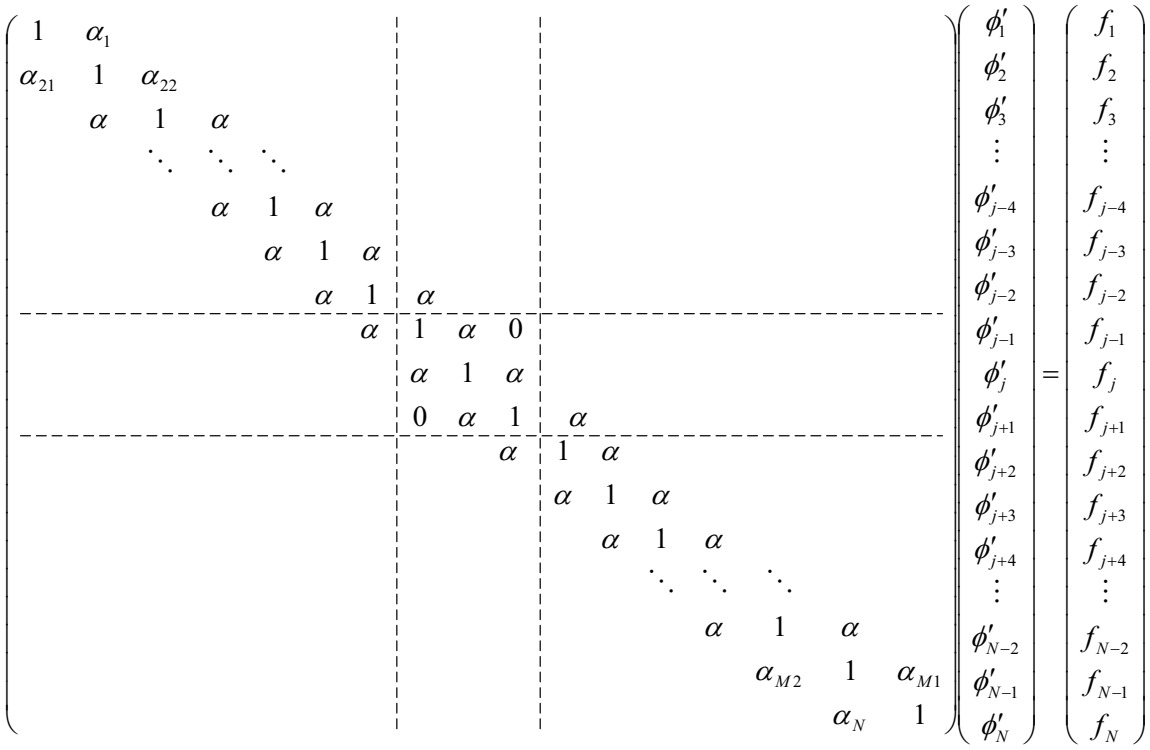

Figure 2.10: Representatative tridiagonal system of equations

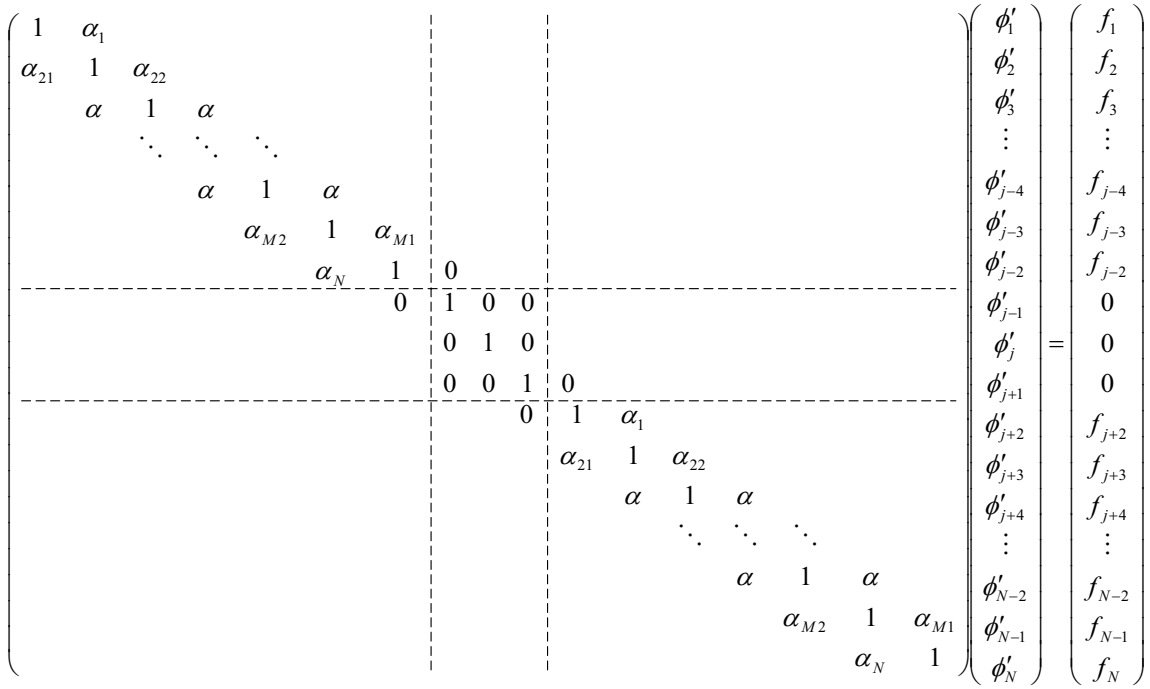

Figure 2.11: Modified tridiagonal system of equations to account for a hole at *j*-1, *j*, and *j*+1

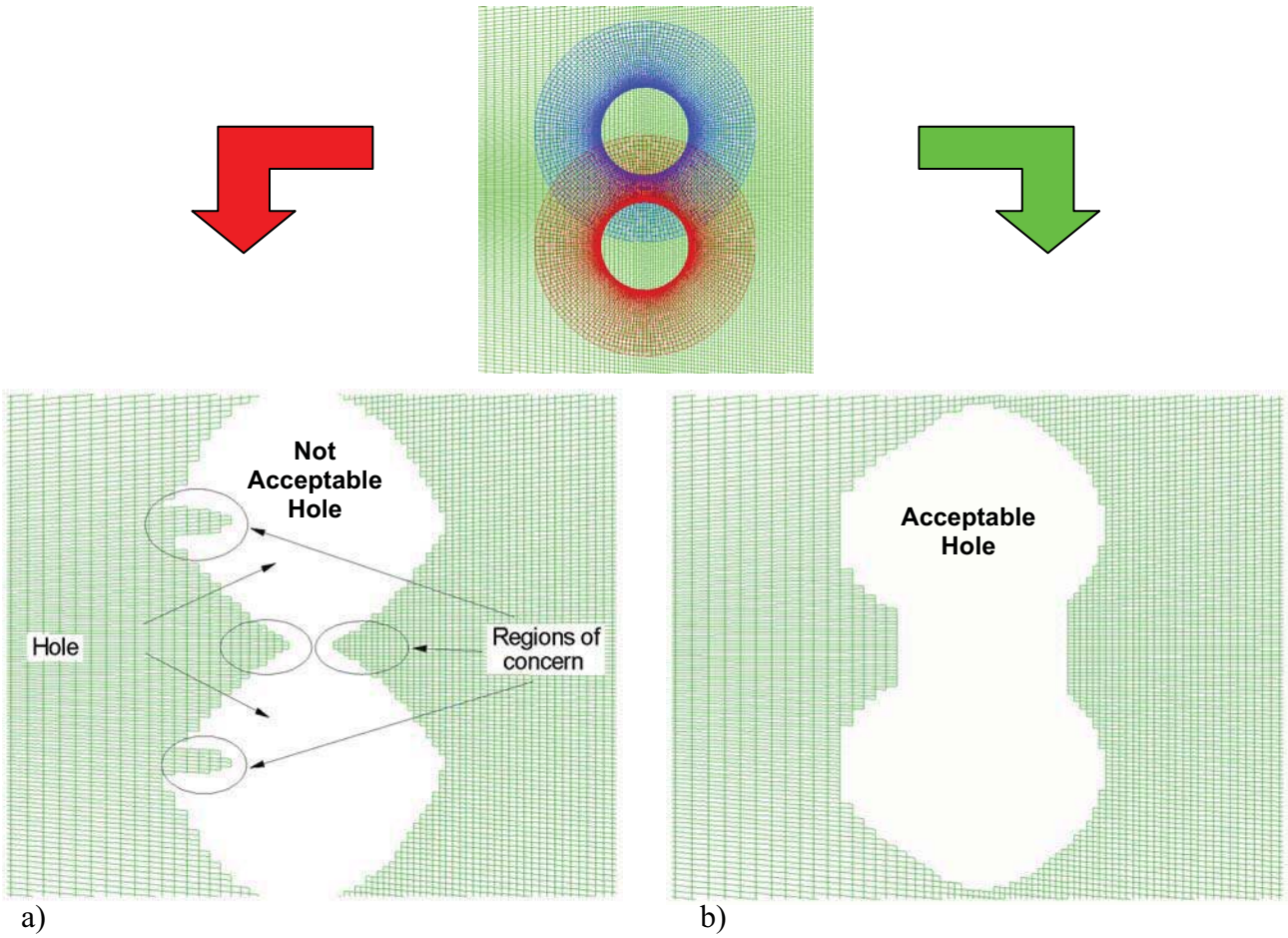

Figure 2.12: A Chimera mesh with hole cutting
a) Unsupported minimum stencil b) Minimum stencil supported

Extra care must be taken when generating holes for FDL3DI due to the larger stencil of the filter and compact differencing scheme. If a 10^{th}-order filter is used, holes must be cut so that all regions of non-hole points consist of at least 11 continuous points for all three computational coordinates. Otherwise, the filter will use the invalid solution in holes to generate the right hand side of the tridiagonal system of equations. Consider Figure 2.12 where two holes have been generated in the background mesh for the two cylinder overset system. Figure 2.12a exemplifies a hole with regions where the 11 point minimum stencil requirement is not satisfied. The hole generated in Figure 2.12b on the other hand does support the minimum stencil.

Appropriate conditions must be supplied at all mesh boundaries, including boundaries generated from hole cutting. Because mesh boundaries overlap into interior regions on other meshes where valid solutions exist, it is natural to use the interior solution to construct boundary conditions for an overlapping mesh. As boundary points do not coincide with the interior point on the neighboring mesh, interpolation is the simplest method of transferring the interior solution to the boundaries. The interpolation is achieved in FDL3DI through a 6^{th} order accurate interpolation scheme in order to maintain the overall higher order spatial accuracy of the methodology.[66] Furthermore, following the discussion of the parallel implementation, two fringe points must be updated on all overlapping boundaries.

2.7 Present Numerical Scheme

For the present computations, the 6^{th}-order compact differencing scheme was implemented on the interior points in all spatial directions. For stability reasons, the scheme is reduced to the one sided 5^{th}-order scheme at the second boundary point and a 4^{th}-order one sided scheme at the first boundary point. This is also summarized in Table 2.6.

Table 2.6: Compact differncing scheme used for present computations

	Point				
Coordinate	1	2	Interior	*N*-1	*N*
ξ	C4	AC5	C6	AC5	C4
η	C4	AC5	C6	AC5	C4
ζ	C4	AC5	C6	AC5	C4

The solution was filtered with an 8^{th}-order filter in the streamwise and surface normal directions and a 10^{th}-order filter in the spanwise direction. The 10^{th}-order filter was used in the spanwise direction since the mesh has uniform spacing in that direction. Boundary points were

treated with the second method described in section 2.3.3.2 where the order of the filter is reduced in order to maintain a central scheme at each grid point. A summary of the filtering scheme is given in Table 2.7.

Table 2.7: Filtering scheme used for present computations

Coordinate		Point					
		1, *N*	2, *N*-1	*3*, *N*-2	4, *N*-3	*5*, *N*-4	Interior
ξ	Filter	0	F2	F4	F6	F8	F8
	α_f	0.0	0.49	0.35	0.35	0.35	0.35
η	Filter	0	F2	F4	F6	F8	F8
	α_f	0.0	0.49	0.35	0.35	0.35	0.35
ζ	Filter	0	F2	F4	F6	F8	F10
	α_f	0.0	0.49	0.35	0.35	0.35	0.35

After each Newton sub-iteration, the one-dimensional filter is successively applied to the conservative variables along each of the three computational coordinates. Before filtering in a subsequent computational coordinate, the solution is updated with filtered quantities. To avoid any bias by constantly applying the filter in the same sequence, a permutation is introduced to cycle through all six possible filtering sequences. The filtering sequence is cycled once per time step; thus the same sequence is applied after each sub-iteration of a particular time step.

2.8 Computing Time-mean Quantities

All time-mean quantities were evaluated by first computing spanwise spatial mean quantities which were subsequently averaged over approximately eight characteristic times. Specifically, the instantaneous spanwise mean quantities were averaged over 54,000 time steps with a non-dimensional time step of $\Delta t = 0.00015$. To eliminate the effect of initial transients, the time accurate solution was allowed to develop over five characteristic times before the time averaging

process was initiated. Eradication of initial transients resulting from a freestream initial solution was further accelerated by initializing three-dimensional computations with a developed two-dimensional solution. Two-dimensional solutions were computed with 3 points in the spanwise extent and were transferred to the three-dimensional mesh through simple extrusion.

3 Computational Mesh and Boundary Conditions

All computational meshes were generated using the software package GridGen[67]. Initially, a single baseline O-grid was generated about the SD7003 airfoil with a rounded trailing edge as depicted in Figure 3.1. The rounded edge had a radius of curvature of 0.0004 relative to the chord. Grid coordinates are oriented such that ξ traverses clockwise around the airfoil, η is normal to the surface, and ζ follows the spanwise direction. The baseline mesh consisted of 315x151x101 points in the ξ, η, ζ directions, respectively, which is approximately 4.8 million grid points. The mesh is evenly spaced in the spanwise direction with a width of Z/C = 0.2. A spanwise periodic boundary condition was imposed on all meshes. Furthermore, a five point overlap is required to impose the O-grid periodic boundary condition.

The farfield boundary was positioned 30 chords away from the airfoil in order to reduce its influence on the solution near the airfoil. In addition, the mesh is stretched to prevent pressure waves from reflecting back into the computational domain.[68] The rapid stretching of the mesh promotes transfer of energy to reflected odd-even modes which in turn are eliminated by the low-pass filter. This technique has been empirically shown to be effective in non-linear and multi-dimensional situations where more advanced non-reflecting techniques[69] derived through asymptotic or linear-analysis may be ineffective.

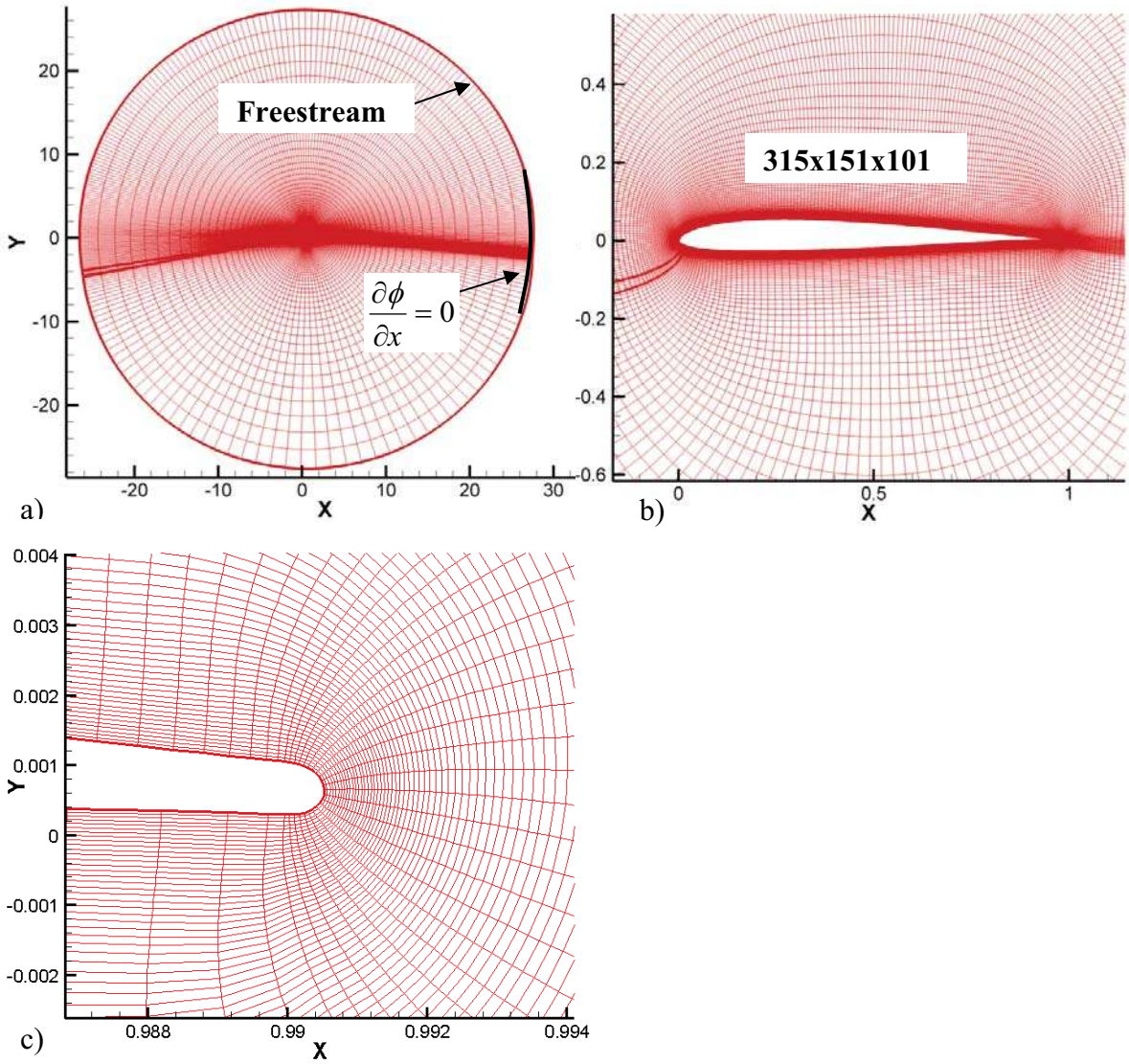

Figure 3.1: Baseline Computational mesh. Grid dimensions of 315x151x101: a) Full O-grid b) Mesh near near the body c) Rounded trailing edeg

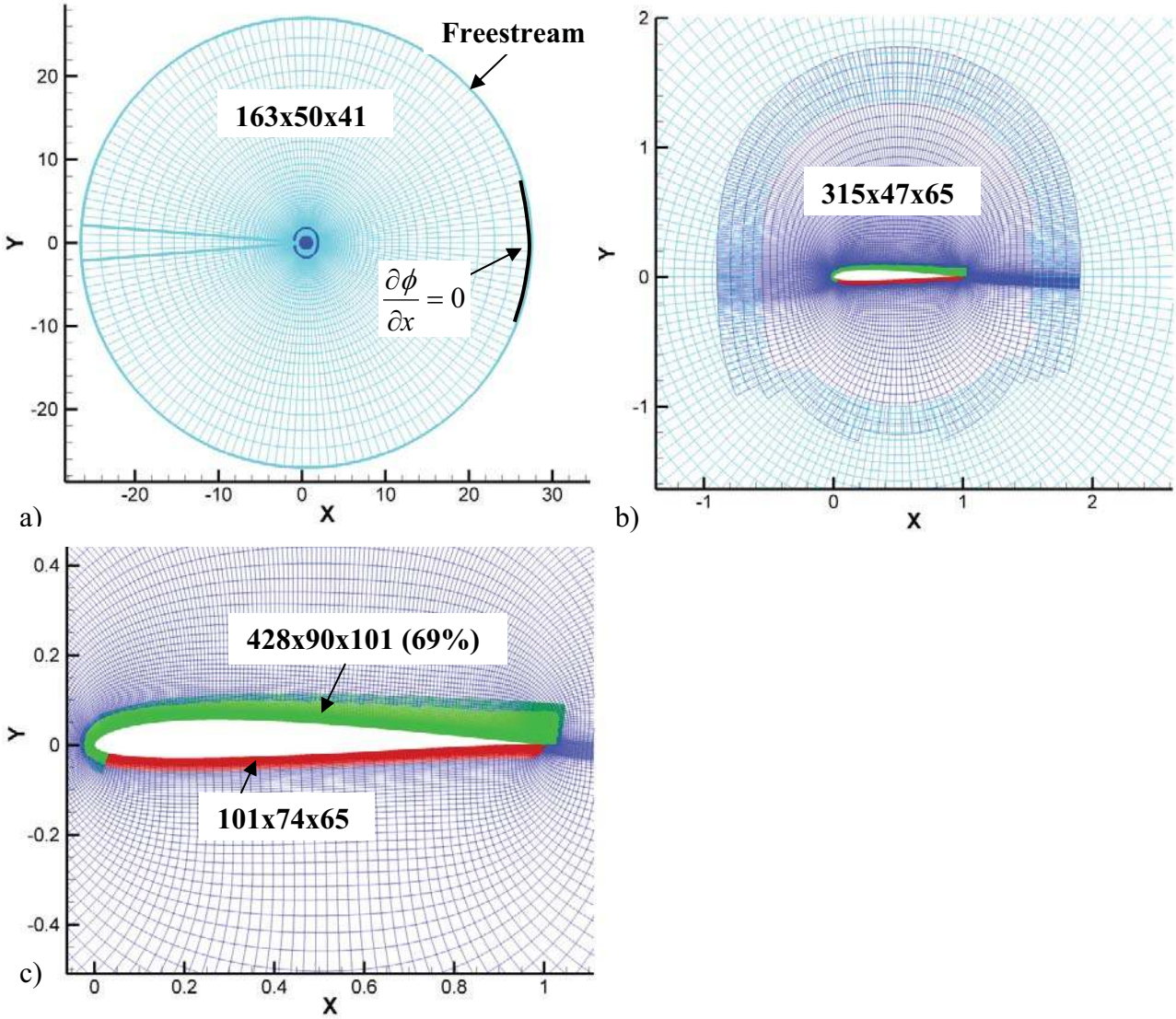

Figure 3.2: Overset computational mesh. Grid dimensions (ξ, η, ζ) are depicted for each grid: a) Background O-grid b) Near O-grid c) Body fitted grids

A second mesh (Figure 3.2) with greater refinement on the upper surface of the airfoil was constructed that exploited the Chimera overset capabilities of the FDL3DI solver. The baseline mesh was used as the basis for the overset mesh and a portion of it was retained as the near O-grid shown in Figure 3.2b. A circular O-grid (Figure 3.2a) was generated away from the airfoil to again move the farfield boundary conditions 30 chords away from the airfoil. By using two meshes, fewer grid points were required to move the farfield boundary away from the airfoil. As

this mesh is away from the separated flow of interest, its spanwise resolution was reduced to 41 points. Similarly, the near O-grid and pressure-side grid were reduced to 65 spanwise points. The grid on the suction side of the airfoil maintained 101 spanwise points. In addition, this mesh was doubled in both the surface normal and streamwise directions compared to the baseline mesh. This reduced y^+ values to below 0.3 for Reynolds number of $6x10^4$ and angle of attack of 4°. After these modifications, the total number of mesh points in the overset system is approximately 5.7 million grid points, with 69% of the points on the suction side of the airfoil. The overset system was further decomposed into 60 blocks for parallel execution.

Two additional overset meshes were generated to asses that the overset mesh adequately resolved the transition of the free shear layer. A coarse overset and a fine overset mesh were generated by altering the streamwise point count on the suction surface mesh from 428 to 328 and 528 points respectively. The coarse overset mesh consisted of 5.7 million while the fine overset mesh consisted of 6.6 million points.

3.1 Wall Boundary Condition

The airfoil surface was modeled with a no-slip adiabatic wall boundary condition with a zero normal pressure gradient. The no-slip is satisfied by simply setting the velocity vector components to zero. Density on the wall is calculated indirectly through the wall pressure and temperature; both of which were obtained with a zero wall normal gradient equation discretized with a 4^{th}-order accurate explicit differencing scheme. Assuming the η computational coordinate approximates the wall normal, the explicit differencing formula for the scalar ϕ is written to give the quantity at the wall as

$$\phi_{wall} = \frac{48\phi_2 - 36\phi_3 + 16\phi_4 - 3\phi_5}{25} \tag{3.1}$$

Pressure and temperature at the wall are now computed by replacing ϕ with the respective quantity. Once wall pressure and temperature are obtained, the density at the wall was calculated with the aid of the ideal gas law.

$$\rho_{wall} = \gamma M^2 \frac{p_{wall}}{T_{wall}} \tag{3.2}$$

3.2 Farfield Boundary Condition

A freestream condition was prescribed on the majority of the farfield boundary. The freestream conditions are

$$\begin{aligned} u &= \cos(\alpha) \\ v &= \sin(\alpha) \\ w &= 0 \\ p &= \frac{1}{\gamma M^2} \\ \rho &= 1 \end{aligned} \tag{3.3}$$

However, downstream of the airfoil, a zero x-gradient extrapolation is imposed on density and velocity components. The freestream pressure is still prescribed. The extrapolation is expressed for a general scalar ϕ in computational coordinates as

$$\frac{d\phi}{dx} = \frac{d\phi}{d\xi}\xi_x + \frac{d\phi}{d\eta}\eta_x = 0 \tag{3.4}$$

The mesh is intentionally constructed such that $\zeta_x = 0$. The analytical expression is then discretized with a 2nd-order central scheme in the ξ direction and 1st-order scheme in the η direction. After rearranging the discrete equation, a tridiagonal system is solved to obtain the boundary values

$$\frac{\phi_{i+1,j,k} - \phi_{i-1,j,k}}{2} \xi_x^{i,j,k} + \phi_{i,j,k} \eta_x^{i,j,k} = \eta_x^{i,j,k} \phi_{i,j-1,k} \tag{3.5}$$

3.3 Spanwise Periodic Boundary Condition

A spanwise periodic boundary condition was imposed on all meshes to simulate an infinite wing. This boundary condition was imposed using a five point overlap similar to what was described for the domain decomposition in section 2.5. The following assignments were applied to all *i, j* values of the meshes to impose the periodic boundary conditions.

$$\begin{aligned} \phi_{i,j,1} &= \phi_{i,j,k_{\max}-3} \\ \phi_{i,j,2} &= \phi_{i,j,k_{\max}-4} \\ \phi_{i,j,k_{\max}} &= \phi_{i,j,5} \\ \phi_{i,j,k_{\max}-1} &= \phi_{i,j,4} \end{aligned} \tag{3.6}$$

The decomposition process for parallel computation was restricted from creating any cuts in the spanwise direction of the mesh in order to ensure that $k = 1$ and $k = k_{max}$ for all blocks were located on the spanwise boundaries of the computational domain.

4 Numerical Considerations

Several numerical parameters were investigated at 4° angle of attack with a Reynolds number of 6×10^4 to limit numerical errors. This combination of angle of attack and Reynolds number was chosen as it has been investigated extensively experimentally[22, 32] and numerically[23, 24]. Specifically, spatial discretization, grid resolution, spanwise extent, and freestream Mach number were evaluated.

4.1 Effect of Spatial Discretization

Both 2nd- and 6th-order computations were performed on the baseline mesh at 4° angle of attack and Reynolds number 6×10^4. Fourth-order spectral damping terms were used to stabilize

the 2nd-order solution.[47] Mean surface pressure and skin friction coefficients from these calculations are presented in Figure 4.1. Even though the pressure gradient predicted by the 6th-order scheme is slightly sharper in the transition region, the surface pressures agree well between the two calculations. However, a starker difference can be observed in the skin friction downstream of X/C = 0.5. The 6th-order scheme is able to predict a significantly sharper rise in skin friction coefficient using the same mesh. Further differences between the 2nd-order and 6th-order solutions can be observed in contours of Reynolds stress shown in Figure 4.2. The 2nd-order scheme yields a lower absolute magnitude of the Reynolds stress than the 6th-order scheme.

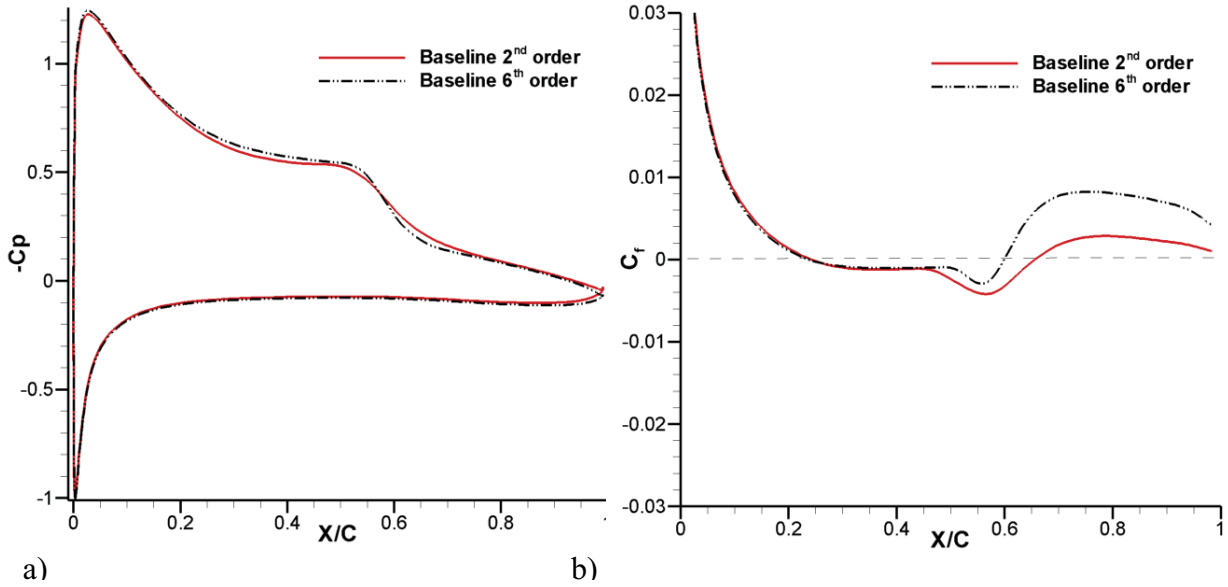

Figure 4.1: Effect of spatial discretization (α = 4°, Re = 6x10^4):
a) Mean surface *Cp* b) Mean surface C_f

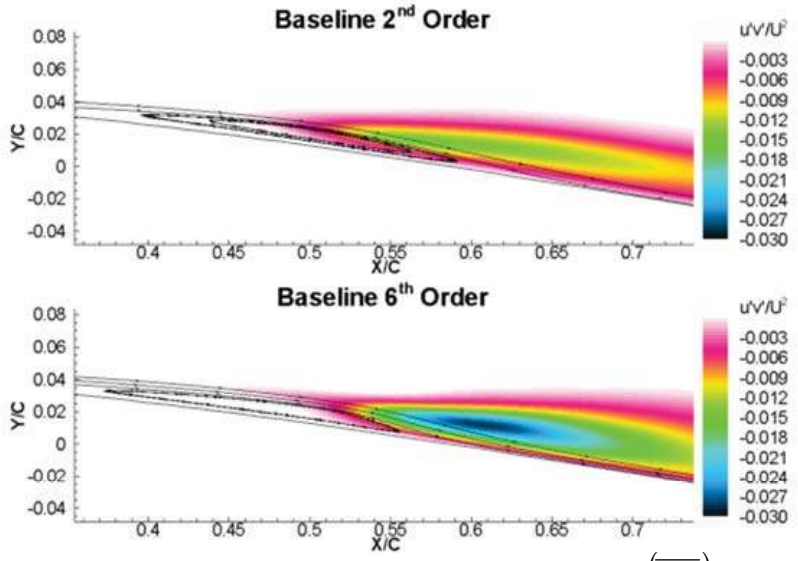

Figure 4.2: Effect of spatial discretization on Reynolds stress $\left(\overline{u'v'}\right)$ ($\alpha = 4°$, Re = 6x10^4)

Table 4.1: Computed LSB properties from the baseline mesh ($\alpha = 4°$, Re = 6x10^4)

Computation	Separation x_s/C	Transition x_t/C	Reattachment x_r/C	Max Bubble Height, h_b/C
Baseline 2nd-order	0.25	0.46	0.66	0.034
Baseline 6th-order	0.24	0.45	0.61	0.028

Separation, transition, and reattachment locations, as well as maximum LSB height for the two calculations are given in Table 4.1. Turbulent transition location is determined in accordance with Ref. 22 and is assumed to occur when the Reynolds stress reaches a value of 0.1% and exhibits a clear visible rise. Turbulent transition is also indicated by a drop in skin friction coefficient which coincides with a sharp pressure gradient observed after a flat pressure plateau typical of LSB's. As prescribed in Ref. 32, the maximum separation bubble height is defined as the distance from the surface to the velocity profile maximum at the edge of the shear layer. For both computations, the flow separates and transitions at approximately the same locations. However, reattachment location occurs further downstream for 2nd-order calculation. In addition, the 6th-order scheme predicts a smaller separation maximum bubble height.

Inspecting instantaneous flow structures are visualized with iso-surfaces of the Q-criterion in Figure 4.3. The Q-criterion provides the ability to visualize vortex cores and identify turbulent structures. In the subsonic regime, the Q-criterion is the Laplacian of the static pressure field over the density[70]

$$Q_{crit} = \frac{\nabla^2 P}{2\rho} \tag{4.1}$$

A limited number of relatively large vortical structures have formed from calculation with the 2nd-order scheme. Conversely, the 6th-order scheme predicts a larger number of finer scale vortical structures. These figures demonstrate the ability of the 6th-order scheme to resolve finer flow structures than the 2nd-order scheme on the same mesh.

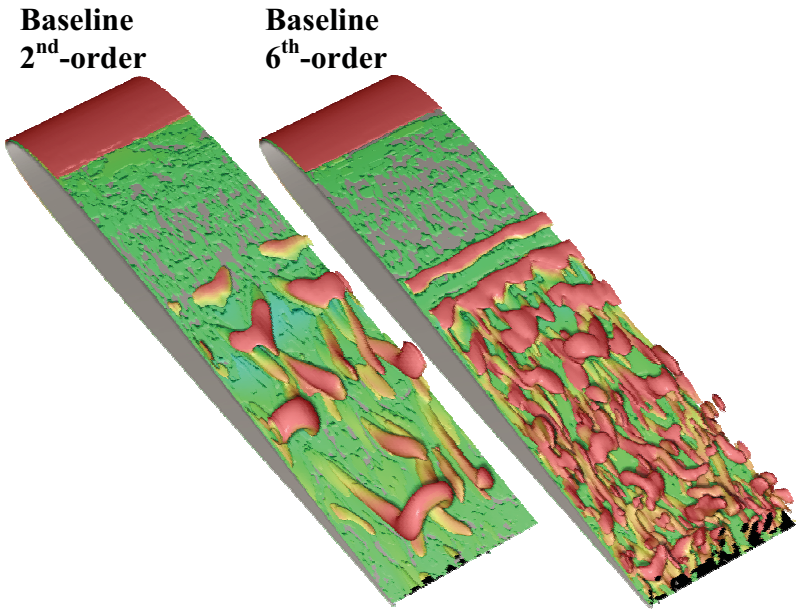

Figure 4.3: Effect of spatial discretization on 3-D instantenous iso-surface of Q-criterion for the baseline mesh (Q = 500, α = 4°, Re = 6x10^4)

4.2 Effect of Grid Resolution

Instantaneous and time-mean solutions obtained with the 6^{th}-order scheme with the baseline mesh and the three overset meshes are compared. Time-mean surface pressure and skin friction coefficients obtained with the four meshes are shown in Figure 4.4. Separation, transition, and reattachment locations along with maximum separation bubble height are given in Table 4.2. The pressure gradient in the transition regions is much sharper and occurs further downstream on the overset meshes compared to the baseline mesh. Consistently, the transition location occurs further upstream with the baseline mesh in comparison with three overset meshes. The surfaces pressures agree well between the three overset meshes with the largest discrepancies in sharp pressure recovery region between transition and reattachment locations. The skin friction coefficients agree favorably between the three overset meshes. However, the baseline mesh predicts a significantly shallower drop in skin friction. Consistent with the transition location, the drop in skin friction occurs further upstream in comparison with the overset meshes. The four meshes predict similar skin friction coefficient downstream of the reattachment locations.

Starker differences between the overset meshes in the magnitude of Reynolds stress are observed in contours of Reynolds stress shown in Figure 4.5. However, maximum magnitude of Reynolds stress differs by roughly 15%. Besides this discrepancy, the shape and extent of the Reynolds stresses are similar. The Reynolds stress contours for the baseline mesh agree favorably with the overset meshes.

Instantaneous flow structures visualized with iso-surfaces of Q-criterion and contours of spanwise vorticity are shown in Figures 4.6 and 4.7 for the baseline and three overset meshes. While the turbulent structures on the baseline mesh are reasonably isotropic over the airfoil, the structures on the overset meshes have a tendency to coalesce into larger structures. Furthermore,

the sizes of the fine scale structures are similar between the three overset meshes. Instantaneous contours of spanwise vorticity indicate that the free sear layer rolls up before transitioning to turbulent flow on the three overset meshes. However, this is not observed in the baseline calculation. These results indicate that even with the 6th-order scheme, fine details of transition are not captured on the coarser baseline mesh.

Given the similarities between solutions on the three overset meshes, and that the solution obtained on the original overset mesh agreed favorably with available experimental data as demonstrated in Chapter 5, the overset mesh was deemed adequate to resolve relevant flow features.

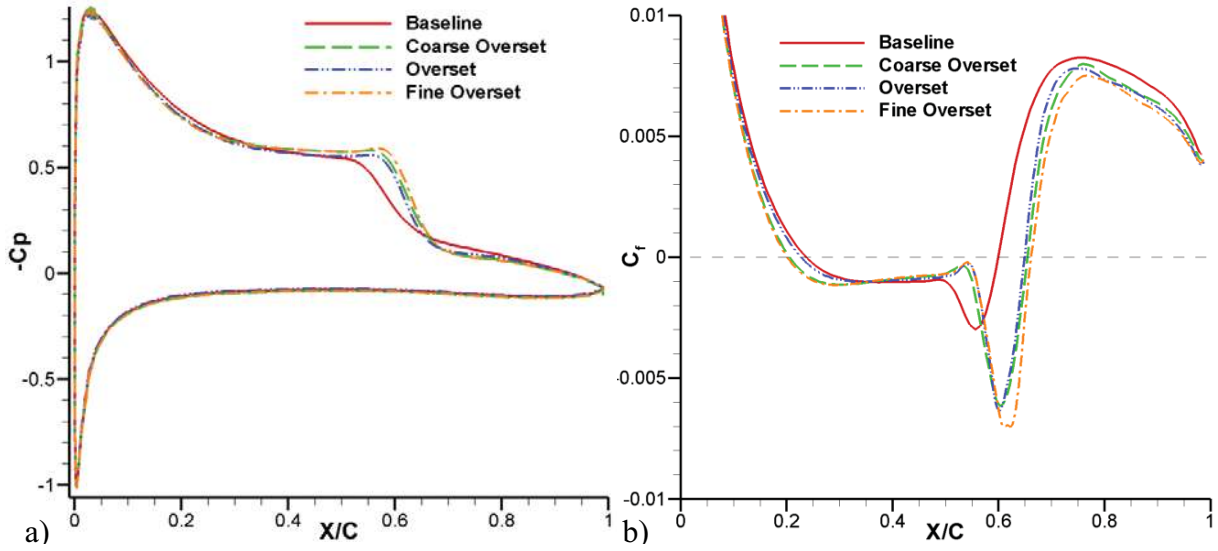

Figure 4.4: Effect of mesh resolution (α = 4°, Re = 6x10^4):
a) Mean surface *Cp* b) Mean surface C_f

Table 4.2: Computed LSB properties from the four meshes (α = 4°, Re = 6x10^4)

Computation	Separation x_s/C	Transition x_t/C	Reattachment x_r/C	Max Bubble Height, h_b/C
Baseline	0.24	0.45	0.61	0.028
Coarse Overset	0.20	0.52	0.65	0.033
Overset	0.23	0.55	0.65	0.030
Fine Overset	0.20	0.53	0.66	0.032

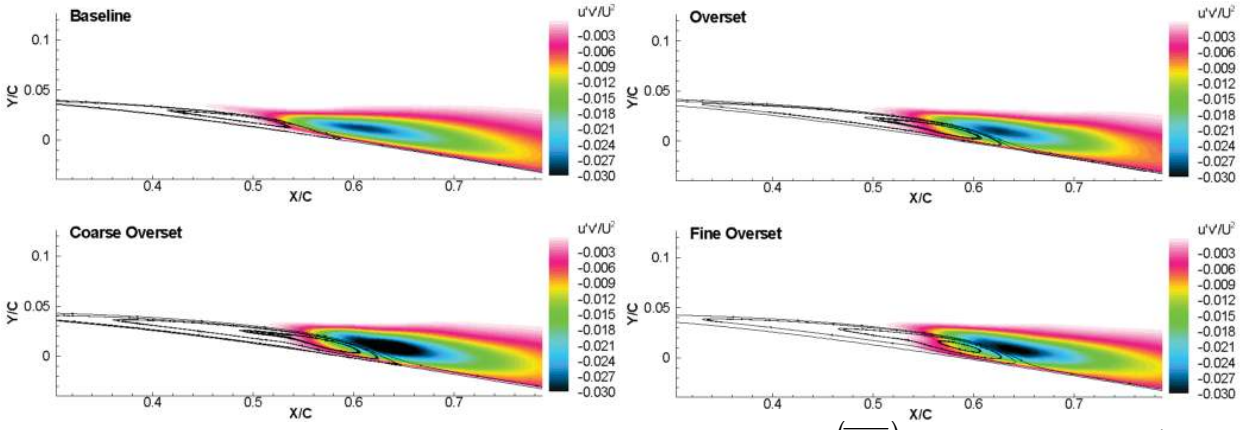

Figure 4.5: Effect of mesh resolution on Reynolds stress $\left(\overline{u'v'}\right)$ (α = 4°, Re = 6x10^4)

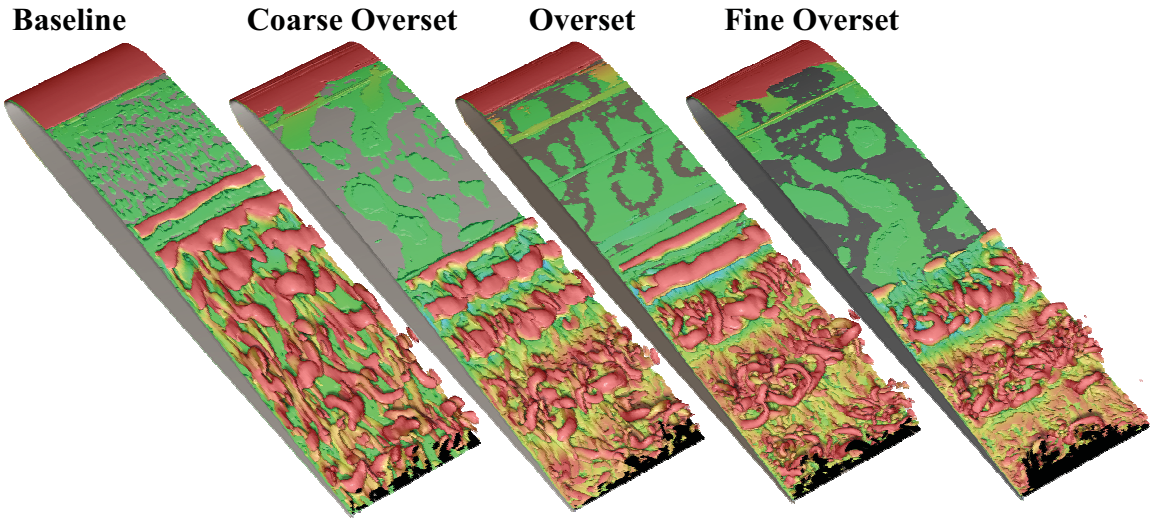

Figure 4.6: Effect of mesh resolution on 3-D instantenous iso-surface of Q-criterion (Q = 500, α = 4°, Re = 6x10^4)

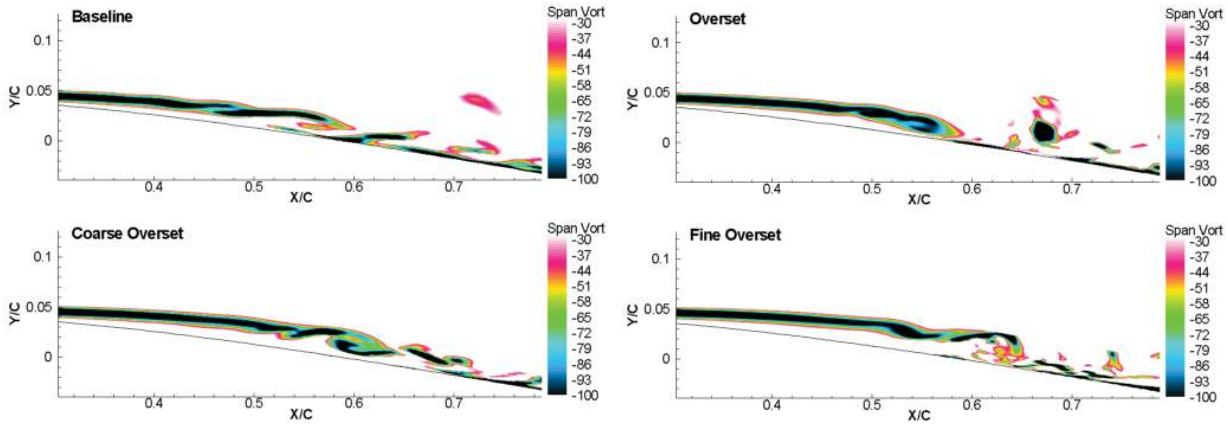

Figure 4.7: Effect of mesh resolution on instantanous contours of spanwise vorticity ($\alpha = 4°$, $Re = 6x10^4$)

4.3 Effect of Spanwise Extent

By imposing spanwise periodic boundary conditions, the three-dimensional mesh is represent a wing with infinite span. As such, spanwise extent is an important parameter in the computational setup. If the span is inadequate, the solution will be artificially constrained and flow structures will not properly develop. Conversely, even though an excessively large span will not impose any constraints on the flow it will incur an undesirable computational overhead. Therefore, a study was conduced using the overset mesh to determine an adequate spanwise extent.

Three spanwise extents were investigated (namely, 0.1, 0.2, and 0.3 fractions of chord) at an angle of attack of 4° and Reynolds number $6x10^4$. In terms of span over maximum bubble height ratio, the three spanwise extents are 3.3, 6.7, and 10. In order to eliminate the influence of spanwise spatial resolution, the number of grid points in the spanwise direction was modified such that the spacing remained approximately 0.002 for all cases.

Mean surface pressure and skin friction coefficients for the three spanwise extents are shown in Figure 4.8. Furthermore, contours of Reynolds stress are shown in Figure 4.9. Both surface

pressure and skin frication along with turbulent Reynolds stresses exhibit little variation for the different spanwise extents. These differences are expected given the irregular and chaotic nature of the turbulent transition of the shear layer.

Instantaneous three-dimensional flow structures are visualized with iso-surfaces of the Q-criterion for the three spanwise extents in Figure 4.10. The Q-criterion demonstrates flow structures of similar shape and size for all spanwise extents. Given the similarities between the three solutions, it is apparent that the spanwise extent of 0.1 is sufficient for this angle of attack and Reynolds number. However, after considering computational costs and the desire to compute a range of angles of attack and Reynolds numbers using the same mesh, the spanwise extent of 0.2 was retained.

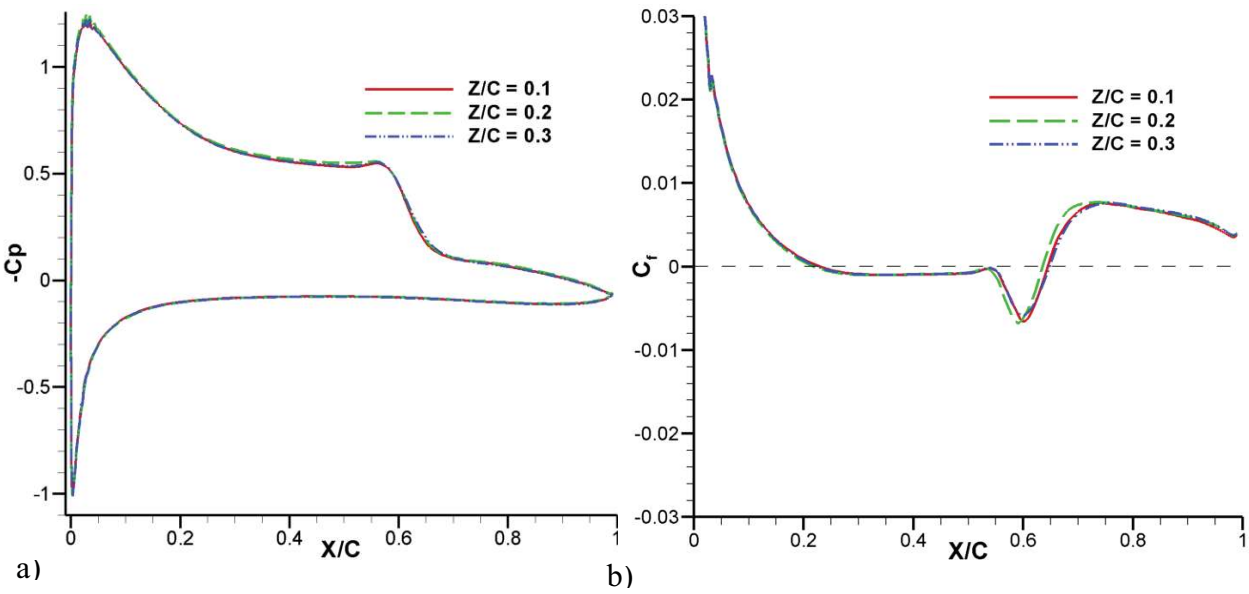

Figure 4.8: Effect of spanwise extent (α = 4°, Re = 6x10^4):
a) Mean surface *Cp* b) Mean surface C_f

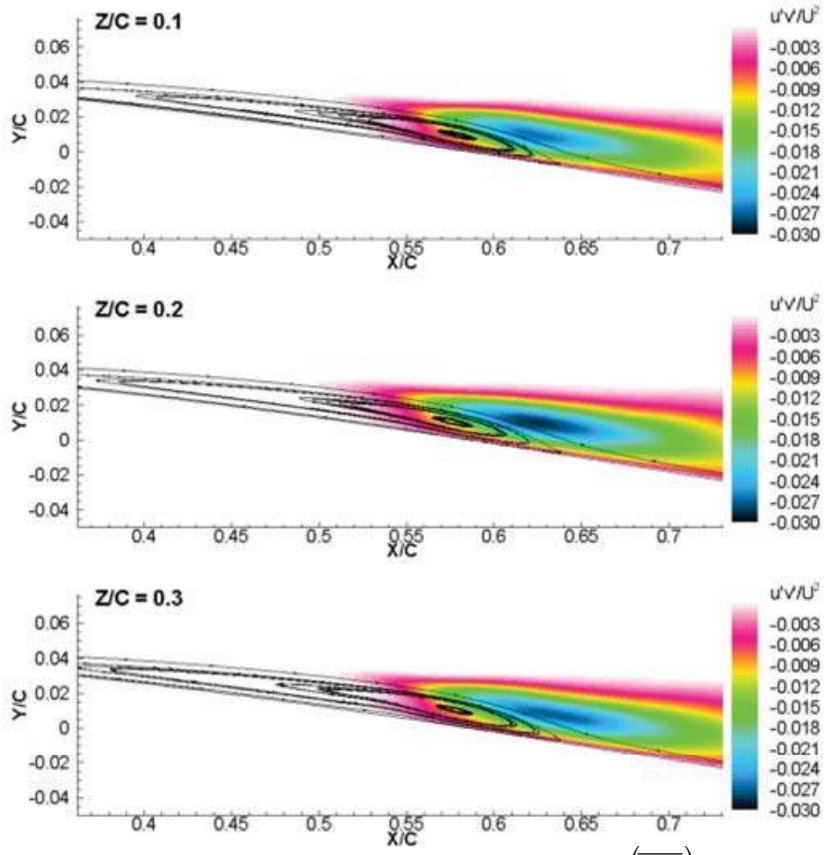

Figure 4.9: Effect of spanwise extent on Reynolds stress $\left(\overline{u'v'}\right)$ ($\alpha = 4°$, $Re = 6x10^4$)

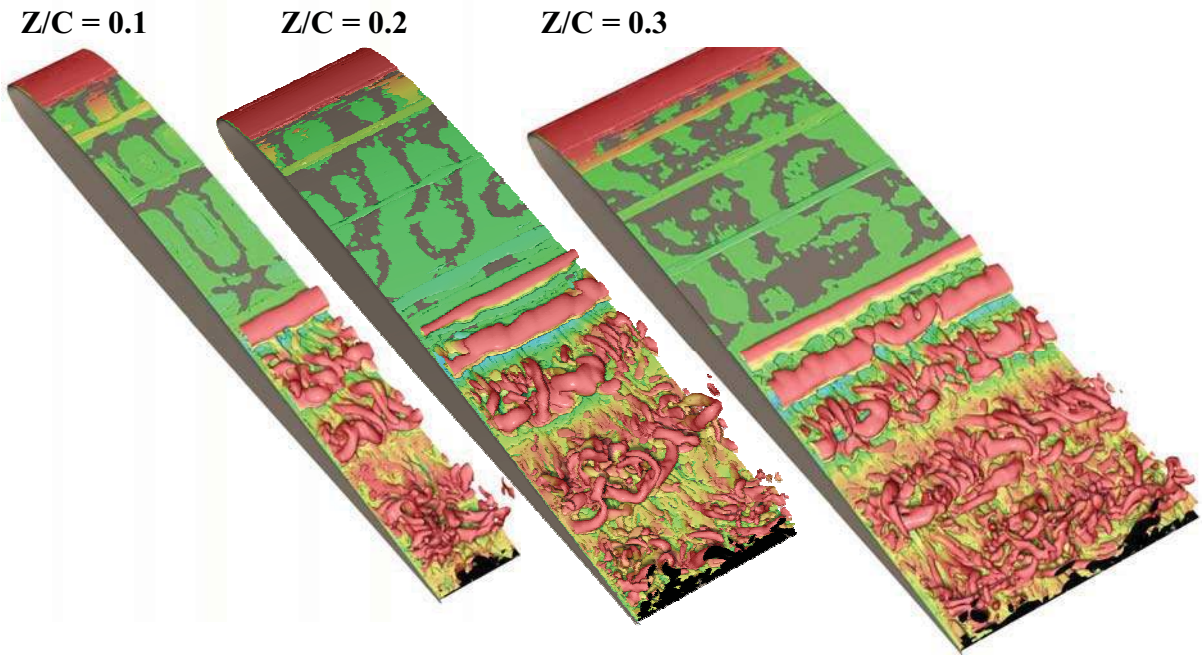

Figure 4.10: Effect of spanwise extent on 3-D instantenous iso-surface of Q-criterion ($Q = 500$, $\alpha = 4°$, $Re = 6x10^4$)

4.4 Effect of Spatial Dimensions

To demonstrate the necessity of three-dimensional computations, a two-dimensional solution was obtained with the overset mesh for 4° angle of attack and Reynolds number $6x10^4$. A comparison between the two-dimensional and three-dimensional (Z/C = 0.2) mean surface pressure and skin friction coefficients are shown in Figure 4.11. Contours of Reynolds stress for the two calculations are shown in Figure 4.12. The surface pressure coefficient of the two-dimensional solution agrees reasonably well with the three-dimensional solution. In addition, the size and extent of the two-dimensional solutions LSB is similar to that of the three-dimensional computations. However, the similarities end here. In terms of difference in the time-mean solution, the Reynolds stresses are more concentrated about the closure of the LSB in the two-dimensional solution. In addition, the skin friction coefficient from the two-dimensional solution does not rise to the same level of the three-dimensional solution downstream of the reattachment location. The most notable difference can be observed in contours of instantaneous spanwise vorticity component shown in Figure 4.13. In the two-dimensional solution, similar to observations by Hodge et al.[14], the shear layer rolls up into a coherent vortex that does not diminish significantly as it travels towards the trailing edge. It is evident that the two-dimensional solution restricts the decay of the vortex due to the lack of spanwise instabilities and vortex stretching.

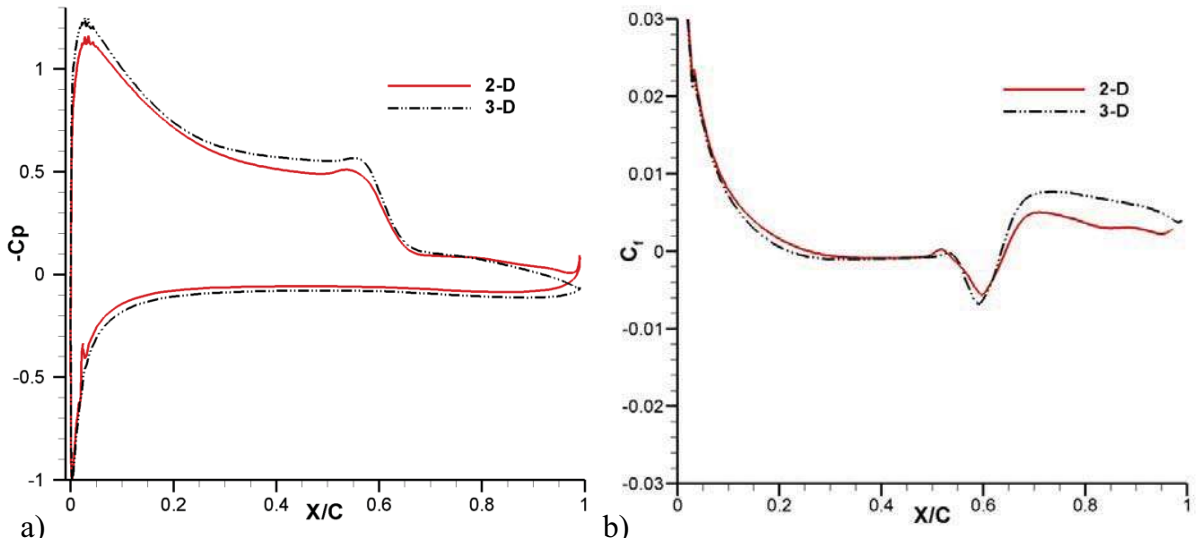

Figure 4.11: Effect of spatial dimenaionalty (α = 4°, Re = 6x10^4): a) Mean surface *Cp* b) Mean surface C_f

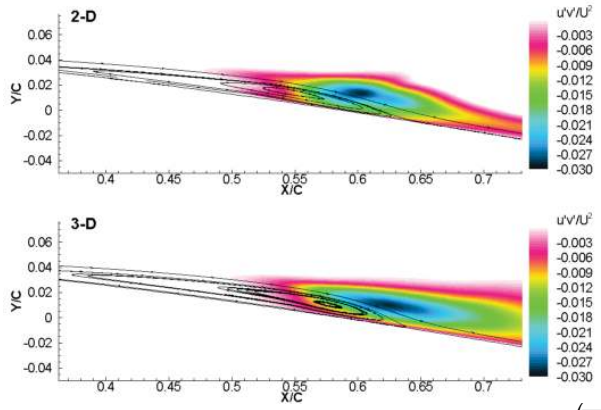

Figure 4.12: Effect of spatial dimenaionalty on Reynolds stress $\left(\overline{u'v'}\right)$ (α = 4°, Re = 6x10^4)

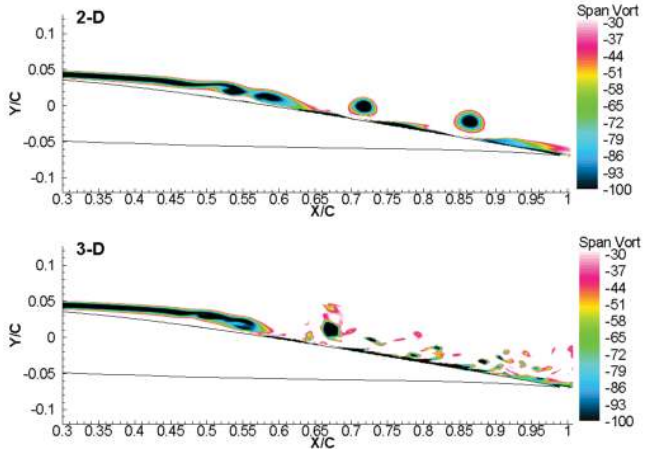

Figure 4.13: Effect of spatial dimensionality on spanwise vorticity

4.5 Effect of Mach Number

All experimental measurements were conducted under incompressible flow conditions. As FDL3DI solves the compressible Navier-Stokes equations, a reference Mach number is required. However, specifying a reference Mach number near zero for the compressible equations can induce numerical instabilities. In fact, computations at a Mach number of 0.05 produced spurious non-physical flow structures near the leading edge of the airfoil. The issue could be addressed with preconditioning for low Mach number flows; however no such methods have been implemented into FDL3DI. Experience with the solver has shown that a stable incompressible solution can be obtained with a reference Mach number of 0.1. To verify that this is a satisfactory low Mach number, a solution was computed with a reference Mach number of 0.075. Results using these two reference Mach numbers are compared in Figure 4.14 where few differences are observed in both mean surface pressure and skin friction coefficient. Similarly, contours of Reynolds stress agree favorably as shown in Figure 4.15. Again, given the irregular nature of the turbulent transition, these differences are acceptable. Separation, transition, and reattachment locations closely agreed between the two solutions. To emphasize the incompressible nature of the solutions, the minimum and maximum non-dimensional density was 0.99 and 1.01 respectively. Therefore, a Mach number of 0.1 was prescribed for all angles of attack and Reynolds numbers.

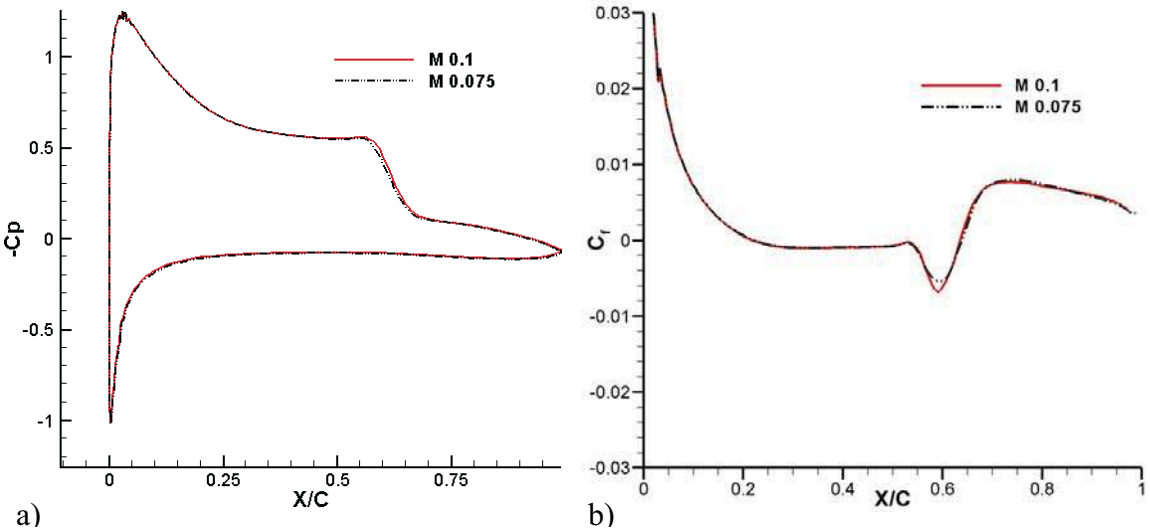

Figure 4.14: Effect of Mach number (α = 4°, Re = 6x10^4): a) Mean surface *Cp* b) Mean surface C_f

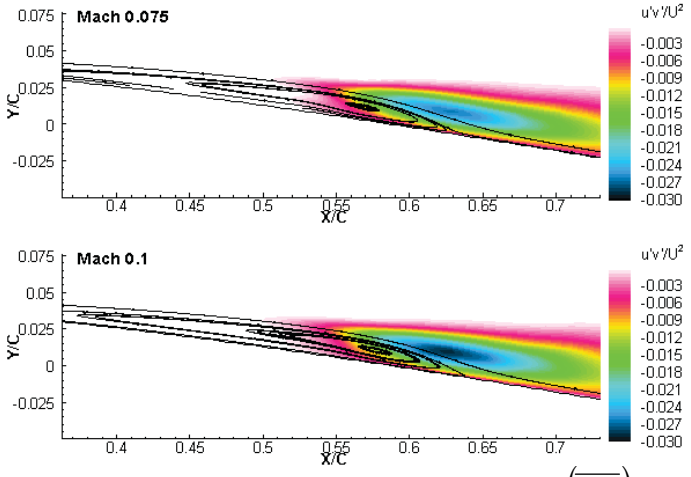

Figure 4.15: Effect of Mach number on Reynolds stress $\left(\overline{u'v'}\right)$ (α = 4°, Re = 6x10^4)

5 Results

5.1 Comparison with Time-mean Experimental Data

Computed contours of Reynolds stresses and spanwise vorticity for the available angles of attack of 4°, 8°, and 11° are compared with TU-BS and HFWT experimental measurements in Figures 5.1 and 5.2 respectively. For angles of attack of 4° and 11°, computed and measured Reynolds stresses agree well in terms of shape, magnitude, and extent. Similarly for spanwise

vorticity contours, general shape and extent of the computed shear layer differs little from experimental measurements. However, discrepancies with all three data sets are observed at 8° angle of attack. In particular, HFWT data does not exhibit a notable separation bubble.

Initially, Ol et al. speculated that the lack of a recirculation region in the experimental data could come from increased freestream turbulence intensity, or a shortcoming of the PIV image pairs for adequate convergence of flow statistics; or both. During later experimental measurements, it was discovered that the model had a tendency to vibrate at this particular angle of attack which likely caused the flow to transition prematurely effectively eliminating the LSB.*

While the computed Reynolds stress is comparable in magnitude to that measured in the TU-BS water tunnel for 8° angle of attack, transition along with reattachment occurs further downstream resulting in a longer LSB than observed in the experiment. Similar trends were observed in computations by Radespiel et al.[22] and Yuan et al.[24] These differences are likely caused by the higher freestream turbulence intensity of the TU-BS water tunnel of approximately 0.8%. Alternatively, the discrepancy could be attributed to a disparity in effective angle of attack due to interference effects in the water tunnel. A slightly higher angle of attack would lead to a smaller separation bubble closer to the leading edge of the airfoil. However, no attempts were made to investigate a discrepancy in angle of attack. Finally, this particular measurement was taken during an earlier experimental campaign with a lower PIV image resolution.

*Personal communication with Dr. Ol.

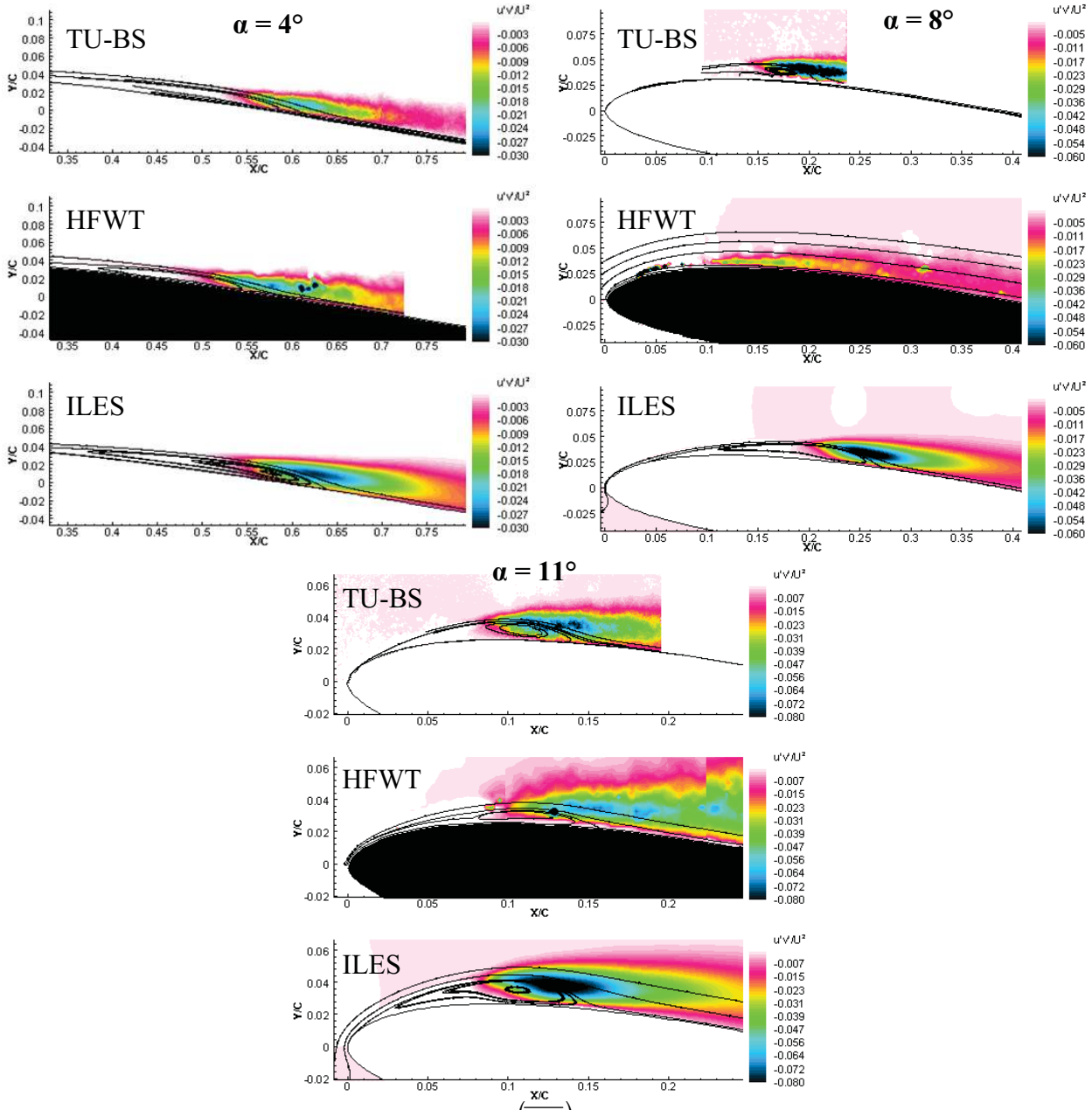

Figure 5.1: Reynolds stress $\left(\overline{u'v'}\right)$ and experimental PIV data for α = 4°, 8°, 11° at Re = 6x10^4

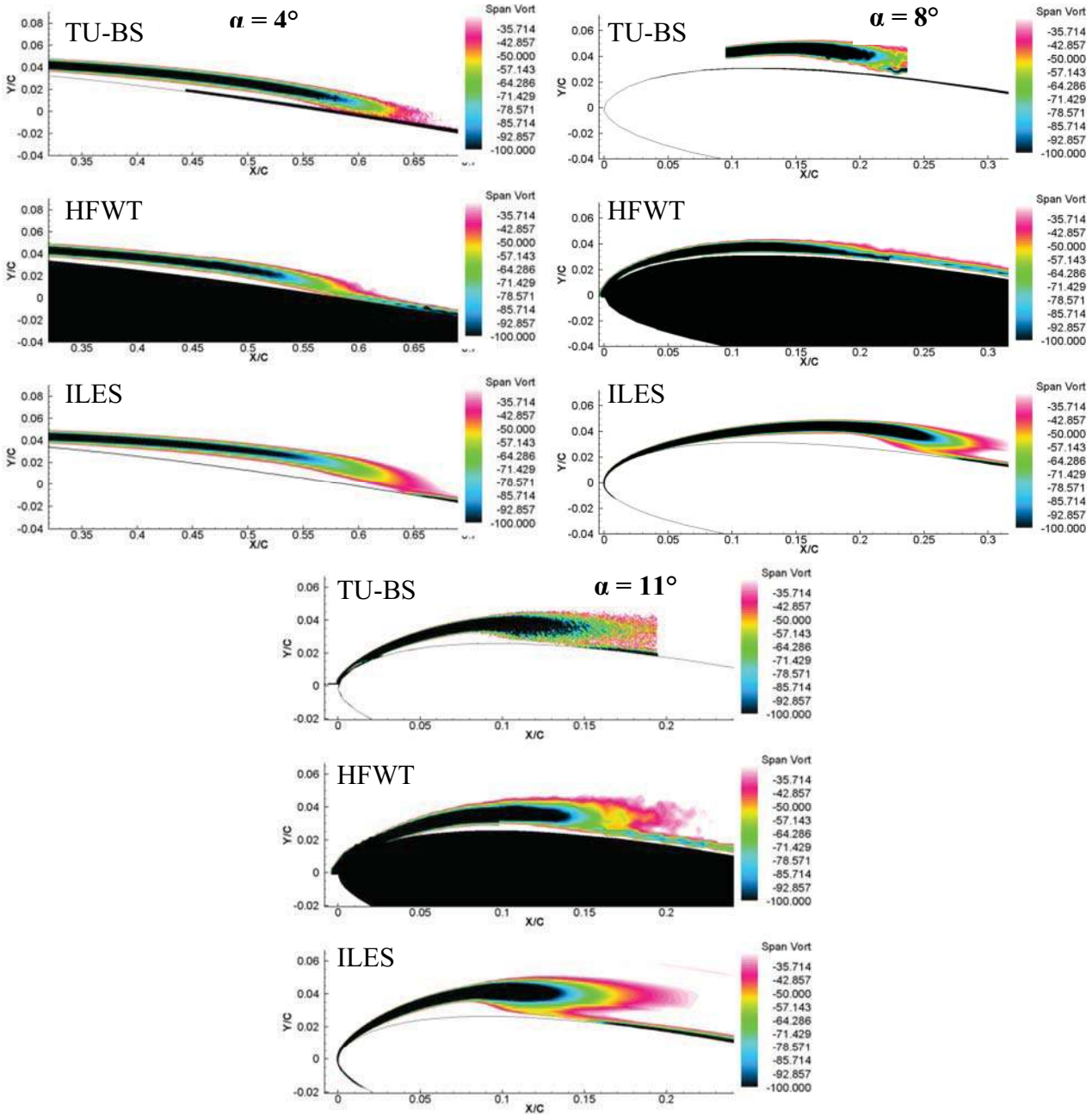

Figure 5.2: Spanwise vorticity and experimental PIV data for α = 4°, 8°, 11° at Re = 6x10^4

Even though the computed LSB at 11° angle of attack is slightly thicker than observed in both experiments, separation, transition, and reattachment locations agree well as shown in Table 5.1. As the airfoil is near stall, a greater pressure recovery is required to cause the LSB to reattach. Such a strong pressure gradient amplifies disturbances resulting in a rapid transition to form the short LSB. In contrast to the 8° angle of attack, it is evident that the higher freestream turbulence intensity in the TU-BS water tunnel does not lead to an earlier transition at 11° angle of attack.

Boundary layer profiles normal to the airfoil surface, shown in Figures 5.3 through 5.5, were extracted from the ILES solution and both experimental PIV measurements. The ILES solution was interpolated onto a body-fitted orthogonal mesh with the same 6^{th}-order accurate interpolation scheme used for the overset interpolation. Experimental data was transferred to the body fitted orthogonal mesh through linear interpolation. For simplicity, the u-velocity component for the profiles rather than the tangential velocity component. Only a select number of profiles are given and the velocity component displayed with different scale factors for each angle of attack. Following the profiles from the leading edge, for each angle of attack, the upstream laminar profile separates to an S-shaped profile which subsequently transforms to a fuller turbulent profile. The computed ILES profiles consistently predict a slightly thicker and longer separation region compared with experimental measurements. Despite the aforementioned discrepancies, good overall agreement is found between experiments and computation.

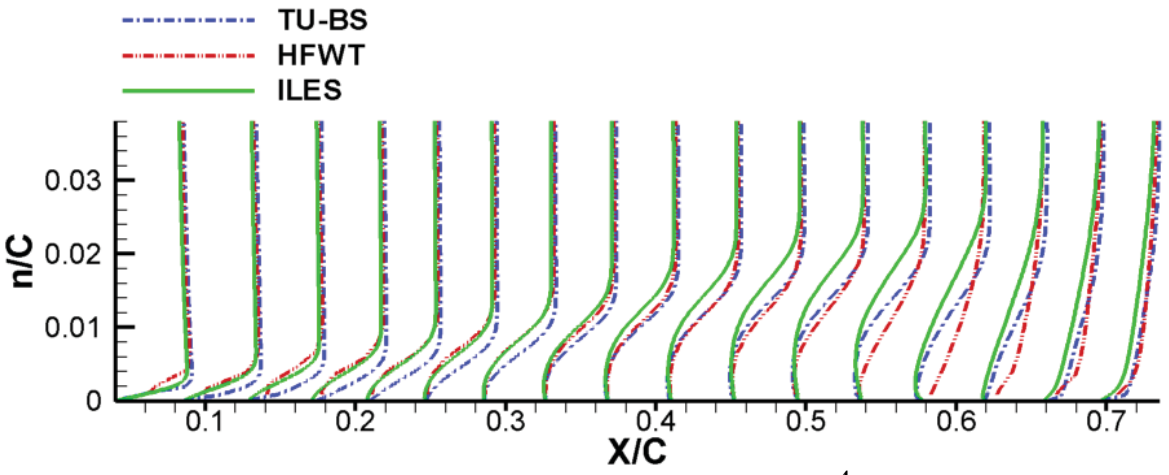

Figure 5.3: Boundary layer profiles at α = 4°, Re = 6x10^4 (scaled by 0.045)

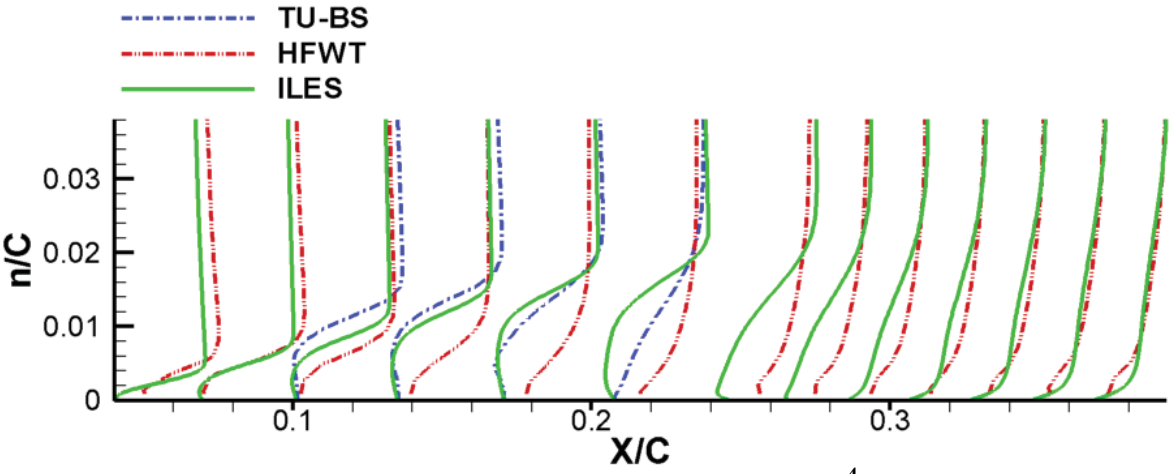

Figure 5.4: Boundary layer profiles at α = 8°, Re = 6x10^4 (scaled by 0.02)

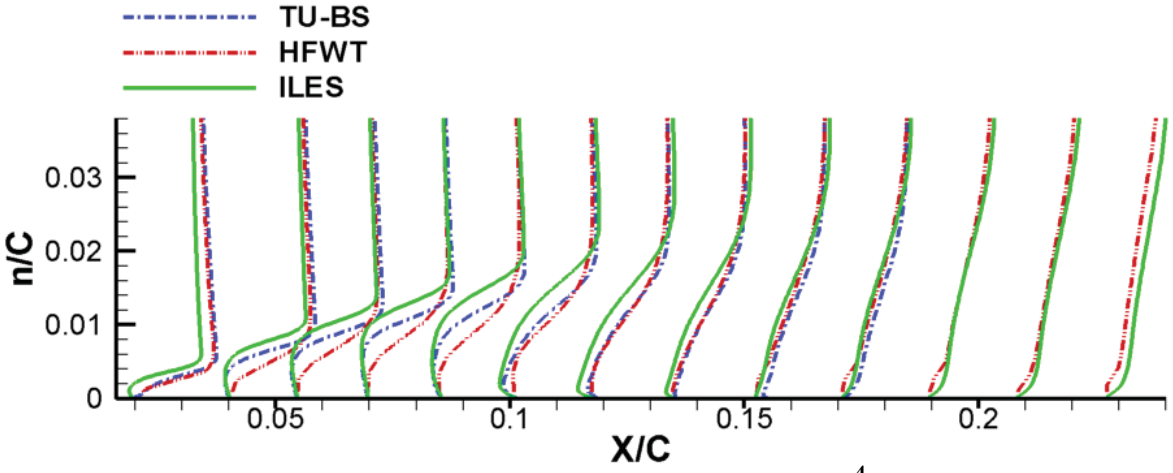

Figure 5.5: Boundary layer profiles at α = 11°, Re = 6x10^4 (scaled by 0.01)

Table 5.1 compares separation, transition, reattachment, and maximum LSB height at 4° angle of attack measured from the two experimental facilities along with simulations by Yuan et al. [24] and Lian et al.[23] and the present ILES and XFOIL[19] computations. A critical N-factor of 8 was used for the RANS-e^N calculations by Yuan et al. and Lian et al., as well as the XFOIL calculation, based on the empirical relationship between freestream turbulence intensity and critical N-factor by Mack[71]

Both XFOIL and ILES computations place the separation location in between the two experimental measurements. The relatively large disparity in the experimentally measured separation location is due in part to difficulties in determining a separation location from near-wall PIV measurements of shallow separation regions. The ILES separation location of 23% is in agreement with separation locations determined by LES and RANS-e^N method calculations by Yuan et al. and Lian et al. A transition location of 55% chord predicted by the ILES computation agrees well with the measured TU-BS transition location of 53% chord. Transition at the HFWT tunnel was measured at 47% chord which is consistent with slightly higher freestream intensity in this facility of ~0.1% compared to 0.08% of the TU-BS low-noise wind tunnel. The influence of freestream turbulence intensity on the ILES solution was not investigated. Reattachment locations are also in agreement between ILES and TU-BS at 65% chord and 62% chord respectively. Reattachment measured at HFWT occurs slightly further upstream at 58%. Finally, the maximum height of the LSB differs little between both experimental measurements and ILES computations.

Table 5.1: Measured and computed LSB properties ($\alpha = 4°$, $Re = 6x10^4$)

Data Set	Freestream Turbulence [%]	Separation x_s/C	Transition x_t/C	Reattachment x_r/C	Max Bubble Height, h_b/C
TU-BS	0.08	0.30	0.53	0.62	0.028
HFWT	~0.1	0.18	0.47	0.58	0.029
Yuan SGS-LES	0	0.25	0.49	0.60	-
Yuan RANS-e^N	0.1, N=8	0.21	0.49	0.58	-
Lian RANS-e^N	0.1, N=8	0.21	0.48	-	-
XFOIL	0.1, N=8	0.21	0.55	0.59	-
ILES	0	0.23	0.55	0.65	0.030

A sequence of spanwise averaged instantaneous surface pressure coefficients are shown in Figure 5.6. Contours of instantaneous spanwise vorticity component for the corresponding time sequence is shown in Figure 5.7. The instantaneous surfaces pressure follows the average surface pressure up to roughly X/C = 0.5, which is slightly upstream of the transition location. Downstream of X/C = 0.5, the surface pressure begins to deviate from the mean, consistent with the rollup of the shear layer observed in the instantaneous spanwise vorticity contours. Furthermore, the peaks in low surface pressure coincide with the relatively coherent vortex that has been shed from the shear layer and can be observed traversing downstream from the contours of spanwise vorticity.

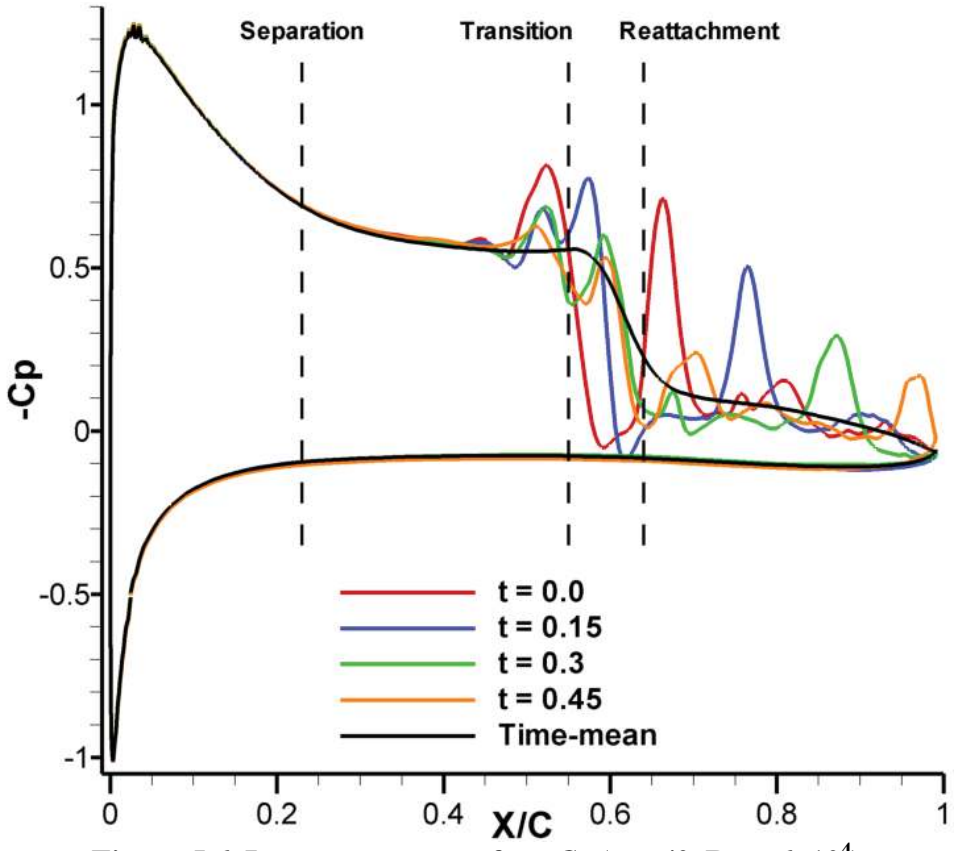

Figure 5.6: Instantaneous surface *Cp* (α = 4°, Re = 6x10^4)

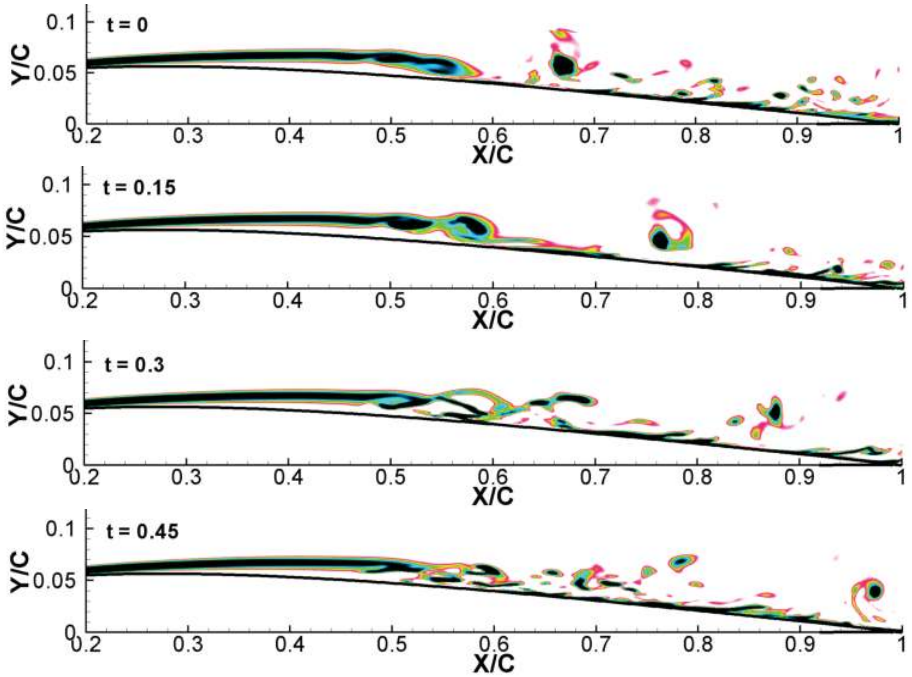

Figure 5.7: Instantanous contours of spanwise vorticity component (α = 4°, Re = 6x10^4)

To inspect the transition into turbulence, velocity probes were positioned at the mid-span over a number of streamwise locations along the suction surface of the airfoil at 4° angle of attack and Reynolds number $6x10^4$. At each streamwise location, the probes were positioned at approximately half the local time-mean boundary layer height. Streamwise velocity energy spectra are plotted from three probes in Figures 5.8 and 5.9 respectively. Furthermore, mean velocity profiles at the three locations are shown in Figure 5.10. For completeness, both original and normalized boundary layer profiles are shown. The boundary layer profiles are normalized based on 99.5% boundary layer thickness and boundary layer edge velocity.

Upstream of the separation location at $X/C = 0.1$, the velocity energy spectrum has a low energy content indicating small fluctuations in the solution which is consistent with the thin laminar boundary layer observed in Figure 5.10. After separation, the velocity energy spectrum at $X/C = 0.5$ increases (note the change in scales of Figure 5.8). This increase in fluctuations is consistent with the presence of the LSB and reversed flow at $X/C = 0.5$ indicated by the S-shaped boundary layer profile. Furthermore, while observable at $X/C = 0.1$, a distinct frequency of $F^+ = 5.8$ emerges in the velocity spectrum at $X/C = 0.5$. This frequency is likely associated with the shedding frequency of the shear layer vortex rollup which also occurs at roughly $X/C = 0.5$. However, a sufficient amount of time accurate images of the flow field were not gathered to conclude this. Higher harmonics of the dominant shear layer frequency are not present.

For a chord length of 200 mm, as used in experiments by Radespiel et al.[22], $F^+ = 5.8$ corresponds to a frequency of 129 Hz in air and 8.7 Hz in water. This is consistent with RANS-e^N calculations by Radespiel et al. where numerical oscillations were observed at a frequency of 125 Hz and 8.5 Hz for air and water respectively. These findings also agree reasonably well with the experimental measurements in the TU-BS water tunnel where 2D waves were observed

with time resolved high resolution PIV to have a frequency of 12 Hz. Non-dimensionalized, 12 Hz in water corresponds to $F^{+} = 8$.

At $X/C = 0.95$, downstream of the LSB reattachment, the velocity energy spectrum resembles that of a turbulent boundary layer with a limited emerging inertial range. A fuller turbulent boundary layer profile is also observed in Figure 5.10 consistent with the energy spectrum. In addition, a dominant shedding frequency is no longer distinguishable from the velocity spectrum.

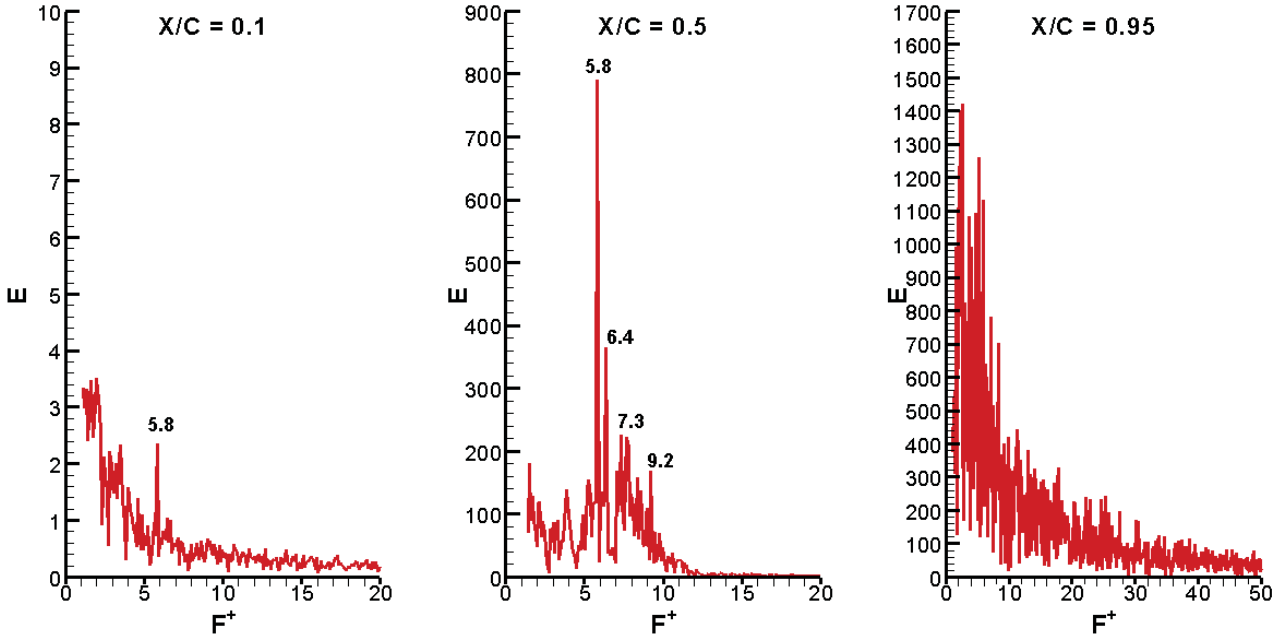

Figure 5.8: Streamwise velocity component energy spectra on linear scales

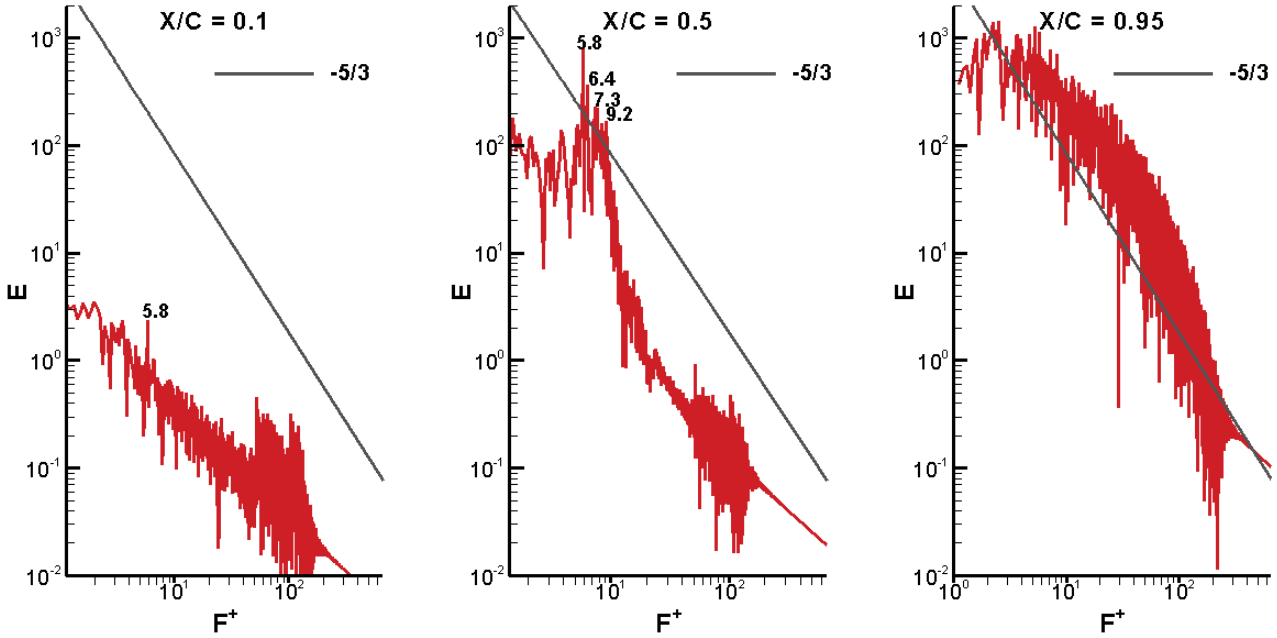

Figure 5.9: Streamwise velocity component energy spectra on log log scales

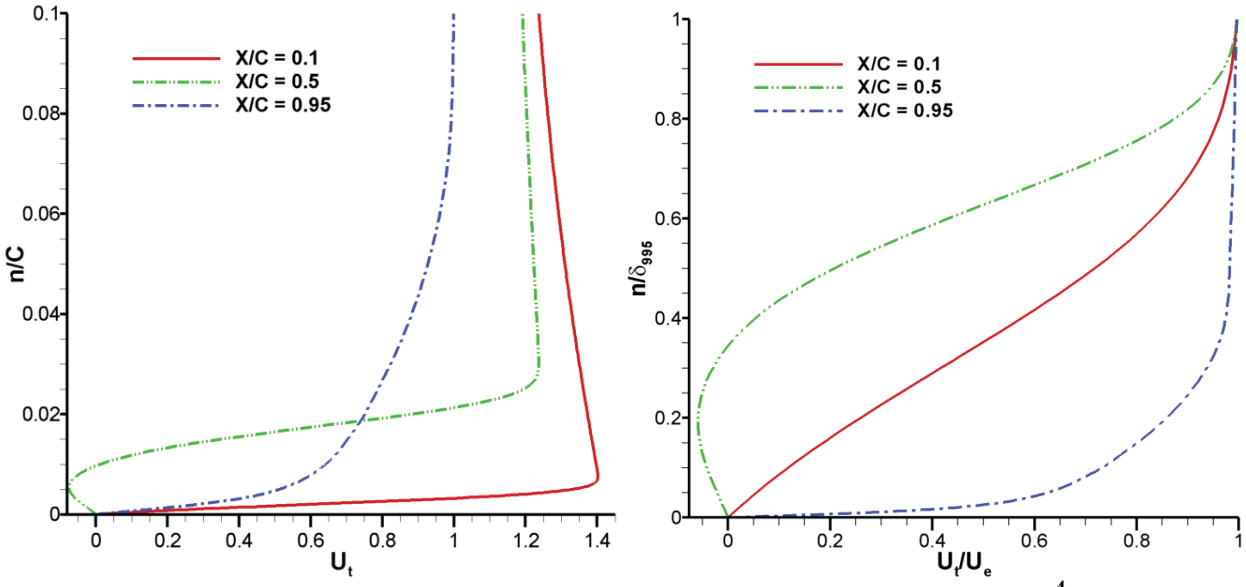

Figure 5.10: Mean tangential velocity profiles ($\alpha = 4°$, $Re = 6x10^4$)

5.2 Effect of Angle of Attack at Fixed Reynolds Number

Solutions were obtained at angles of attack 2°, 4°, 6°, 8°, 11°, and 14° at Reynolds number $6x10^4$. Lift and drag coefficients were obtained from the ILES solutions by integrating mean pressure and skin friction over the surface of the airfoil. In order to accurately perform the integration in overlapping regions of the overset mesh, the solution was first transferred to a single mesh, i.e. the baseline mesh. As points did not necessarily coincide in the refined region of the suction surface of the airfoil, linear interpolation was used to transfer the solution.[72] Because linear interpolation was used to solely transfer surface data, which was subsequently integrated, the low order interpolation was not expected to degrade the quality of the computed lift and drag.

Integrated lift and drag coefficients are compared in Figure 5.11 with computed values from XFOIL and experimental measurements of Selig et al.[33, 34] and Ol et al.[32] Computations with XFOIL slightly over predict but generally agree well with experimental measurements up to stall. While drag coefficients from the ILES calculations slightly over estimated measurements

by Selig et al., ILES lift coefficients agree well with experimental measurements. Stall is predicted at 11° angle of attack by the ILES computations consistent with measurements by Ol et al. Most notably, the post stall lift coefficient at 14° angle of attack agrees well with the measured lift coefficient. Accurate lift and drag predictions are challenging to obtain with traditional transition and turbulence modeling for massively separated flows past stall angles of attack. However, investigations into dynamic motions such as plunging airfoil requires accurate modeling of massively separated flows induced by the motion of the airfoil. Furthermore, unlike traditional methods, the evolution from a closed LSB to bubble bursting and stall was seamlessly captured by the ILES model without modification to any parameters.

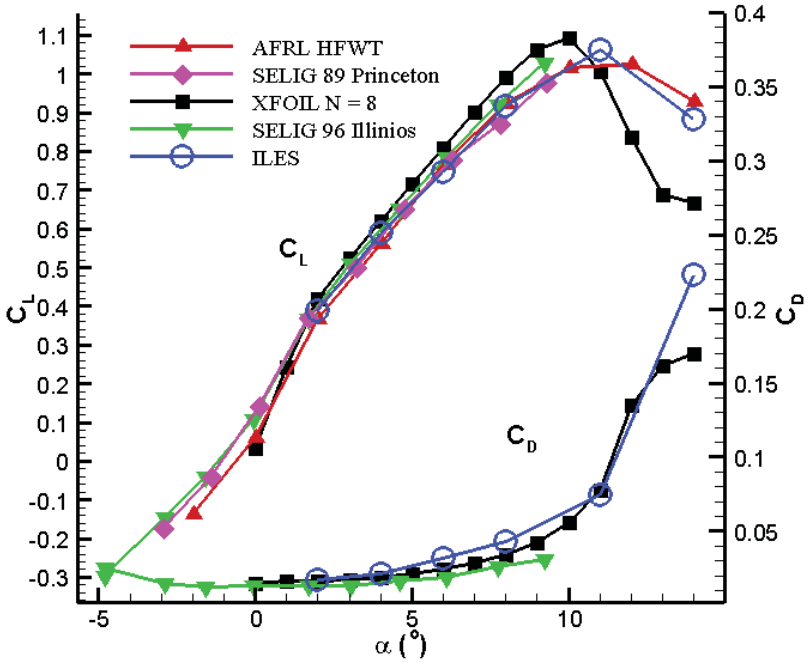

Figure 5.11: Comparison of ILES lift and drag polars with XFOIL and experimental measurements

Mean surface pressure coefficient, skin friction coefficient, Reynolds stresses, and spanwise vorticity for all angles of attack computed are presented in Figures 5.12 through 5.15. At the lowest angle of attack of 2°, a long LSB forms, the flow begins to transition to turbulent flow

near the trailing edge, and reattaches at 93% chord. Consistent with experimental findings, as the angle of attack increases, the adverse pressure gradient grows and pressure plateau of the LSB shortens as shown in Figure 5.12. As a result, separation, turbulent transition, and reattachment locations, summarized in Table 5.2, move upstream. As shown in Figure 5.13, the transition location, characterized by the sudden drop in skin friction, moves towards the leading edge with increasing angle of attack. It is noteworthy that the sharp rise in skin friction coefficient downstream of the transition location is consistent with experimental observations and is challenging to obtain with RANS calculations.[73]

As the LSB moves towards the leading edge, shown in Figure 5.14, the increasing magnitude of Reynolds stresses is indicative of a more intense turbulent transition process causing the reattachment location to move upstream. When the airfoil is fully stalled at 14° angle of attack, the Reynolds stress drops, the spanwise vorticity indicates that the free shear layer does not reattach to the surface, and the mean surface pressure is characteristically flat across the entire suction side of the airfoil.

Instantaneous flow features visualized with iso-surfaces of the Q-criterion are shown in Figure 5.16 for all angles of attack. As the separated shear layer breaks down, a coherent spanwise vortex forms over the extent of the airfoil and, due to spanwise instabilities, subsequently breaks down into turbulent structures. With increasing angle of attack, the formation of the spanwise vortex moves towards the leading edge and breaks down after traveling shorter distances. However, the size of the turbulent structures does not change drastically with increasing angle of attack.

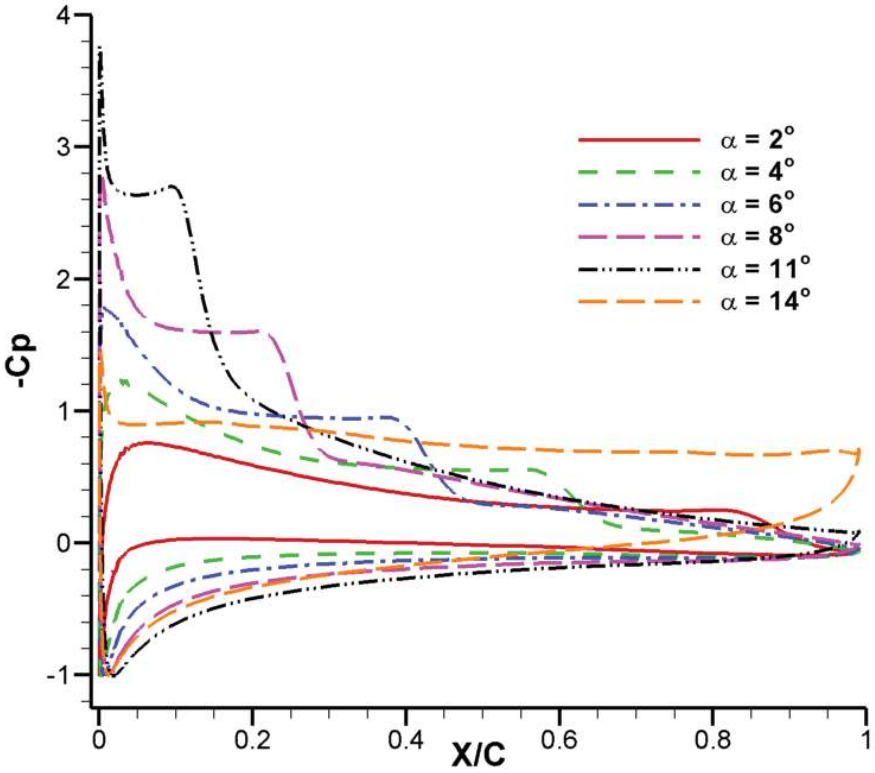

Figure 5.12: Effect of angle of attack on mean surface *Cp* (Re = 6x10^4)

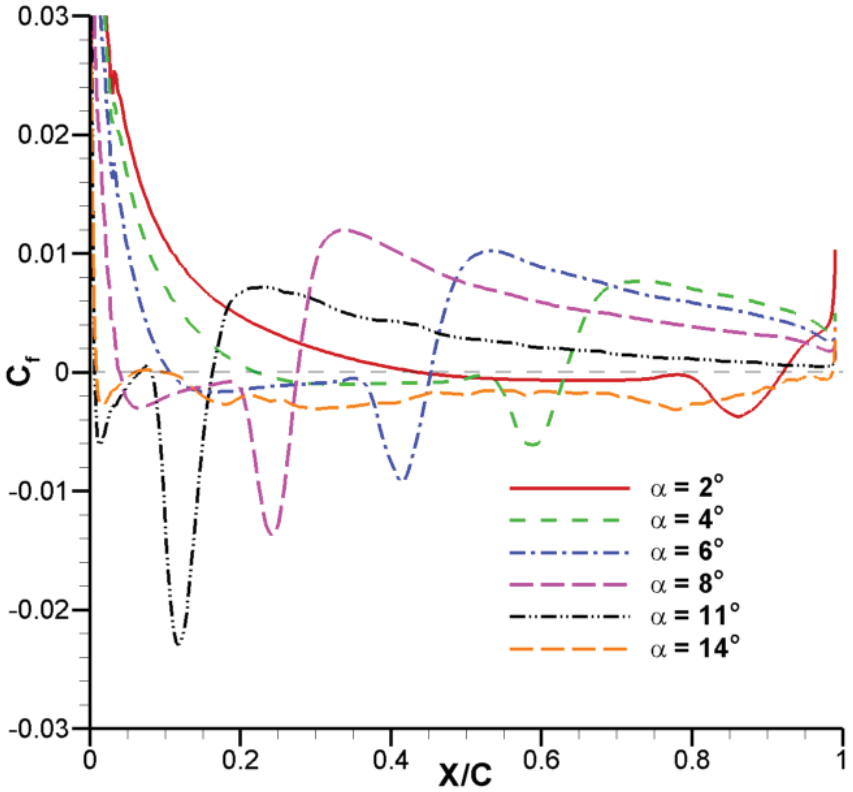

Figure 5.13: Effect of angle of attack on mean suction surface C_f (Re = 6x10^4)

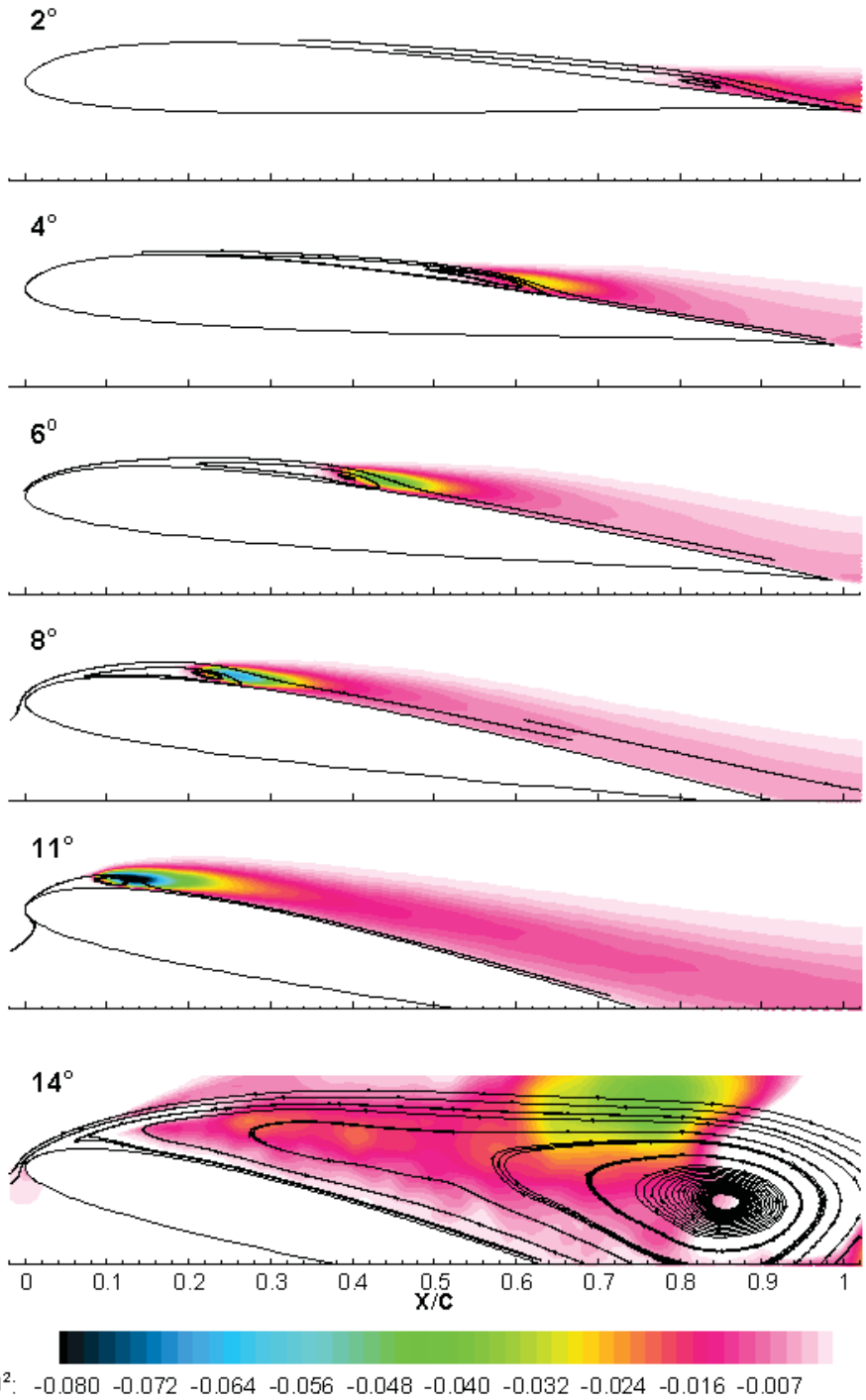

Figure 5.14: Effect of angle of attack on Reynolds stress $\left(\overline{u'v'}\right)$ (Re = 6x10^4)

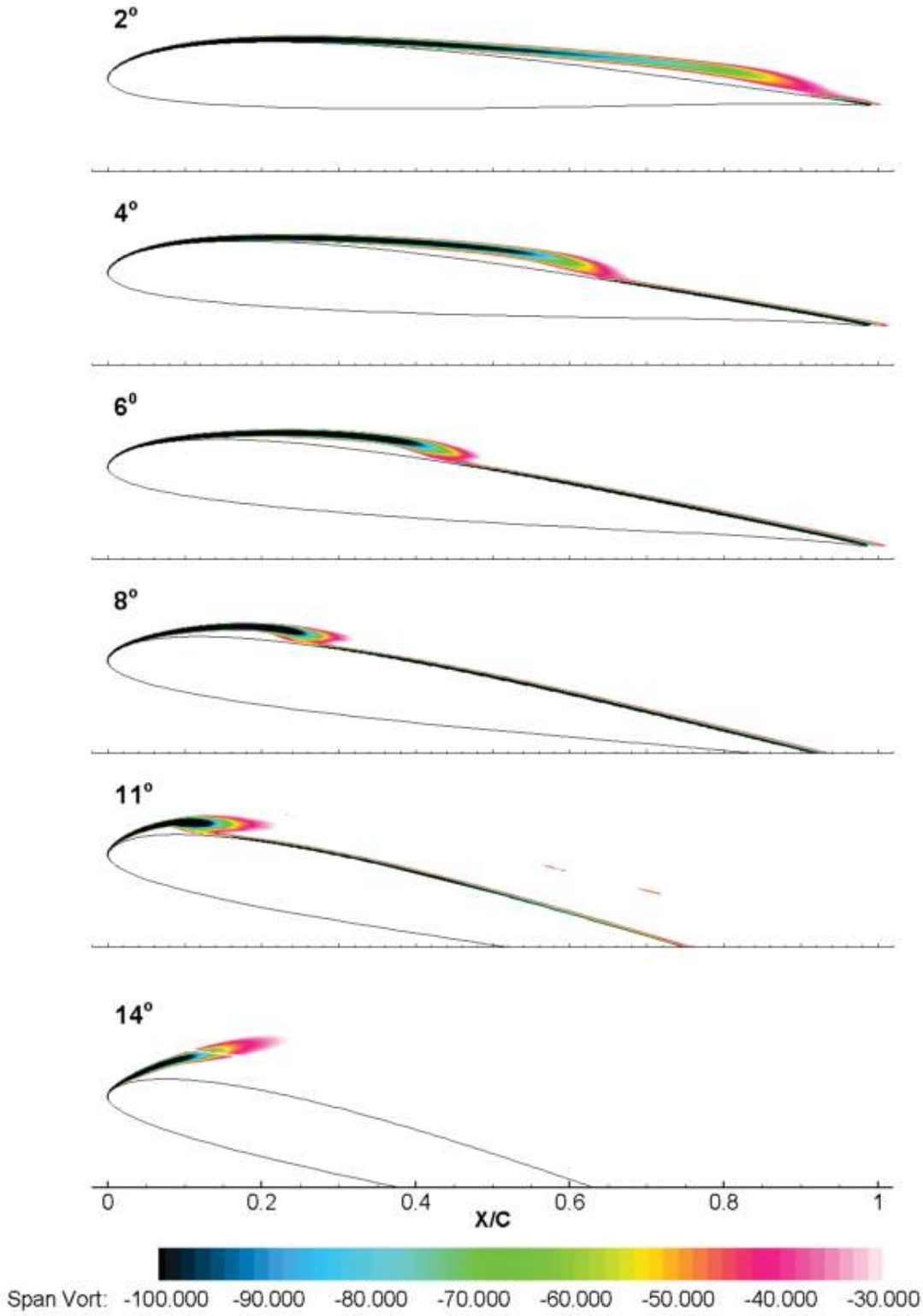

Figure 5.15: Effect of angle of attack on spanwise vorticity component (Re = $6x10^4$)

Table 5.2: Effect of angle of attack on LSB properties at Re = $6x10^4$

α Degrees	Separation x_s/C	Transition x_t/C	Reattachment x_r/C	Max Bubble Height, h_b/C
2	0.45	0.74	0.92	0.036
4	0.23	0.55	0.65	0.030
6	0.11	0.34	0.45	0.028
8	0.04	0.18	0.28	0.027
11	0.007	0.06	0.16	0.025
14	0.01	-	-	-

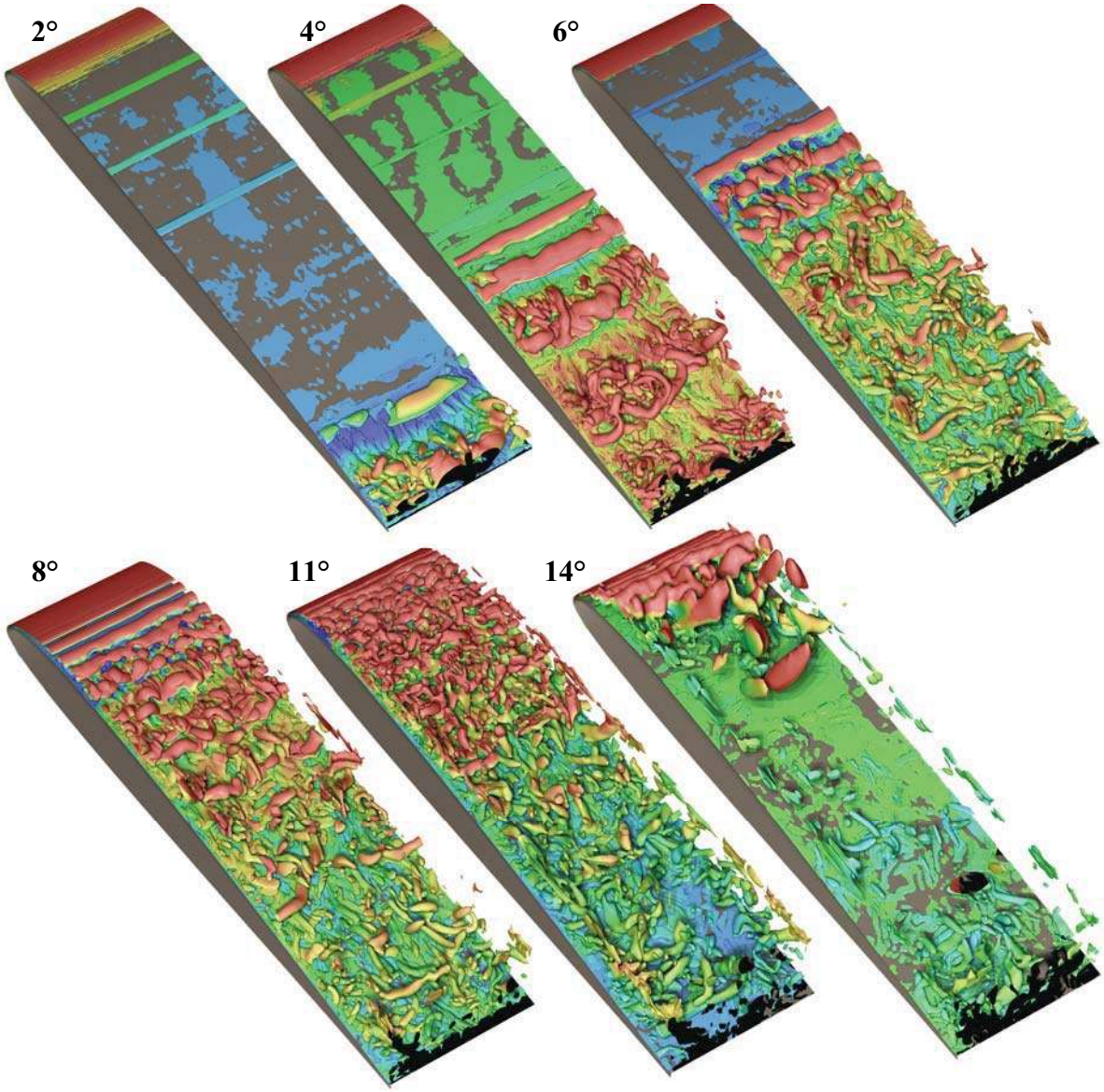

Figure 5.16: Effect of angle of attack on 3-D instantaneous iso-surfaces of Q-criterion (Q = 500, Re = $6x10^4$)

5.3 Effect of Reynolds Number at Fixed Angle of Attack

Two series of Reynolds numbers at fixed angles of attack were computed. In the first series, two additional Reynolds numbers of 10^4 and $4x10^4$ were computed at 4° angle of attack. The second series included Reynolds numbers ranging from 10^4 to $9x10^4$ at 8° angle of attack.

Contours of Reynolds stress and spanwise vorticity for both angles of attack are given in Figures 5.17 and 5.18. In addition, time and spanwise mean surface pressure and skin friction coefficients are given in Figures 5.19 and 5.20. For the lowest Reynolds number of 10^4, the shear layer does not reattach at either angle of attack. For the 4° angle of attack, the Reynolds stress and vorticity contours show the shear layer rolling up near the trailing edge of the airfoil. The pressure coefficient has a weak suction peak followed by a relatively flat distribution over the airfoil. The skin friction coefficient has a sudden drop near the trailing edge associated with the rollup of the shear layer. At 8° angle of attack, the spanwise vortex formed by the shear layer rolling up does not break down rapidly and remains relatively coherent over the streamwise extend of the airfoil. This can be observed in the instantaneous iso-surface of the Q-criterion in Figure 5.22. The airfoil is in fact fully separated as indicated by the relatively flat surface pressure distribution over the entire suction surface.

As the Reynolds number increases for both angles of attack, the LSB closes and continues to decrease in size consistent with the increasing pressure gradient downstream of the LSB. At 4° angle of attack, separation, transition, and reattachment locations move upstream with increasing Reynolds number as shown in Table 5.3. A more significant difference in separation location is observed between the two lowest Reynolds numbers. For 8° angle of attack, the transition location and reattachment locations move upstream with increasing Reynolds number, whereas the separation location remains near constant near the leading edge as presented in Table 5.4.

For both angles off attack, the lift coefficient increases and the drag coefficient decreases with rising Reynolds number.

Table 5.3: Effects of Reynolds number on LSB properties at α = 4°

Re	Separation x_s/C	Transition x_t/C	Reattachment x_r/C	Max Bubble Height, h_b/C	Mean C_L	Mean C_D
10^4	0.36	-	0.98	0.115	0.36	0.047
$4x10^4$	0.25	0.57	0.77	0.044	0.58	0.028
$6x10^4$	0.23	0.55	0.65	0.030	0.59	0.021

Table 5.4: Effects of Reynolds number on LSB properties at α = 8°

Re	Separation x_s/C	Transition x_t/C	Reattachment x_r/C	Max Bubble Height, h_b/C	Mean C_L	Mean C_D
10^4	0.09	-	0.98	0.217	0.65	0.082
$3x10^4$	0.05	0.25	0.53	0.073	0.89	0.070
$6x10^4$	0.04	0.18	0.28	0.027	0.92	0.043
$9x10^4$	0.04	0.14	0.20	0.014	0.94	0.035

Instantaneous three-dimensional vortical structures are visualized with an iso-surface of the Q-criterion in Figures 5.21 and 5.22 for 4° and 8° angles of attack respectively. Even though it is not as clear for 4° angle of attack, the instantaneous turbulent flow structures appear to decrease in size with increasing Reynolds number. At the lowest Reynolds number (10^4), the shear layer does not transition over the airfoil at either angle of attack. Rather, the shear layer rolls up into large coherent structures which exhibit only mild spanwise instabilities. For the lower 4° angle of attack, the time-mean solution resulting from these coherent spanwise vortices can actually be computed with two-dimensional simulation as shown in Figure 5.23. However, two-dimensional calculation for the higher 8° angle of attack, shown in the same figure, does not capture the breakdown of the vortex near the trailing edge of the airfoil resulting in a shorter time-mean separation bubble. These trends for the two angles of attack are also observable in the time-

mean surface pressures coefficients shown in Figure 5.24. For the 4° angle of attack, the surface pressures are in agreement between the two-dimensional and three-dimensional calculations. However, for the 8° angle of attack, the two-dimensional calculation predicts a higher suction peak along with a higher pressure gradient near the trailing edge in comparison with the three-dimensional calculation.

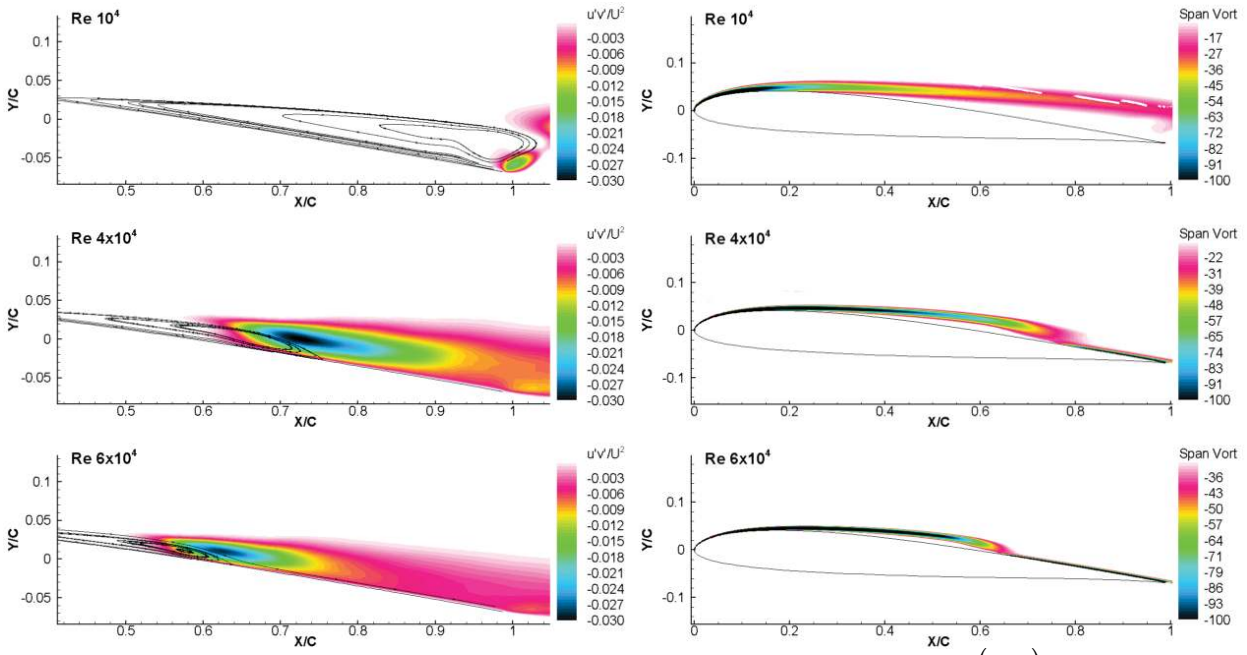

Figure 5.17: Effect of Reynolds number on Reynolds stress $\left(\overline{u'v'}\right)$ and spanwise vorticity at α = 4°

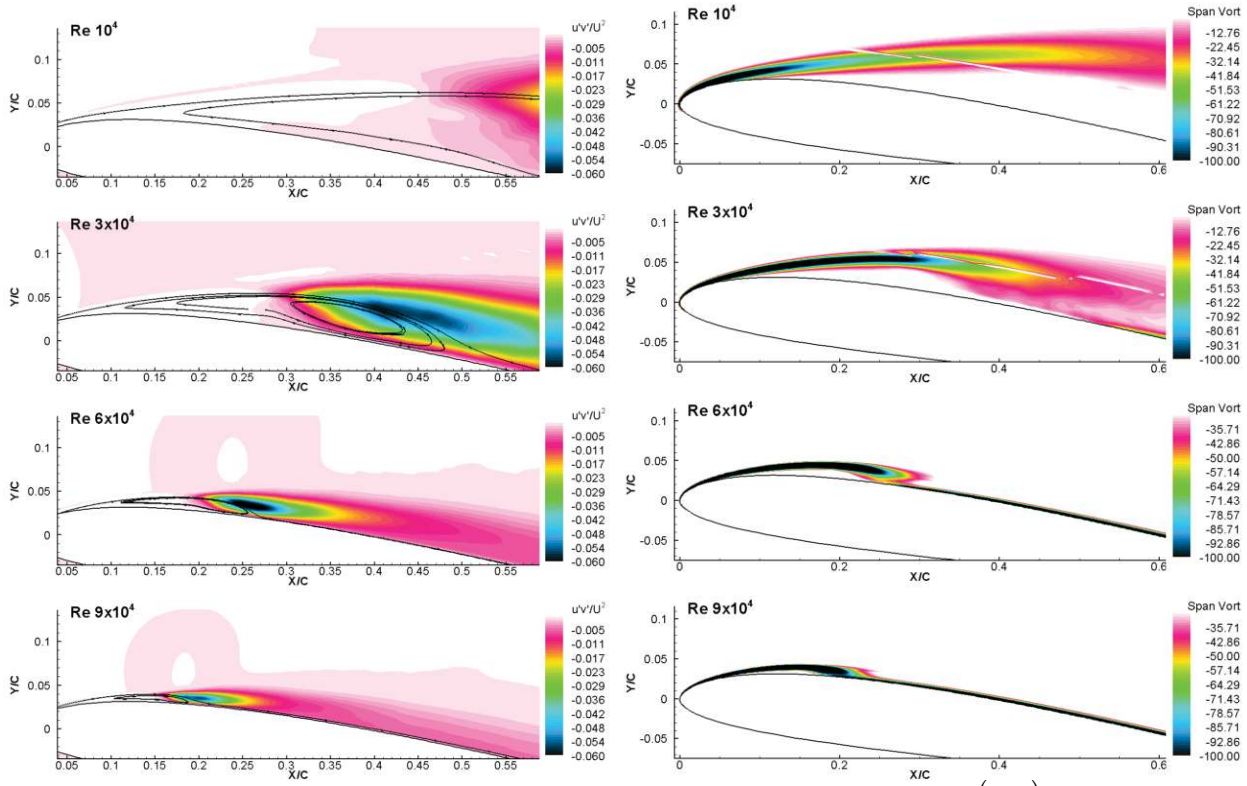

Figure 5.18: Effect of Reynolds number on Reynolds stress $\left(\overline{u'v'}\right)$ and spanwise vorticity at α = 8°

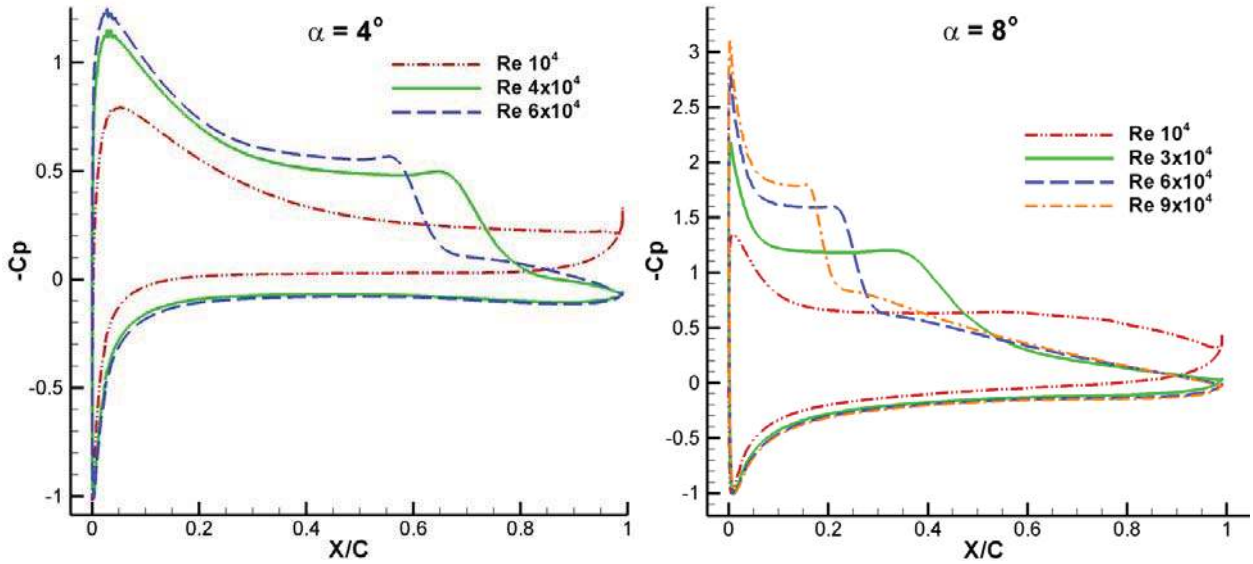

Figure 5.19: Effect of Reynolds number on mean surface *Cp* for α = 4° and α = 8°

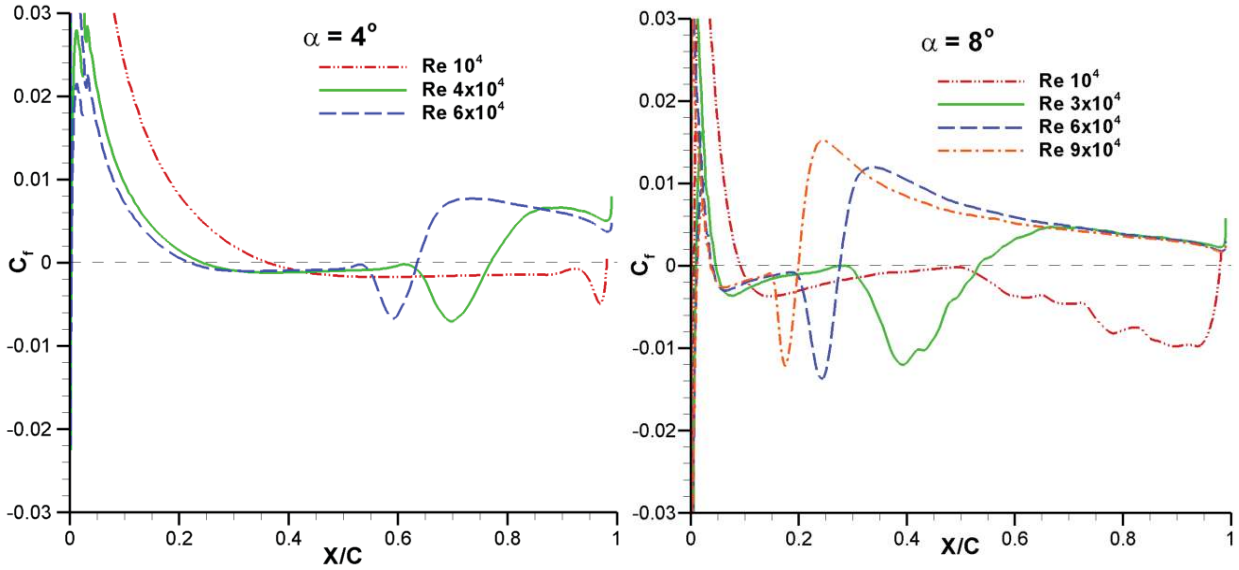

Figure 5.20: Effect of Reynolds number on mean suction surface C_f for α = 4° and α = 8°

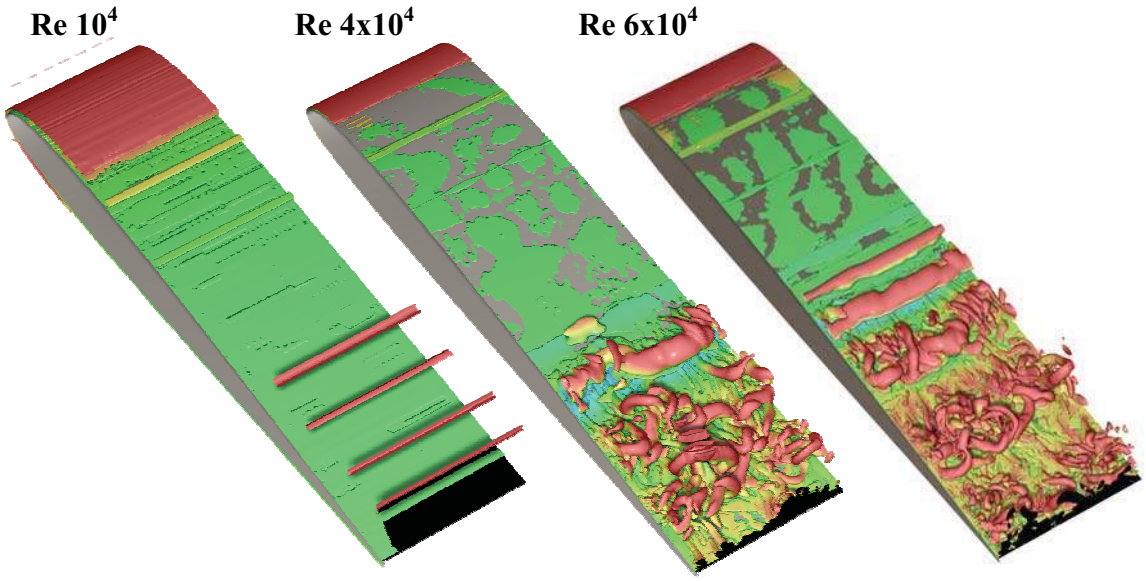

Figure 5.21: Effect of Reynolds number on 3-D instantaneous iso-surfaces of Q-criterion (Q = 500, α = 4°)

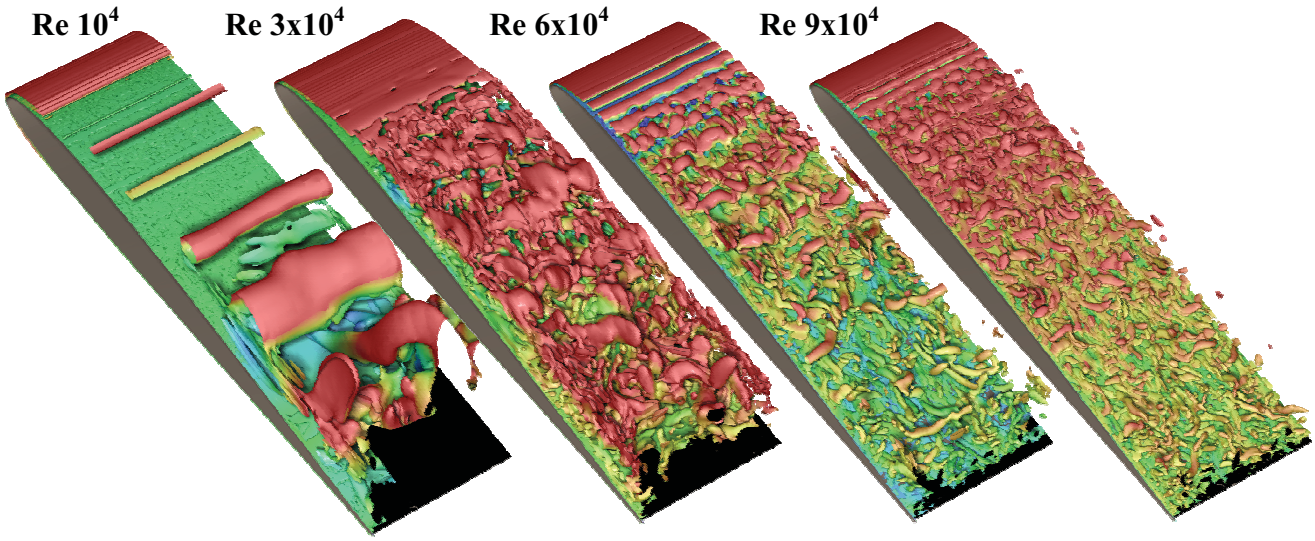

Figure 5.22: Effect of Reynolds number on 3-D instantaneous iso-surfaces of Q-criterion (Q = 500, α = 8°)

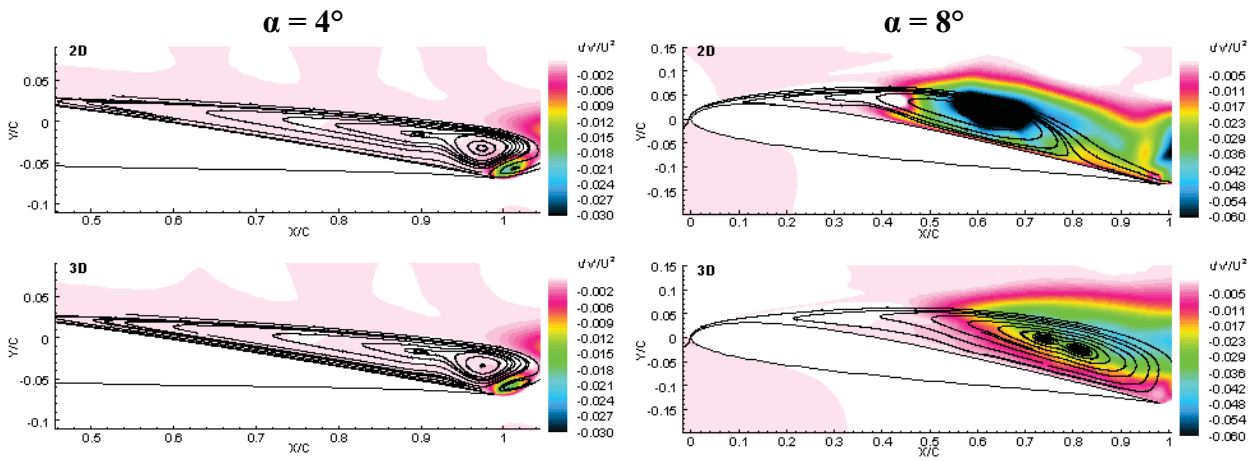

Figure 5.23: Effect of spatial dimensionality on Reynolds stress for Reynolds number 10^4

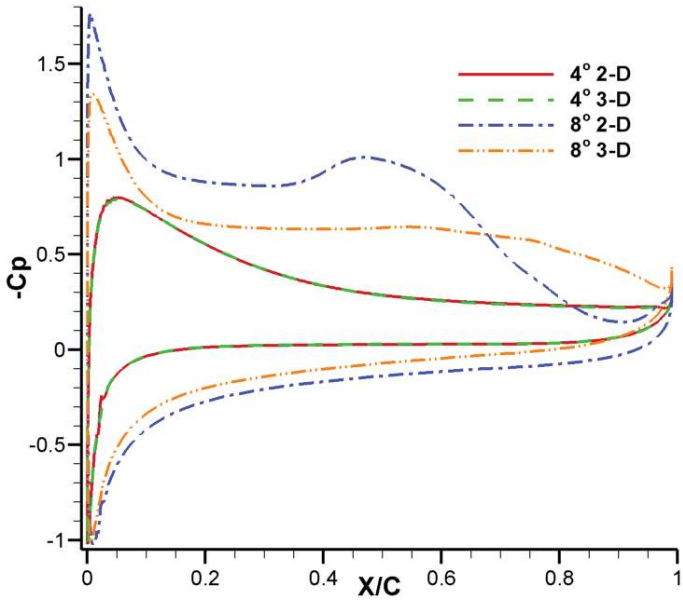

Figure 5.24: Effect of spatial dimensionality on surface pressure for Reynolds number 10^4

5.4 Effect of Leading Edge Disturbance

A limited study was conducted to investigate the sensitivity of the separation bubble to disturbances. The goal was not to investigate any particular flow control technique, rather the effect of perturbations to the shear layer. For simplicity, the disturbance selected was a wall normal zero-net mass-flow blowing/suction slot with a streamwise sinusoidal distribution. The slot was positioned near the leading edge and the amplitude was oscillated sinusoidally in time. The mathematical expression for the disturbance is

$$D(s,t) = A\sin\left(2\pi\frac{s}{s_{\max}}\right)\sin\left(2\pi F^{+}t\right), \quad 0 \le s \le s_{\max}, \quad s_{max}/\mathrm{C} = 0.03 \tag{5.1}$$

where s denotes the body fitted coordinate along the surface of the airfoil and A is the maximum amplitude of the slot. The streamwise extent of the disturbance was chosen such that it was resolved with 20 points. Also, the disturbance is effectively two-dimensional as it is uniform across the span of the computational domain. A magnified illustration of the disturbance is given in Figure 5.25.

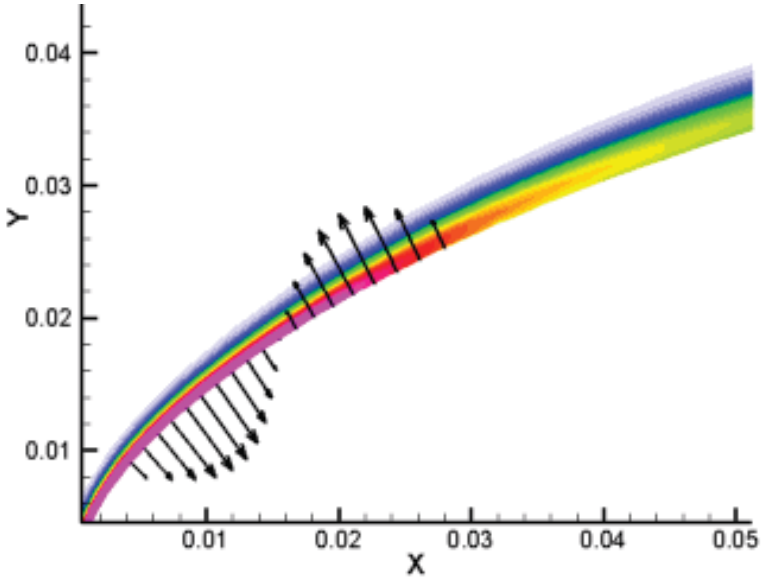

Figure 5.25: Leading edge disturbance with magnified velocity amplitude

Two velocity amplitudes were considered: $A = 0.001$ and $A = 0.01$, which correspond to 0.1% and 1% of the freestream velocity respectively. Both of these amplitudes are too small to affect the time-mean flow in the vicinity of the disturbance. Preliminary investigations into the frequency spectrum indicated a dominant frequency around $F^+ = 6$; this frequency was used for both velocity disturbances.

It is apparent from the contours of the Reynolds stress and spanwise vorticity component in Figure 5.26 that both disturbance velocity amplitudes diminish the separation bubble. Contours of the Reynolds stress has been significantly altered by both leading edge disturbances. Both magnitude and extent normal to the surface of the airfoil have been drastically diminished by the disturbances. Furthermore, the recirculation region, although present, has been nearly eliminated. For both amplitudes, the separation location has moved downstream while the transition and reattachment locations have move upstream as shown in Table 5.5. Neither disturbance has much effect on lift coefficient as shown in Table 5.5. However, both disturbances reduce the drag, with the highest disturbance nearly halving the drag.

Table 5.5: Effect of leading edge disturbance on LSB properties ($\alpha = 4°$, $Re = 6x10^4$)

A ($F^+ = 6$)	Separation x_s/C	Transition x_t/C	Reattachment x_r/C	Max Bubble Height, h_b/C	Mean C_L	Mean C_D
0	0.23	0.55	0.65	0.030	0.59	0.021
0.001	0.25	-	0.52	0.024	0.60	0.018
0.01	0.29	-	0.43	0.019	0.60	0.011

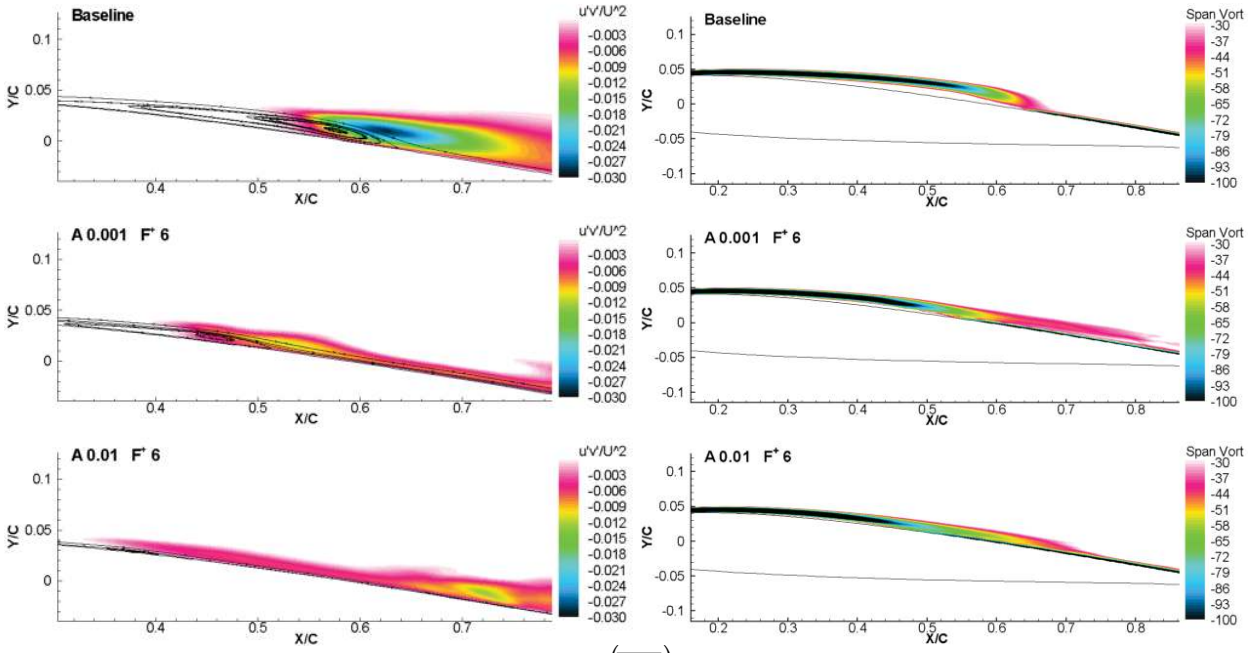

Figure 5.26: Reynolds stress $\left(\overline{u'v'}\right)$ and spanwise vorticity with leading edge disturbance (α = 4°, Re = 6x10^4)

Time-mean velocity profiles from the suction surface of the airfoil are shown in Figure 5.27. Despite the placement of the disturbance about X/C = 0.02, the laminar velocity profiles upstream of X/C = 0.2 are unaltered. This demonstrates that neither disturbance amplitude is large enough to affect the time-mean solution near the disturbance. However, the disturbance does cause the profiles to retain a fuller velocity profile through the undisturbed separated region, consistent with the reduction in the separation bubble. The higher disturbance velocity amplitude yields the fullest profile. Furthermore, both the flat plateau in the surface pressure coefficient and the drop in skin friction coefficient diminish with increasing disturbance velocity amplitude as depicted in Figures 5.28 and 5.29. Besides the drop in the pressure peak, the disturbance with higher velocity magnitude produces a pressure field that closely follows that predicted by inviscid theory.

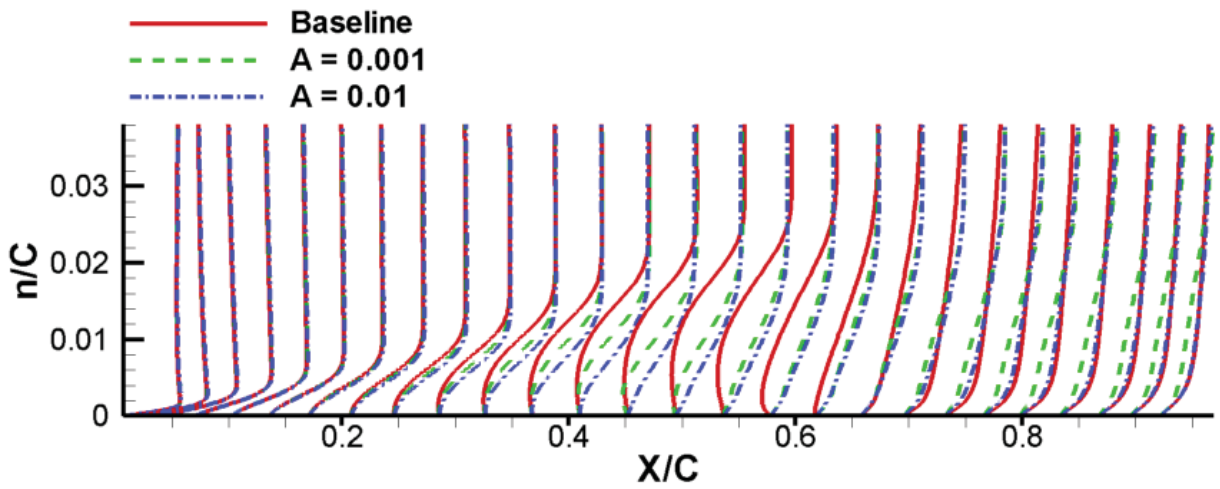

Figure 5.27: Boundary layer profiles with leading edge disturbance at α = 4°, Re = 6x10^4 (scaled by 0.05)

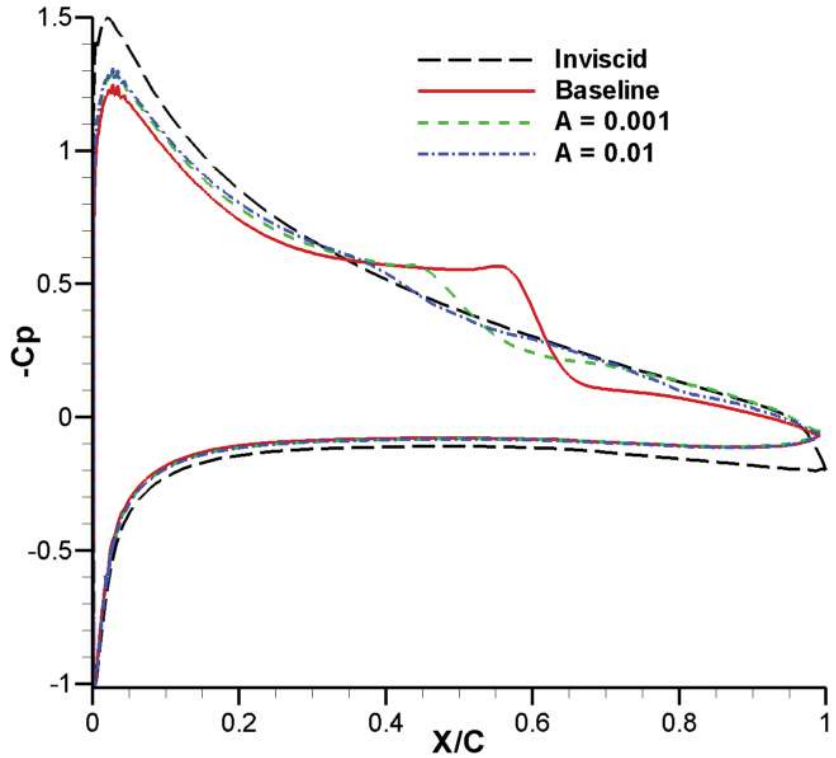

Figure 5.28: Effect of leading edge disturbance on mean surface *Cp*

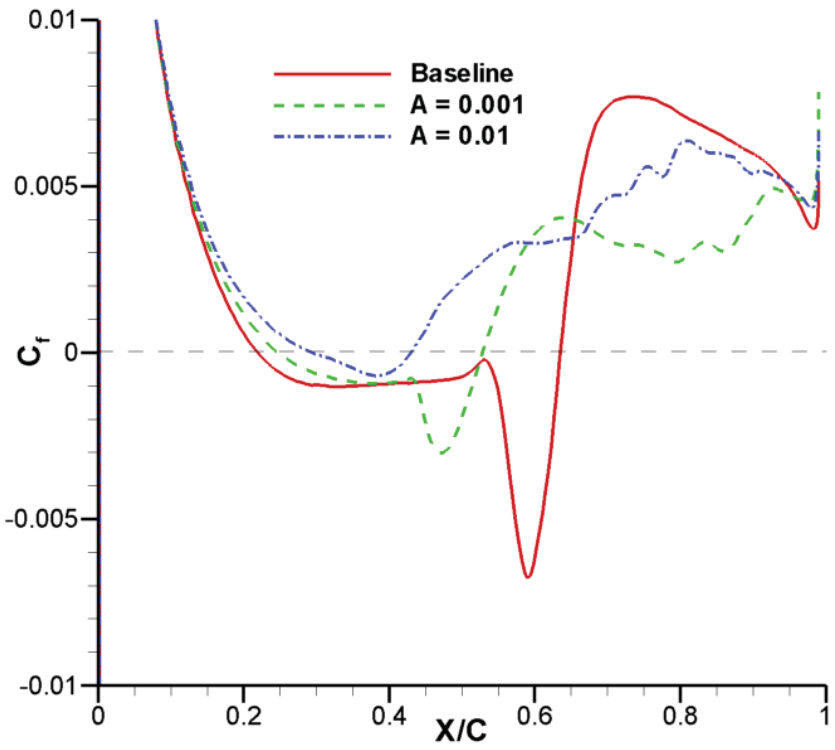

Figure 5.29: Effect of the leading edge disturbance on mean suction surface C_f

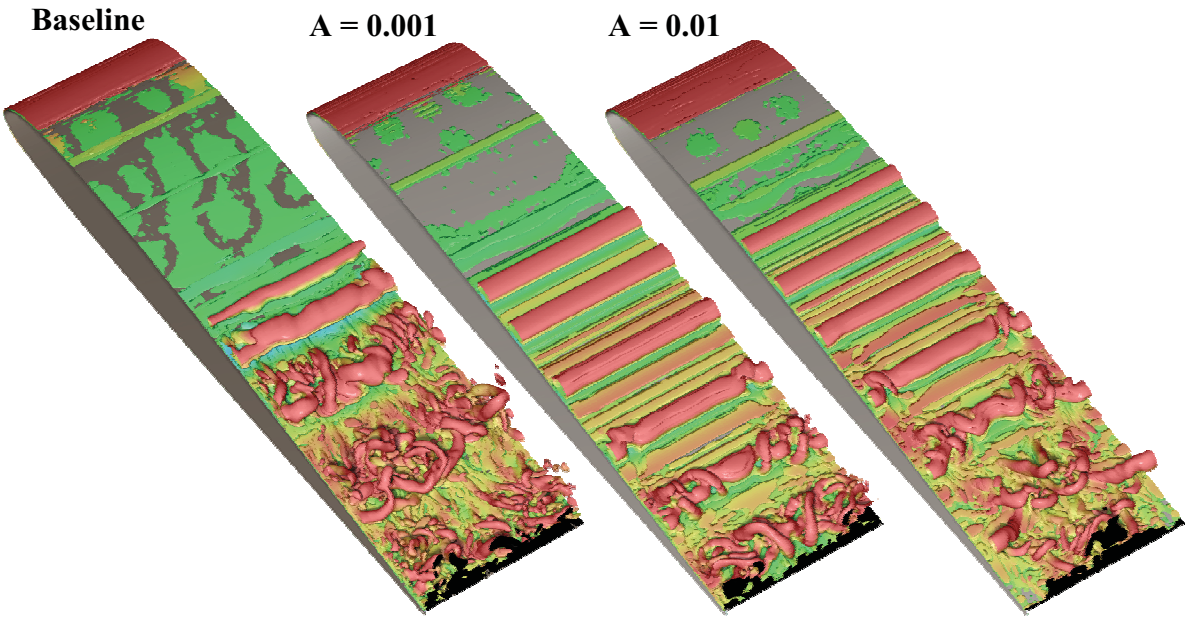

Figure 5.30: Effect of leading edge disturbance on 3-D instantaneous iso-surfaces of Q-criterion (Q = 500, α = 4°)

Instantaneous flow features are inspected to explain the affect of the leading edge disturbance on the time-mean flow. Similar to the baseline calculation, with the leading edge disturbance present the shear layer rolls up into a spanwise vortex as shown by the instantaneous flow features visualized by the iso-surface of Q-criterion in Figure 5.30. However, rather than rapidly breaking down into finer turbulent structures, the leading edge disturbance causes the vortex to remain coherent over a significant portion over the airfoil before breaking down. Unfortunately, the periodic boundary condition appears to have an affect on the solution as the spanwise vortices first begin breakdown at the spanwise boundaries of the computational domain. It is possible that a larger spanwise extent is required to eliminate grid affects on the solution with the leading edge disturbance present.

Instantaneous surface pressure coefficient and contours of spanwise vorticity component for the two disturbance magnitudes are shown in Figures 5.31 through 5.34. Instantaneous surface pressures begin to deviate from the time-mean surface pressure at approximately $X/C = 0.4$ and $X/C = 0.35$ for the lower and higher disturbance amplitudes respectively. Similarly, instantaneous spanwise vorticity contours indicate the shear layer rolling up at approximately at the same streamwise locations. Furthermore, a periodic shedding of the vortices has been established as the surface pressures at the particular instances in time nearly coincide. In addition, the instantaneous spanwise vorticity component contours appear nearly identical for the selected time instances.

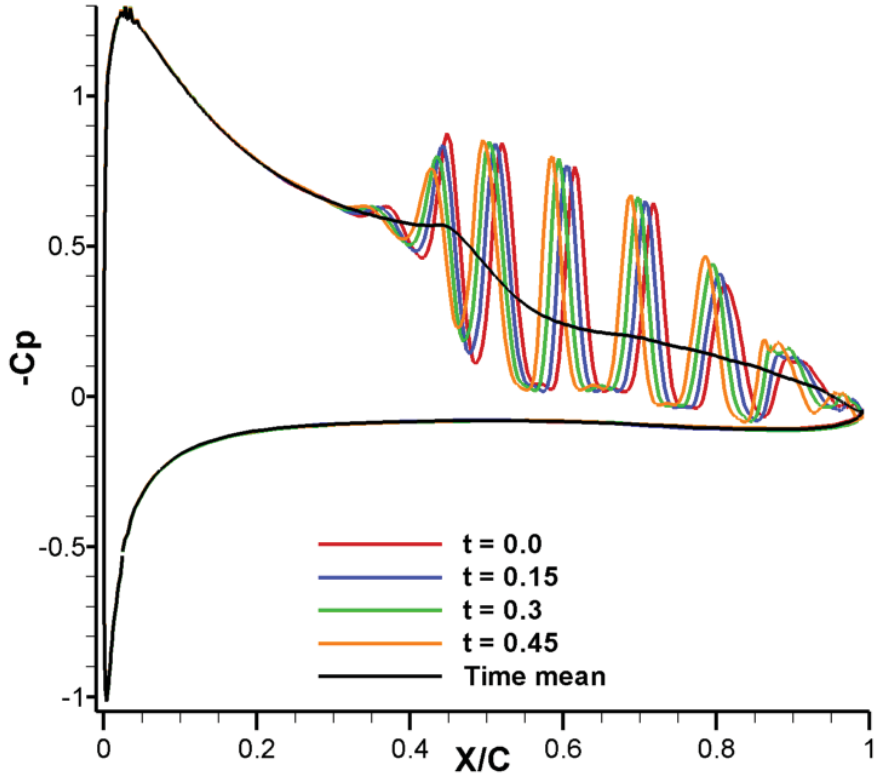

Figure 5.31: Instantaneous surface *Cp* ($\alpha = 4°$, $Re = 6x10^4$, A = 0.001)

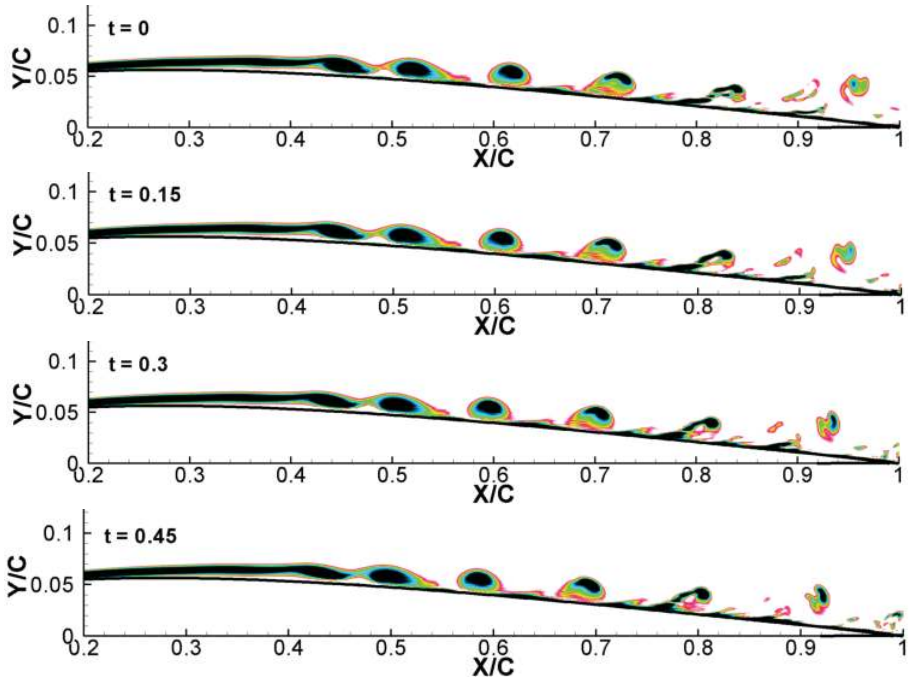

Figure 5.32: Instantanous contours of spanwise vorticity component ($\alpha = 4°$, $Re = 6x10^4$, A = 0.001)

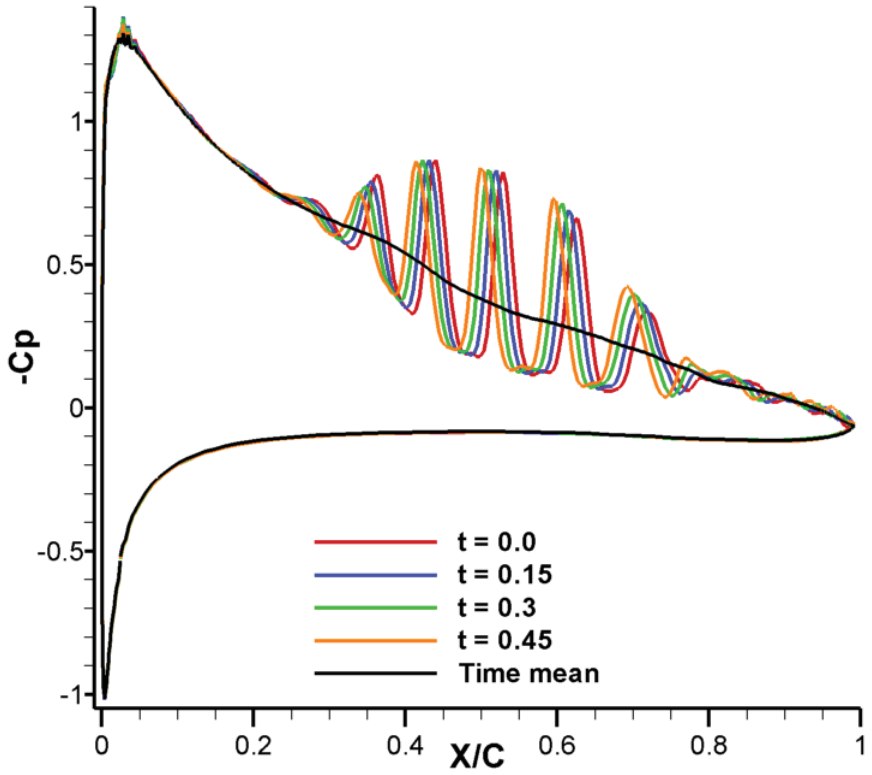

Figure 5.33: Instantaneous surface *Cp* ($\alpha = 4°$, $Re = 6x10^4$, A = 0.01)

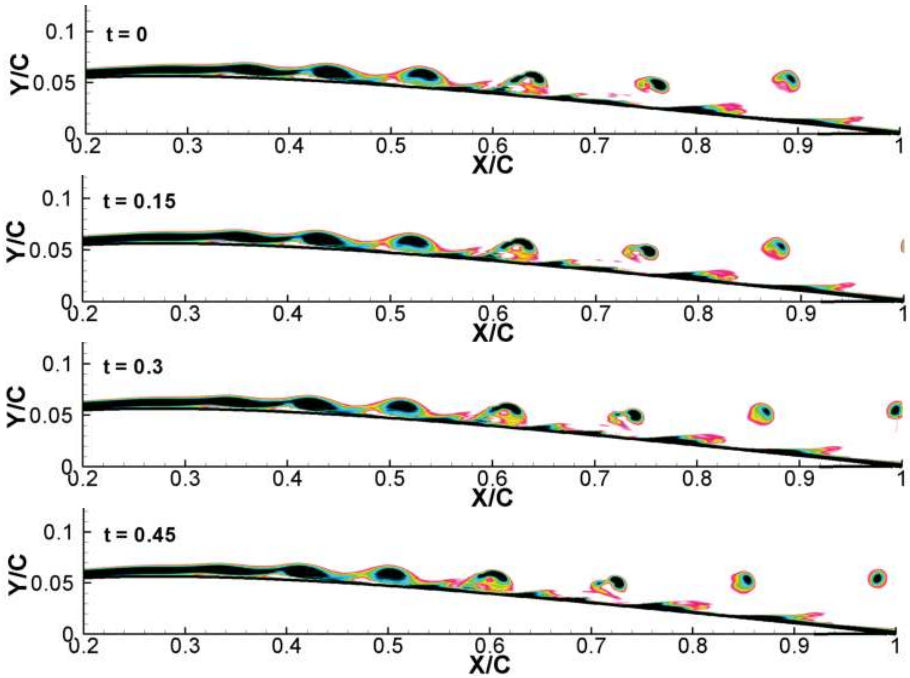

Figure 5.34: Instantanous contours of spanwise vorticity component ($\alpha = 4°$, $Re = 6x10^4$, A = 0.01)

Streamwise velocity spectra for the two disturbances obtained using the probes described in section 5.1 are depicted in Figures 5.35 and 5.36. Note that the axes differ in range for these figures to emphasize the dominant frequencies at each streamwise location. As expected, the forcing frequency of $F^+ = 6$ is dominant for both disturbance amplitudes and at all three streamwise locations. Furthermore, additional harmonics have formed by the physics of the fluid.

Comparing the two disturbance amplitudes at $X/C = 0.1$, there is an order of magnitude greater energy transferred into the first mode for the higher amplitude disturbance along with a noticeable transfer of energy into the second mode. However, moving downstream to the half chord, the energy content in the dominant mode has grown significantly and is now similar between the two disturbance amplitudes. Near the trailing edge, the dominant mode for the lower amplitude disturbance has retained a greater amount of energy. Thus, it is evident that the higher amplitude disturbance transfers energy to the higher modes at a greater rate which causes the coherent spanwise vortex to breakdown after traveling a shorter distance consistent with observations in the instantaneous solution. The streamwise velocity energy spectra from the baseline and two disturbance amplitudes at $X/C = 0.95$ are shown with log-log plots in Figure 5.37. While all three spectra resemble that of turbulent decay, the leading disturbance has shifted energy content into lower frequencies.

Evidently, unlike traditional passive methods where the LSB is removed by tripping the flow to turbulent upstream of the separation location, the leading edge disturbance has nearly eliminated the LSB by exiting the two-dimensional mode and reduced spanwise instabilities of the shear layer.

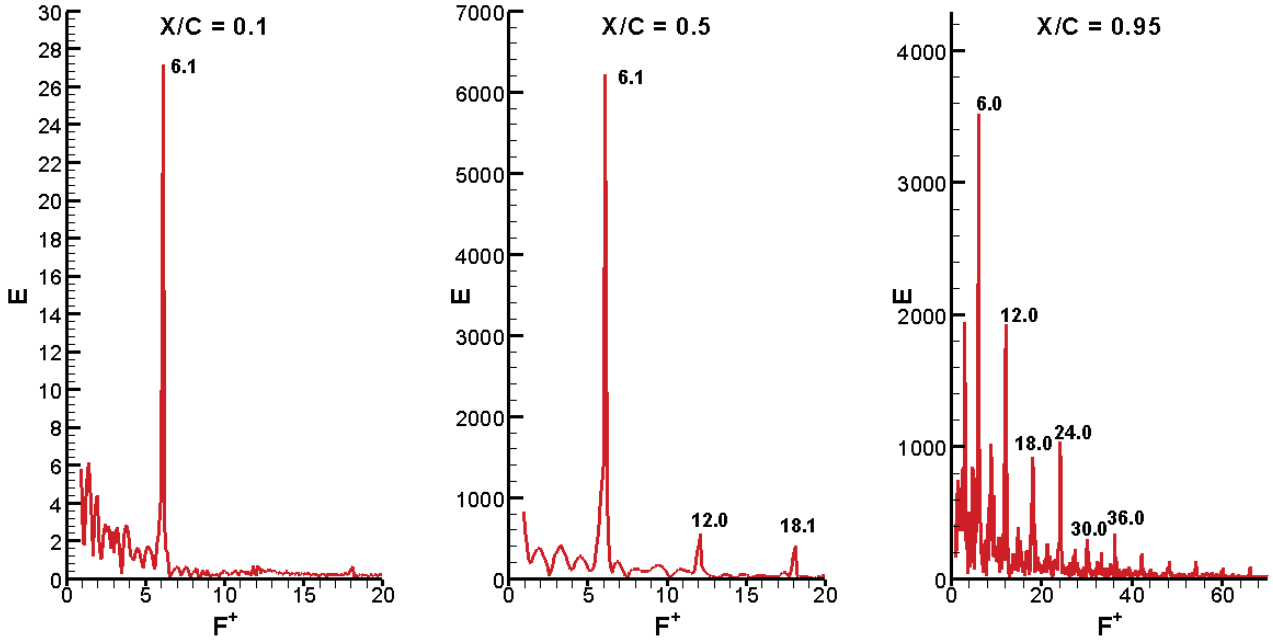

Figure 5.35: Streamwise velocity component energy spectra (α = 4°, Re = 6x10^4, A = 0.001)

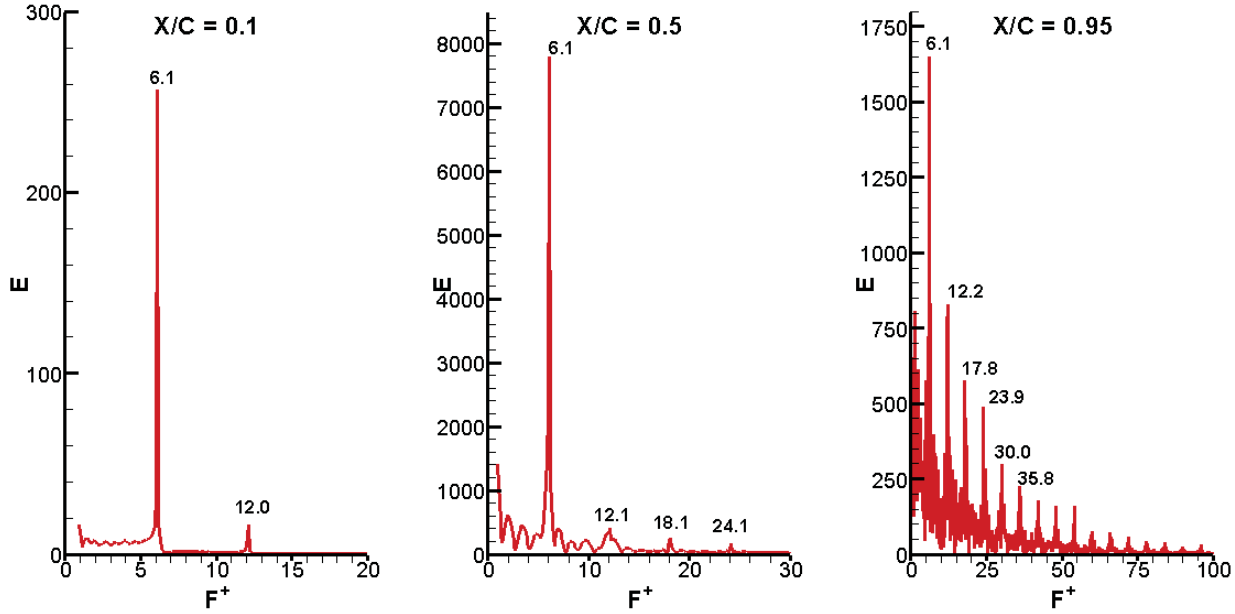

Figure 5.36: Streamwise velocity component energy spectra (α = 4°, Re = 6x10^4, A = 0.01)

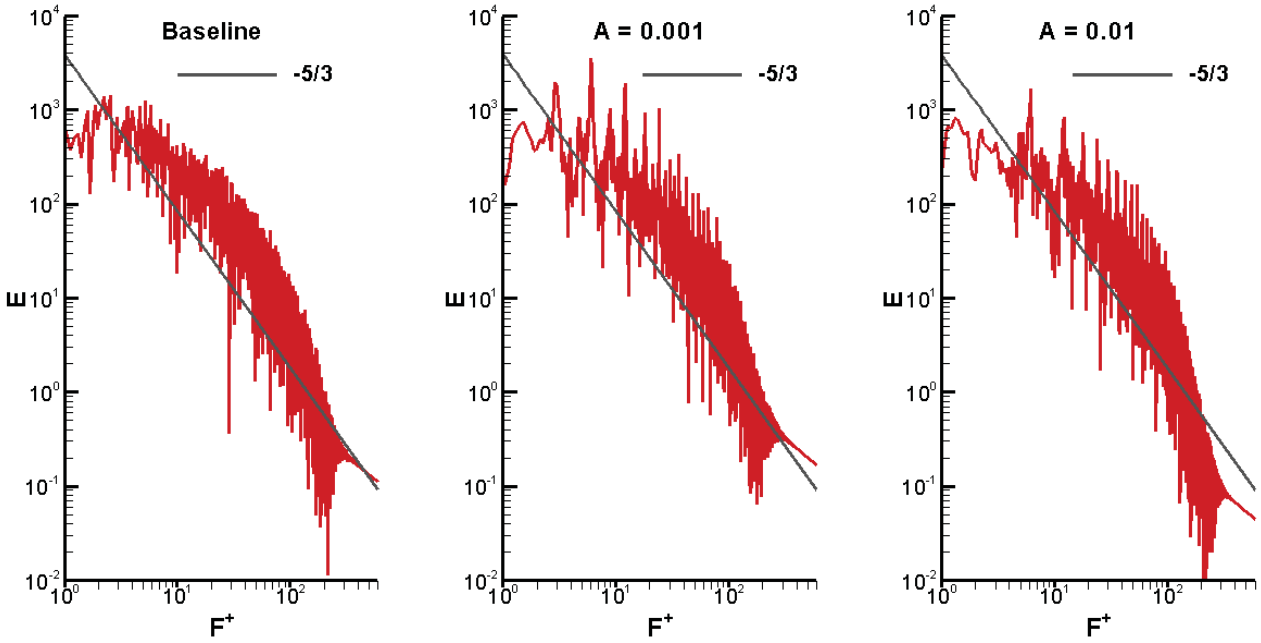

Figure 5.37: Streamwise velocity component energy spectra ($\alpha = 4°$, $Re = 6x10^4$, X/C = 0.95)

6 Conclusions and Recommendations

6.1 Conclusions

An implicit large eddy simulation (ILES) technique has been applied to predict the formation and burst of a time-mean laminar separation bubble (LSB) on the SD7003 airfoil. The LSB is characterized by laminar, transitional, and turbulent flow regions. Flow solutions were obtained with a validated Navier-Stokes solver based on high-order compact schemes. The solution was regularized with a low pass Pade-filter which removed poorly resolved high wave numbers in the mesh in lieu of an explicit SGS model. Unlike RANS solvers coupled with transition models, which rely on a limited number of parameters to determine transition locations, the ILES method solves the unfiltered Navier-Stokes equations without change in the laminar, transitional, and turbulent regions of the flow. Furthermore, the ILES method captured the shift from a closed LSB to bubble burst and stall without modification of any parameters.

Computations compared favorably with experimentally measured Reynolds stresses for available angles of attack, 4°, 8°, and 11°, at Reynolds number $6x10^4$. Computed separation, transition, and reattachment locations were also in agreement with measured values. The transitional nature of the flow was indicated by streamwise velocity component energy spectra, and a fuller turbulent velocity profile was observed downstream of the reattachment location. The computed time-mean lift polar (2°-14°) agreed well with experimental measurements. Most notably, both the stall angle of attack and post stall lift coefficient were accurately predicted. Even though the time-mean drag coefficients were over predicted, they also compare favorably with measured values. As expected, with increasing angle of attack, the ILES simulations predict the LSB decreasing in size and moving toward the leading edge until post stall where the bubble bursts and the flow is fully separated. Accurate resolution of massively separated flows is imperative for research focused on modeling maneuvers that may promote dynamic stall phenomena.

Effects of Reynolds number was considered for 4° and 8° angle of attack. For the lowest Reynolds number (10^4), the time-mean flow field is characterized by a large recirculation region. Furthermore, the shear layer does not transition into turbulence. At the higher Reynolds numbers of $3x10^4$ and $4x10^4$ an LSB has formed. As the Reynolds number increases, the LSB decreases in vertical and streamwise extent and moves towards the leading edge of the airfoil. In addition, the pressure gradient increases as a result of a more intense transition process indicated by the increase in Reynolds stress and decrease in size of instantaneous turbulent flow structures with increased Reynolds number. Time-mean lift increases while time-mean drag decreases consistent with the diminishing extent of the LSB with increasing Reynolds number.

A leading edge disturbance was introduced to perturb the shear layer. The disturbance was implemented in the form of a zero-net-mass-flow jet. Two velocity amplitudes of the jet were considered, neither of which were strong enough to influence the time-mean flow field in direct vicinity of the jet. The jet was forced at a frequency near the natural frequency of the shear layer. Both disturbance amplitudes were able to practically eliminate the time-mean LSB. However, unlike traditional passive control methods, the leading edge disturbance did not induce turbulent transition to eliminate the LSB; rather it excited two-dimensional mode and reduced spanwise instabilities which in turn caused the shear layer to roll up into more stable and coherent vortices that traversed a significant streamwise portion of the airfoil before breaking down. As such, the LSB was eliminated by delaying the turbulent transition process.

6.2 Recommendations

The ILES method has been demonstrated to capture the complex laminar-transitional-turbulent low Reynolds number flow associated with a LSB. The primary influence on the quality of the solution is grid resolution. Furthermore, because the unfiltered Navier-Stokes equations are solved directly, the method is dependent on three-dimensional computational domains to capture the vortex stretching and spanwise instabilities of the shear layer associated with turbulent transition process. However, ILES methods are mostly suitable for low Reynolds numbers that exhibit large LSBs. With increasing Reynolds numbers, the transitional and turbulent vortical structures decrease in size and hence require increasing grid resolution to capture the fine scale structures. In addition, due to the higher computational cost of three-dimensional calculations, the method of coupling well calibrated turbulence and transition models, such as the RANS-e^N method[22, 23, 24], are more suitable for studies requiring a large

number of airfoil calculations at pre-stall angles of attack. The massively separated flows associated with post-stall angles of attach are still challenging for RANS solvers to capture.[23]

Given the ability of the ILES method to capture the massively separated flow associated with post-stall flow fields, it is recommended that the method be applied to maneuvering airfoils where high angle of attack excursions could induce leading-edge dynamic stall. Similar to massively separated post-stall flow, turbulence modeling techniques are limited in their ability to capture the breakdown and transition of vortices shed from the leading edge of a plunging airfoil.[22] Such calculations would however require a significant increase in grid resolution on both sides of the airfoil. In particular, instantaneous vortical structures were observed to propagate into the coarser mesh away from the airfoil surface in presented high incidence angle calculations. Adequate resolution of these structures is likely required in a maneuvering airfoil calculation. None the less, it is hoped that maneuvering airfoil ILES calculations could provide further insight to improve the ability of turbulence models to capture the vortex breakdown.

A few improvements are suggested for FDL3DI flow solver to extend the ILES technique to full three-dimensional calculations of MAV's. A boundary condition or model that imposes freestream turbulence on the solution is lacking. Freestream turbulence can cause the separated shear layer of the LSB to transition more rapidly, which shifts the transition and reattachment locations upstream. [23] Furthermore, particularly for dynamic motions, the solver lacks a routing for obtaining integrated lift, drag, and momentum coefficients on Chimer overset meshes. The integration first required the solution to be transferred to a single mesh during the post-processing stage. While this is feasible for time-mean solutions, it is not feasible for simulations that intend incorporate maneuvers requiring a time history of integrated quantities.

Bibliography

1 Schmitz, F.W., *Aerodynamik des Fluges,* Verlag Carl Lange, Duisburg, 1960.

2 Eppler, R., *Airfoil Design and Data*, Springer Verlag, ISBN 3-540-52505-X, 1990.

3 Selig, M.S., Donovan, J. F., Fraser, D. B., *Airfoils at Low Speeds*, SoartechTech Publications. H.A. Stokely, Virginia Beach, VA, USA, 1989.

4 Jones, B. M., ”Stalling,” *Journal of the Royal Aeronautical Society*, Vol. 38, pp. 753-770, 1934.

5 Maekawa, T. and Atsumi, S., “Transition Caused by Laminar Flow Separation,” NACA-TM-1352, 1952.

6 Berry, D. T., ”A Visual Investigation of Laminar Separation and Turbulent Rejoin of the boundary Layer as Affected by Angle of Attack,” M. S. Thesis, University of Notre Dame, Notre Dame, Ind., 1955

7 Gault, D. E., ”An Experimental Investigation of Regions of Separated Laminar Flow,” NACA-TN-3505, Sep. 1955.

8 Crabtree, L. F., ”Effects of Leading Edge Separation on Thin Wings in Two Dimensional Incompressible Flow,” *Journal of Aeronautical Sciences*, Vol. 24, Aug. 1957.

9 Ward, J. R., ”The Behavior and Effects pf Laminar Separation Bubbles on Airfoils in Incompressible Flow,” *Journal of the Royal Aeronautical Society*, Vol. 67, pp. 783-790, Dec. 1963.

10 Gaster, M., “The Structure and Behavior of Laminar Separation Bubbles, “ ARC R&M No. 3595, 1967.

11 Roberts, W. B., ”A Study of the Effect of Reynolds Number and Laminar Separation Bubbles on the Flow through Axial Compressor Cascades,” D. Sc. Dissertation, von Karman Institute, 1973.

12 Horton, H. P., "Laminar Separation Bubbles in Two and Three Dimensional Incompressible Flow," Ph.D. Thesis, University of London, London, 1968.

13 Schmidt, G. S., and Mueller, T. J., “A Study of the Laminar Separation Bubble on an Airfoil at Low Reynolds Numbers Using Flow Visualization Techniques,” AIAA Paper 87-0242, Jan. 1987.

14 Hodge, J. K., Stone, A. L., and Miller, T. E., “Numerical Solution for Airfoils near Stall in Optimized Boundary-Fitted Curvilinear Coordinates,” *AIAA Journal*, Vol. 17, No. 5, 1979, pp. 458-464.

15 Jacobs, E. N., and Sherman, A., “Airfoil Characteristics as Affected by Variations of the Reynolds Number,” NACA Rept. 596, 1937.

16 Von Doenhoff, A. E., ”A Preliminary Investigation of Boundary-Layer Transition Along a Flat Plate with Adverse Pressure Gradient,” NACA-TN-639, Mar. 1938.

17 Smith, A. M. O., Gamberoni, N., ”Transition, Pressure Gradient and Stability Theory,” Douglas Aircraft Report ES-26388, 1956.

18 Van Ingen, J. L., ”A Suggested Semi-Empirical Method for the Calculation of the Boundary Layer Transition Region,” Inst. of Tech., Dept. of Aeronautics and Engrg., Report VTH-74, Delft, Holland, 1956.

19 Drela, M., XFOIL Users Guide, Version 6.94 , MIT Aero. and Astro. Department, 2002.

20 Hegna, H. A., ”The Numerical Solution of Incompressible Turbulent Flow Over Airfoils,” AIAA Paper 81-0047, Jan. 1981.

21 Green, J., Weeks, D., and Brooman, J., “Prediction of Turbulent Boundary Layers and Wakes in Compressible Flow by a Lag-Entrainment Method,” ARC-R/M-3791, 1977.

22 Radespiel, R., Windte, J., and Scholz, U., “Numerical and Experimental Flow Analysis of Moving Airfoils with Laminar Separation Bubbles,” AIAA Paper 2006-501, Jan. 2006.

23 Lian, Y., and Shyy, W., “Laminar-Turbulent Transition of a Low Reynolds Number Rigid or Flexible Airfoil,” AIAA Paper 06-3051, Jun 2006.

24 Yuan, W., Khalid, M., Windte J., Scholz, U., and Radespiel, R., “An Investigation of Low-Reynolds-number Flows past Airfoils,” AIAA Paper 05-4607, Jun 2005.

25 Arnal, D., Casalis, G., and Juillen, J. C., “A Survey of the Transition Prediction Methods: from Analytical Criteria to PSE and DNS,” in M. Hallback (ed.) *Turbulence and Transition Modeling*, Lecture Notes from the ERCOFTAC/IUTAM Summer School held in Stockholm, June 12-20, 1995, Kluwer Academic Publishers, Dordrecht, pp. 3-14, 1996.

26 Winkelmann, A. E. and Barlow, J. B., "A Flow Field Model for a Rectangular Planform Wing Beyond Stall," AIAA Journal, Vol. 18, No. 8, 1980.

27 Visbal, M. R. and Rizzetta, D. P., “Large-Eddy Simulation on Curvilinear Grids Using Compact Differencing and Filtering Schemes. Journal of Fluids Engineering,” 124:836–847, 2002.

28 Visbal, M. R., Morgan, P. E., and Rizzetta, D. P., “An Implicit LES Approach Based on High-Order Compact Differencing and Filtering Schemes,” AIAA Paper 2003-4098, 2003.

29 Stolz. S., and Adams, N., “An Approximate Deconvolution Procedure for Large-Eddy Simulation,” *Physics of Fluids*, Vol. 11, No. 7, 1999, pp. 1699–1701.

30 Mathew, J., Lechner, R., Foysi, H., Sesterhenn, J., and Friedrich, R., “An explicit filtering method for LES of compressible flows,” *Physics of Fluids*, Vol. 15, No. 8, 2003, pp. 2279–2289.

31 Selig, M. S., Guglielmo, J. J., Broeren, A. P., and Giguere, P., “Summary of Low Speed Airfoil Data,” Vol. 1, Soartech Aero, Virginia Beach, VA, 1995.

32 Ol, M. V., McAuliffe, B. R., Hanff, E. S., Scholz, U., and Kähler, C., “Comparison of Laminar Separation Bubble Measurements on a Low Reynolds Number Airfoil in Three Facilities,” AIAA Paper 2005-5149, Jun. 2005.

33 Selig, M. S., Guglielmo, J. J., Groeren, A. P., G. Giguere, P., “Summery of Low-Speed Airfoil Data,” SoarTech Aero Publications, H. A. Stokely, Virginia Beach, VA, USA, 1995.

34 Selig, M. S., Donovan, J. F., Fraser, D. B., ”Airfoils at Low Speeds,” Soartech 8, Soartech Publications, H. A. Stokely, Virginia Beach, VA, USA, 1989.

35 Rizzetta, D. P., and Visbal M. R., "Numerical Investigation of Transitional Flow Through a Low-Pressure Turbine Cascade," AIAA Paper 2003-3587, Jun. 2003.

36 Gordnier, R.E. and Visbal, M.R., "Numerical Simulation of Delta-Wing Roll," AIAA Paper 93-0554, Jan. 1993.

37 Visbal, M. R., "Computational Study of Vortex Breakdown on a Pitching Delta Wing," AIAA Paper 93-2974, Jul. 1993.

38 Visbal, M. R., Gaitonde, D., and Gogineni, S., "Direct Numerical Simulation of a Forced Transitional Plane Wall Jet," AIAA Paper 98-2643, Jun. 1998.

39 Sherer, S. E, and Visbal, M. R., “Implicit Large Eddy Simulations Using a High-Order Overset Grid Solver,“ AIAA Paper 2004-2530, Jan. 2004.

40 Rizetta, D. P., Visbal, M.R., and Blaisdell, G.A., "A Time-Implicit High Order Compact Differencing and Filtering Scheme for Large-Eddy Simulation," *International Journal for Numerical Methods in Fluids*, Vol. 42, No. 6, Jun. 2003, pp. 665-693.

41 Sherer, S. E., Gordnier, R. E., and Visbal, M. R., ”Computational Study of a UCAV Configuration Using a High-Order Overset-Grid Algorithm,” AIAA Paper 2008-626, Jan. 2008

42 Smagorinsky, J., “General Circulation Experiments with the Primitive Equations. I. The Basic Experiment,” *Mon. Weather Rev.*, Vol. 91, 1963, pp. 99-164.

43 Germano, M., Piomelli, U., Moin, P., and Cabot, W., “A Dynamic Subgrid-Scale Eddy Viscosity Model,” *Physics of Fluids A*, Vol. 3, 1991, pp. 1760.

44 Spyropoulos, E. T., and Blaisdell, G. A., “Evaluation of the Dynamic Model for Simulations of Compressible Decaying Isotropic Turbulence,” AIAA Journal, Vol 34, No. 5, pp. 990-998, 1996.

45 Hughes, T. J., Mazzei, L., and Jansen, K., “Large Eddy Simulation and the Variational Miltiscale Method,” Comput. Visual. Sci., Vol 3, pp. 47-59.

46 Beam, R. and Warming, R., "An Implicit Factored Scheme for the Compressible Navier-Stokes Equations," *AIAA Journal*, Vol. 16, No. 4, Apr. 1978, pp. 393-402.

47 Jameson, A., Schmidt, W., and Turkel, E., “Numerical Solutions of the Euler Equations by Finite Volume Methods Using Runge–Kutta Time Stepping Schemes,” AIAA Paper 81-1259, June 1981.

48 Pulliam, T.H. and Chaussee, D.S., "A Diagonal Form of an Implicit Approximate-Factorization Algorithm," *Journal of Computational Physics*, Vol. 39, No. 2, Feb. 1981, pp. 347-363.

49 Visbal,M. R., and Gaitonde, D. V., “High-Order-Accurate Methods for Complex Unsteady Subsonic Flows,” *AIAA Journal*, Vol. 37, No. 10, 1999, pp. 1231–1239.

50 Lele, S. A., “Compact Finite Difference Schemes with Spectral-Like Resolution,” *Journal of Computational Physics*, Vol. 103, No. 1, 1992, pp. 16–42.

51 Gaitonde, D. V. and Visbal, M. R., "High-Order Schemes for Navier-Stokes Equations: Algorithm and Implementation into FDL3DI," Air Force Research Laboratory AFRL-VA-WP-TR-1998-3060, Wright-Patterson Air Force Base, Ohio, 1998.

52 Adam, Y., "Highly Accurate Compact Implicit Methods and Boundary Conditions," *Journal of Computational Physics*, Vol. 24, 1977, pp. 10-22.

53 Koutsavdis, E. K., Blaisdell, G. A., and Lyrintzis, A. S., "On the Use of Compact Schemes with Spatial Filtering in Computational Aeroacoustics," AIAA Paper 99-0360, Jan. 1999.

54 Jurgens, H. M., and Zingg, D. W., "Implementation of a High-Accurate Finite-Difference Scheme for Linear Wave Phenomena," *Proceedings of the Internat. Conf. on Spectral and High-Order Methods*, June 1995.

55 Gaitonde, D., Shang, J. S., andYoung, J. L., "Practical Aspects of High-Order Accurate Finite-Volume Schemes for Electromagnetics,"AIAA Paper 97-0363, Jan. 1997.

56 Vichnevetsky. R., "Numerical Filtering for Partial Differential Equations," *Numerical Applications Memorandum*, (NAM 156), November 1974.

57 Visbal, M. R., and Gaitonde, D. V., "High-Order Accurate Methods for Unsteady Vortical Flows on Curvilinear Meshes," AIAA Paper 98-131, 1998

58 Steger, J. L., "Implicit Finite-Difference Simulations of Flow about Arbitrary Two-Dimensional Geometries," *AIAA Journal*, Vol. 16, No. 7, pp 679-686, 1978

59 Vinokur, M., "An Analysis of Finite-Difference and Finite-Volume Formulations of Conservation Laws," *Journal of Computational Physics*, Vol. 81, pp. 1, 1989.

60 Pulliam, T. H., and Steger J. L., "Implicit Finite-Difference Simulations of Three-Dimensional Compressible Flow," *AIAA Journal*, Vol. 18, No. 2, pp. 159-167, 1980.

61 Thomas, P. D., and Lombard, C. K., "Geometric conservation law and its application to flow computations on moving grids," *AIAA Journal*, Vol. 17, No. 10, pp 1030-1037, 1979.

62 Visbal, R. D., and Gaitonde, D. V., "On the Use of Higher-Order Finite Difference Schemes on Curvilinear and Deforming Meshes," *Journal of Computational Physics*, Vol. 181, pp 155-185, 2002

63 Message Passing Interface Forum, "MPI: A Message-Passing Interface Standard," Computer Science Department Technical Report CS-94-230, University of Tennessee, Knoxville, TN, Apr. 1994.

64 Sherer, S. E., Visbal, M. R., and Galbraith, M. C., "Automated Preprocessing Tools for Use with a High-Order Overset-Grid Algorithm," AIAA Paper 06-1147, Jan 2006.

65 Benek, J. A., Steger, J. L., and Dougherty, F. C., "A Flexible Grid Embedding Technique with Application to the Euler Equations," AIAA Paper 83-1944, 1983.

66 Sherer, S. E., "Investigation of High-Order and Optimized Interpolation Methods with Implementation in a High-Order Overset Fluid Dynamics Solver," Ph.D. Dissertation, Aeronautical and Astronautical Engineering Dept., Ohio State Univ., Columbus, OH, 2002.

67 Steinbrenner, J. P., Chawner J. P., and Fouts, C. L., "The GRIDGEN 3D Multiple Block Grid Generation System, Volume II: User's Manual," Technical Report WRDC-TR-90-3022, Wright Research and Development Center, Wright Patterson AFB, OH, Feb. 1991.

68 Visbal, V. R., and Gaitonde, D. V., "Very high-order spatially implicit schemes for computational acoustics on curvilinear meshes," Journal of Computational Acoustics, Vol. 9, No. 4, pp. 1259-1286, 2001.

69 C. K. W. Tam, "Advances in Numerical Boundary Conditions for Computational Aeroacoustics," AIAA Paper 97-1774, 1997.

70 Dubeif, Y., and Delcayre, F., "On Coherent-vortex Identification in Turbulence," *Journal of Turbulence*, Vol. 1, No. 11, 2000, pp. 1-22.

71 Mack, L.M., "Transition and Laminar Instability," Jet Propulsion Laboratory Publication 77-15, Pasadena, CA, 1977.

72 Galbraith, M. C., and Miller, J., "Development and Application of a General Interpolation Algorithm," AIAA Paper 06-3854, Jun 2006.

73 Radespiel, R., and Windte, J., "Numerical Simulation of Laminar Separation Bubbles with RANS Solutions," RTO/AVT-104/VKI Lecture Series: Low Reynolds Number Aerodynamics on Aircraft, Brussels, Belgium, Nov 2003.

74 Chang, C., "Langley Stability and Transition Analysis Code (LASTRAC) Version 1.2 User Manual," NASA/TM-2004-213233, Langley Research Center, Hampton, VA, Jun 2004.

Appendix A: Boundary Layer Stability Analysis

To investigate the growth of boundary layer instabilities, the code LASTRAC[74] was used to compute the N-factor growth for both linear and non-linear parabolized boundary layer stability analysis. The e^N transition model indicates transition when the N-factor of the most unstable Tollmien-Schlichting waves reaches a predetermined critical value. The critical N-factor is dependant on many factors such as surface roughness, freestream turbulence intensity, and acoustics to name a few. Typical values for wind tunnels are roughly between 7 and 9, and values can go as high as 12 or 13 for a wing in flight.

N-factor growth for a range of frequencies in Figure A.1 were initially computed from the time-mean solution at 4° angle of attack and Reynolds number $6x10^4$ using both linear and non-linear parabolized stability analysis to estimate the most unstable frequency. Both analysis indicate a most unstable frequency of roughly $F^+ = 9$. While this frequency is not the dominant frequency observed in the velocity energy spectrum shown in Figure 5.8, it is consistent with the peak observed at $F^+ = 9.2$ at $X/C = 0.5$. Given the previously determined transition location, both the linear and non-linear parabolized stability analyses yield an N-factor of roughly 10 at transition. Limited differences between the linear and non-linear parabolized stability analysis indicates that non-parallel effects are not significant in the stability analysis. Hence, the quasi two-dimensional parallel flow assumption of the linear stability analysis is valid.

A comparison of N-factor growth between the LASTRAC analysis and N-factor growth used by XFOIL for a range of N_{crit} values is given in Figure A.2. Here, only the dominant frequencies observed in the velocity fluctuations are included. In comparison with the ILES solution, XFOIL slightly under estimates the growth of the N-factor. In addition, an N_{crit} value

of 10 in XFOIL predicts transition to occur at X/C = 0.59 which is further downstream than the ILES. A consistent transition location at X/C = 0.55 is obtained from XFOIL with an N_{crit} value of 8.

Even though an N_{crit} of 10 predicts transition to occur further downstream, the surface pressure distribution with N_{crit} of 10 is closer to the ILES prediction than an N_{crit} value of 8 as illustrated in Figures A.3 and A.4. Part of the discrepancy can be attributed to how transition is defined. For the ILES solution, transition is assumed to occur when the Reynolds stress in the shear layer reaches a value of 0.1% and exhibits a clear visible rise. However, this occurs slightly further upstream of the sudden recovery in pressure. In contrast, XFOIL uses the transition location as predicted by the e^N method to demarcate the pressure recovery process. However, the ILES computations predict a sharper pressure recovery than XFOIL.

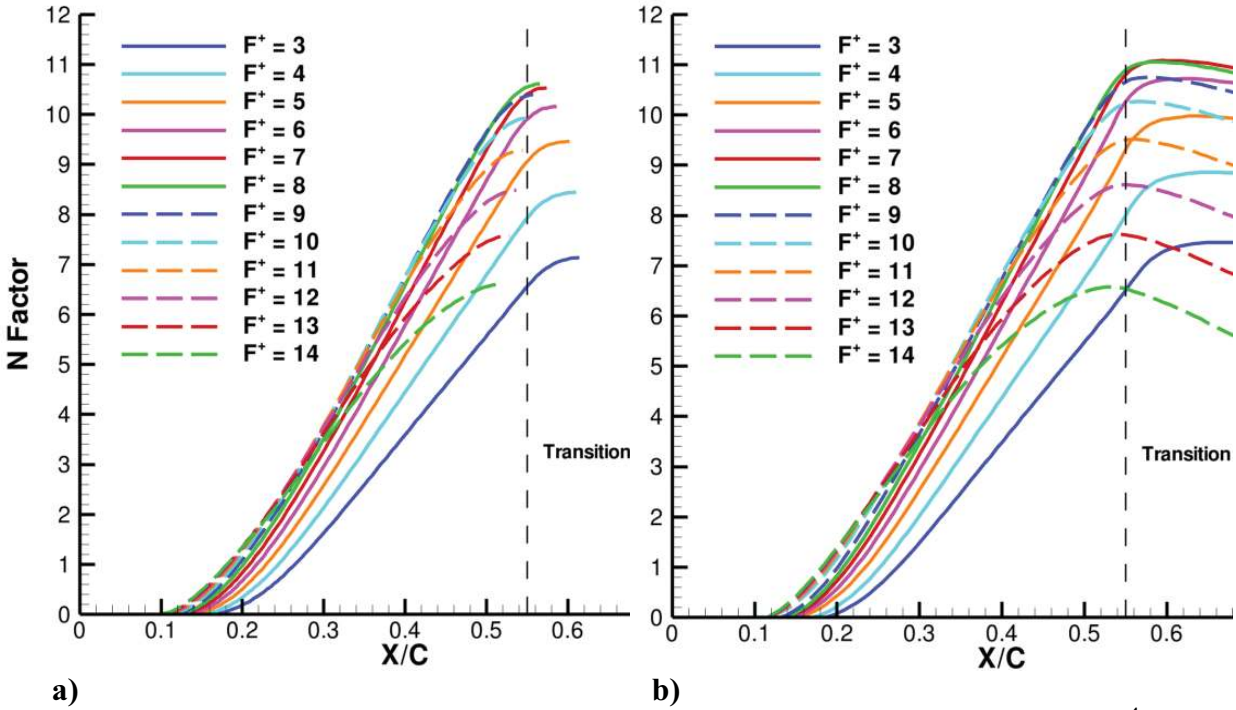

Figure A.1: N-Factor growth rate from stability analysis (α = 4°, Re = 6x10^4)
a) Linear b) Non-linear Parabolized

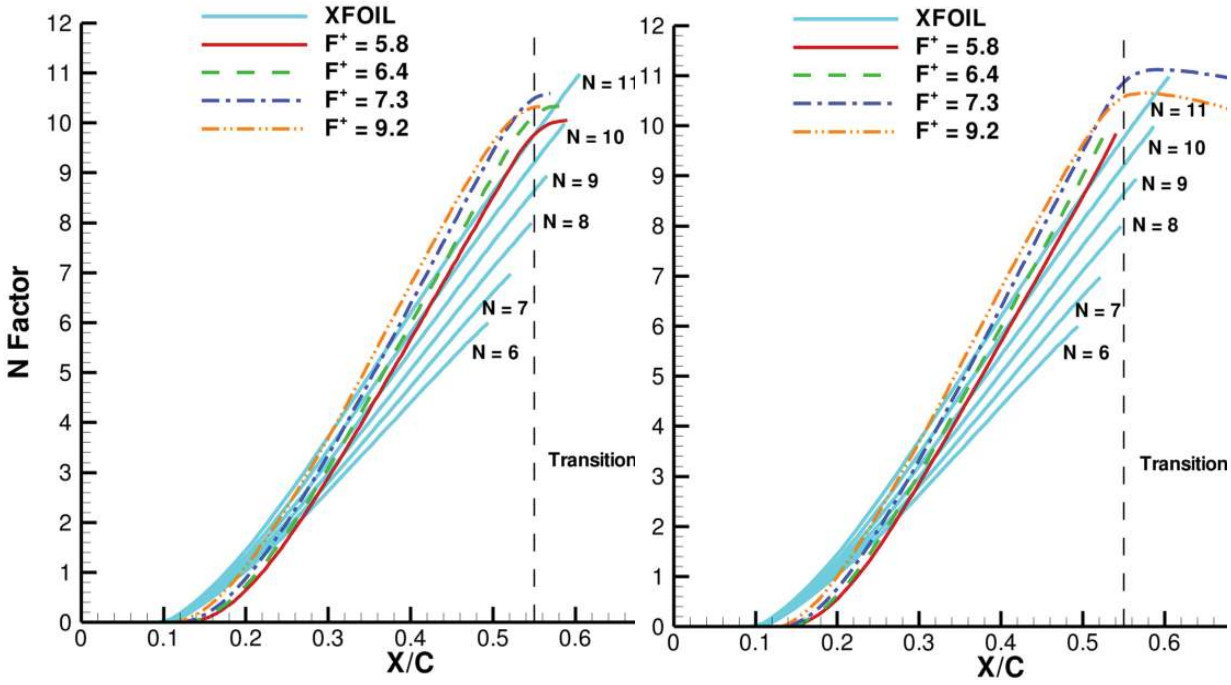

Figure A.2: N-Factor growth rate of dominant frequencies compared with N-factors from XFOIL ($\alpha = 4°$, $Re = 6x10^4$) a) Linear b) Non-linear Parabolized

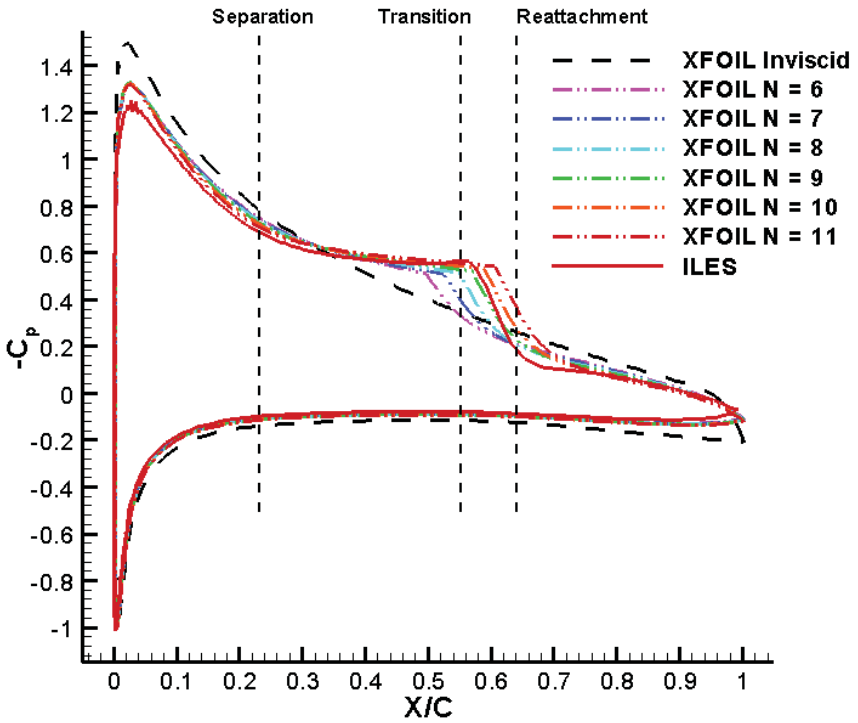

Figure A.3: *Cp* comparison between XFOIL and ILES ($\alpha = 4°$, $Re = 6x10^4$)

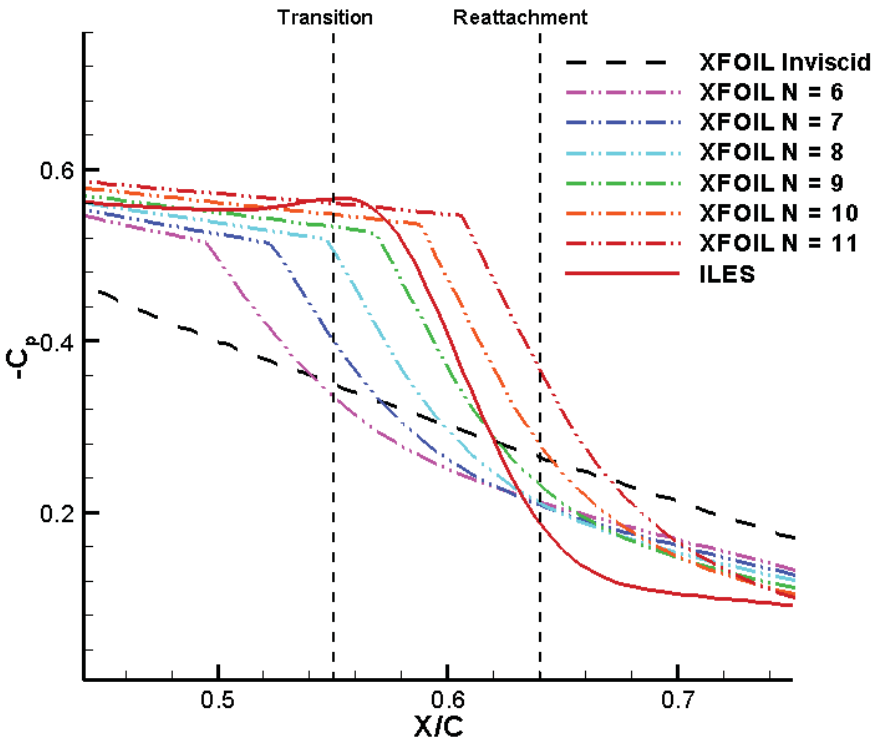

Figure A.4: ***Cp*** **comparison between XFOIL and ILES in the transition regtion ($\alpha = 4°$, $Re = 6x10^4$)**

The most significant differences between the ILES and XFOIL computations are observed in the suction surface skin friction coefficient shown in Figure A.5. While the skin friction coefficients in the laminar and separated region agree well, the XFOIL results lack the drastic drop in skin friction coefficient in the transition region. The abrupt rise is after reattachment is present, but under estimated. Despite these discrepancies, the reattachment location is in agreement with N_{crit} of 10.

A comparison in Figures A.6 and A.7 of displacement and momentum thickness and kinematic shape factor of the boundary layer on the suction surface of the airfoil also indicate a reasonable agreement for N_{crit} of 10. A physical reasoning of N_{crit} is also plausible. Higher N_{crit} values are associated with lower freestream turbulence intensities. Thus, since the ILES

calculation does not include any freestream turbulence intensities, a higher N_{crit} value would expectedly yield better agreement with the ILES computation.

Despite the indication that N_{crit} would be the proper value to prediction transition, a comparison of lift and drag polars for three N_{crit} values in Figure A.8 indicates little difference in lift and drag coefficients up to stall. All three N_{crit} values slightly over predict the lift coefficient and yield different stall angles. Arguably, N_{crit} of 7 gives the correct stall angle of 11°. Post stall the lift is under predicted for all values of N_{crit}. Despite all discrepancies, XFOIL performs remarkably well given the computational costs; XFOIL computations take seconds while the ILES calculations requires weeks on a cluster of computers.

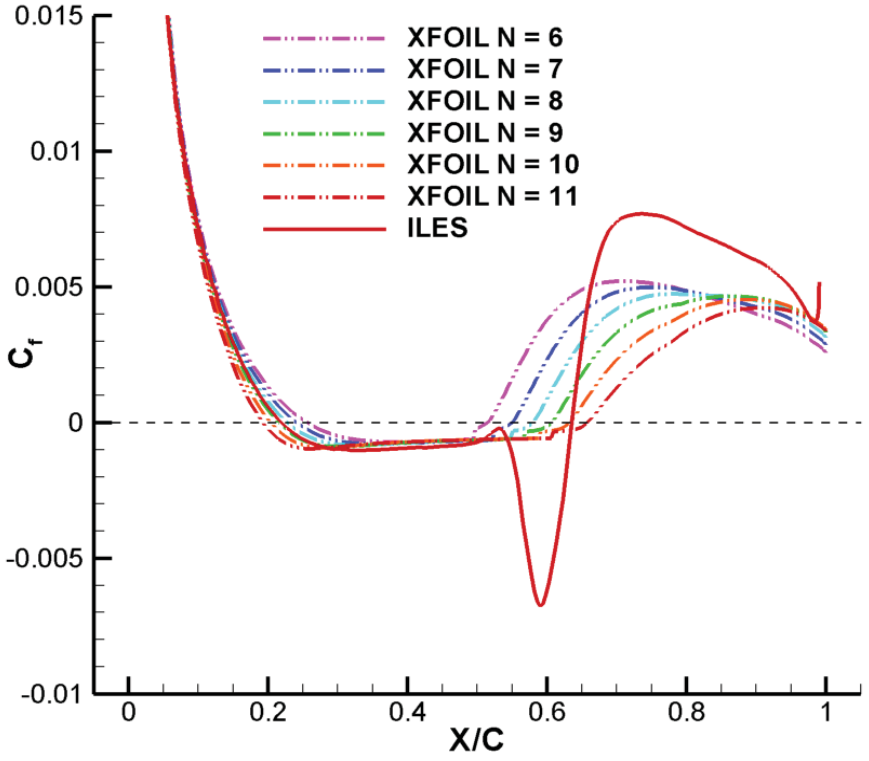

Figure A.5: Sucton surface C_f comparison between XFOIL and ILES ($\alpha = 4°$, $Re = 6x10^4$)

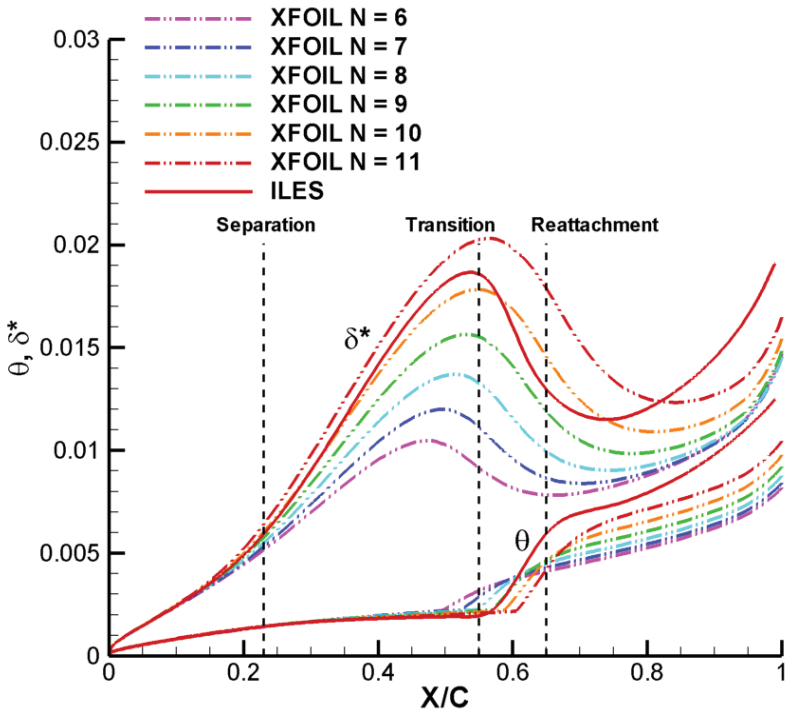

Figure A.6: Displacement (δ^*) and momentum (θ) thickness comparison between XFOIL and ILES ($\alpha = 4°$, $Re = 6x10^4$)

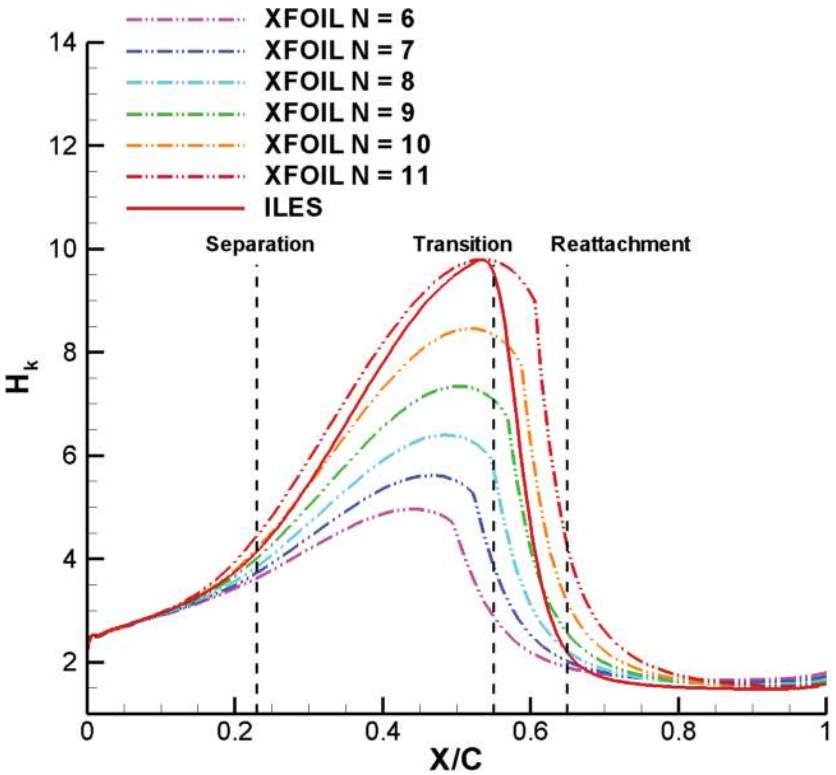

Figure A.7: Kinematic shapefactor comparison between XFOIL and ILES ($\alpha = 4°$, $Re = 6x10^4$)

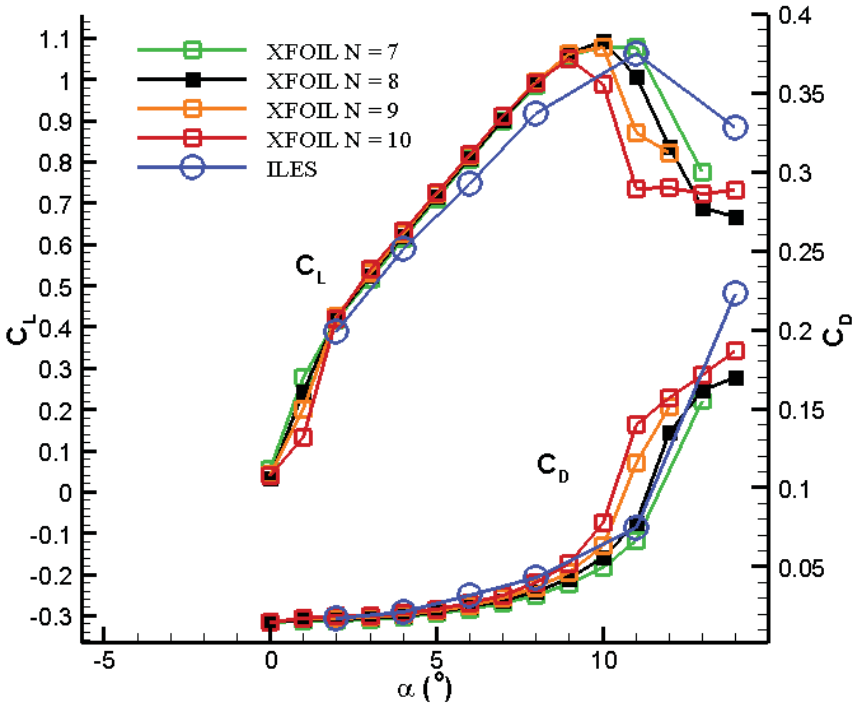

Figure A.8: XFOIL and ILES lift and drag polars

A boundary layer stability analysis using LASTRAC[74] was performed for the two leading edge disturbances. For the lower amplitude, N-factor growth for a range of F^+ values and for the dominant modes observed in the velocity spectra are given in Figures A.9 and A.10 respectively. Similar figures for the higher amplitude disturbance are given in Figures A.11 and A.12. Few differences can be observed between the linear and non-linear parabolized solutions indicating that non-parallel effects are not significant. Consistent with the transition locations moving upstream for both amplitudes, the critical N-factor has decreased from the undisturbed flow. For the lower amplitude disturbance, the critical N-factor has dropped to 5 with the most unstable of roughly $F^+ = 12$. Similarly, the most unstable frequency for the higher amplitude disturbance is roughly $F^+ = 12$, however the critical N-factor has dropped now to roughly 3.5. Finally, the disturbances reduced displacement and momentum thicknesses as show in Figure A.13, and hence a reduction in the shape factor as shown in Figure A.14.

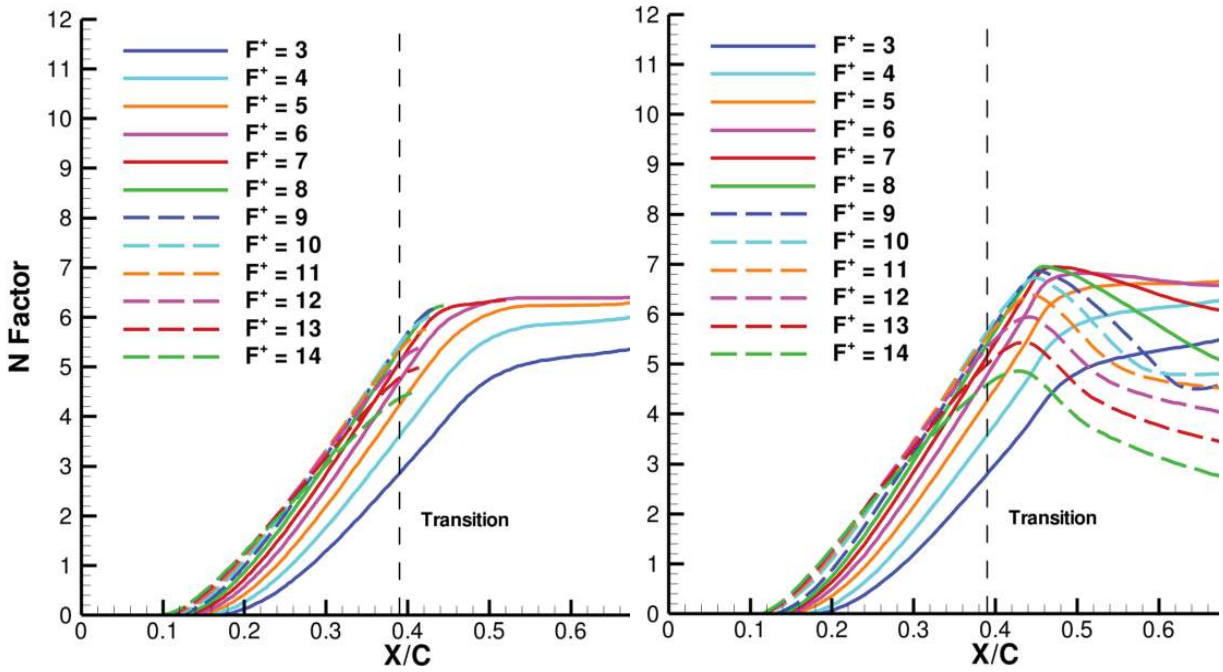

Figure A.9: N-Factor growth rate from stability analysis (A = 0.001)
a) Linear b) Non-linear Parabolized

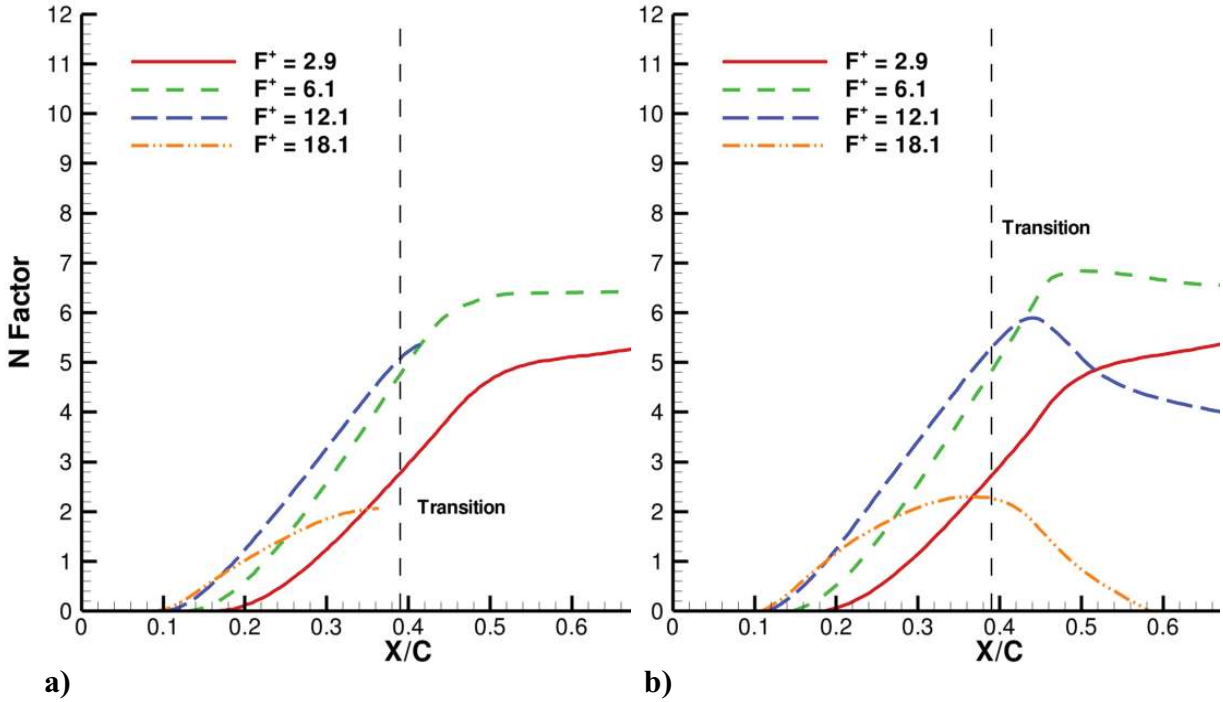

Figure A.10: N-Factor growth rate of dominant frequencies (A = 0.001)
a) Linear b) Non-linear Parabolized

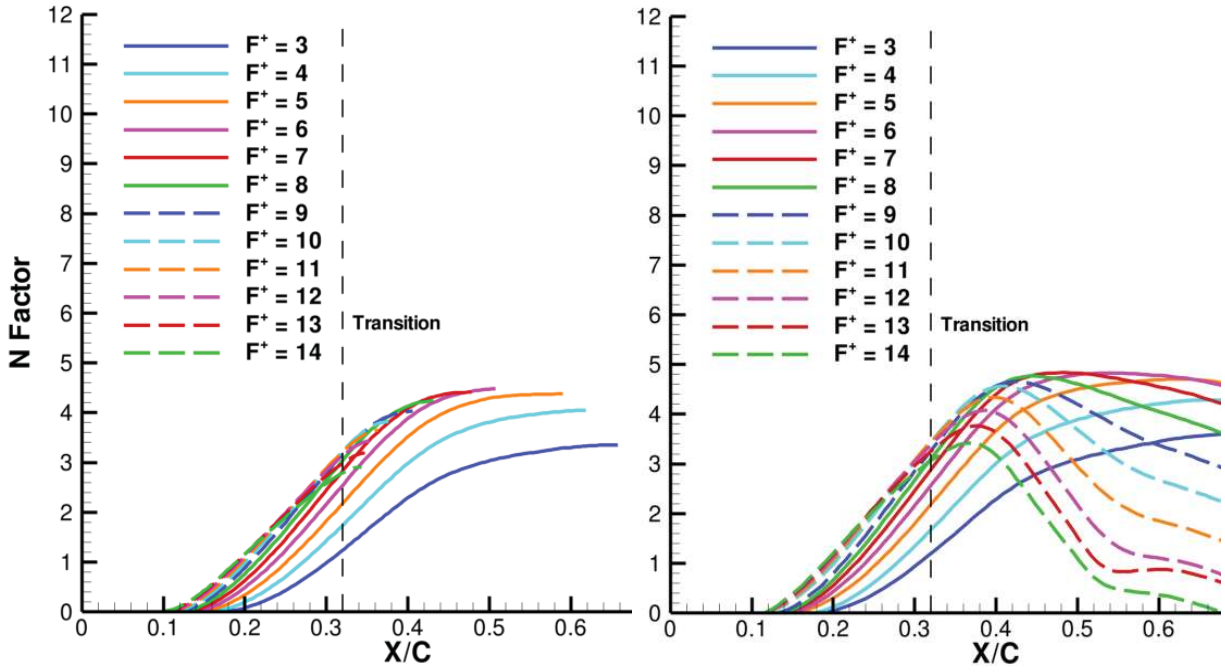

Figure A.11: N-Factor growth rate from stability analysis (A = 0.01)
a) Linear b) Non-linear Parabolized

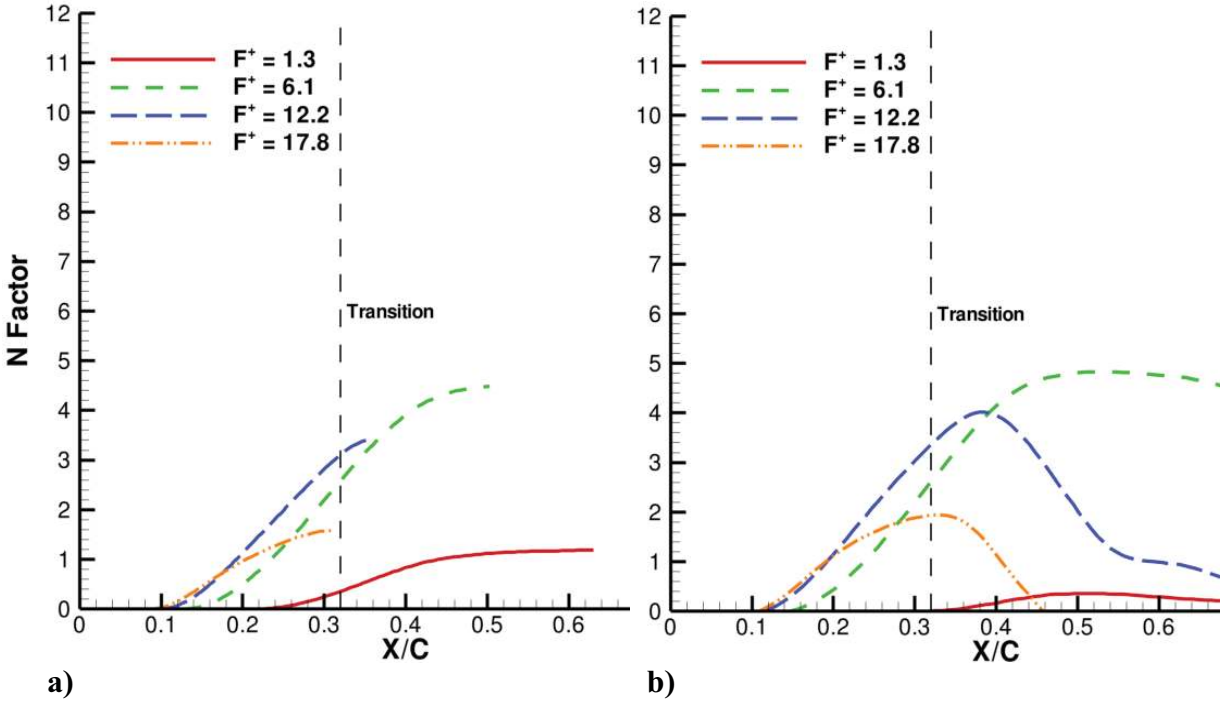

Figure A.12: N-Factor growth rate of dominant frequencies (A = 0.01)
a) Linear b) Non-linear Parabolized

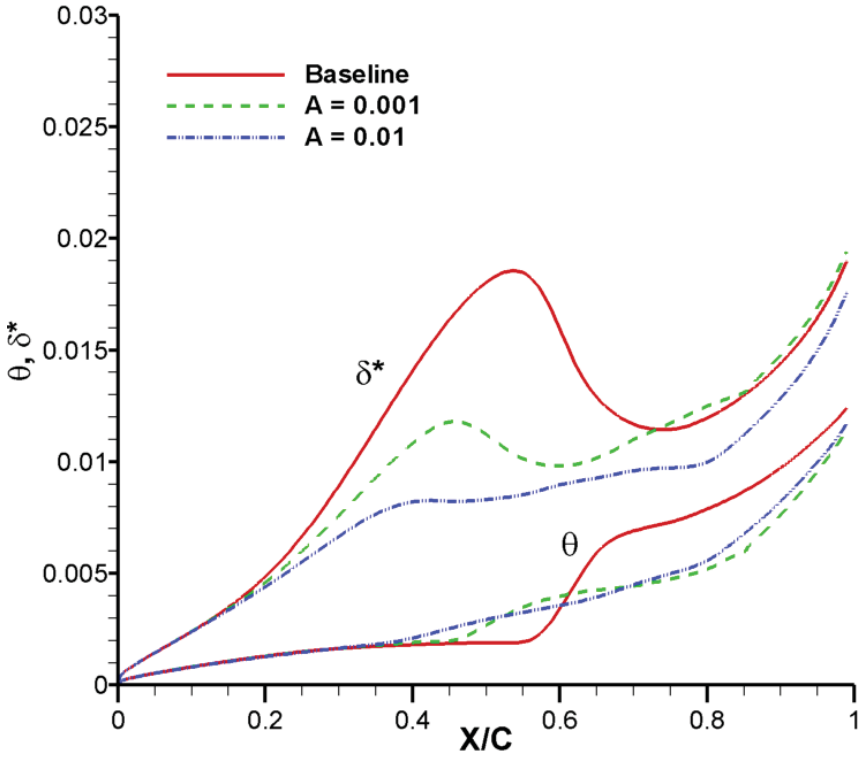

Figure A.13: Bondary layer displacement (δ^*) and momentum (θ) thickness with leading edge disturbance

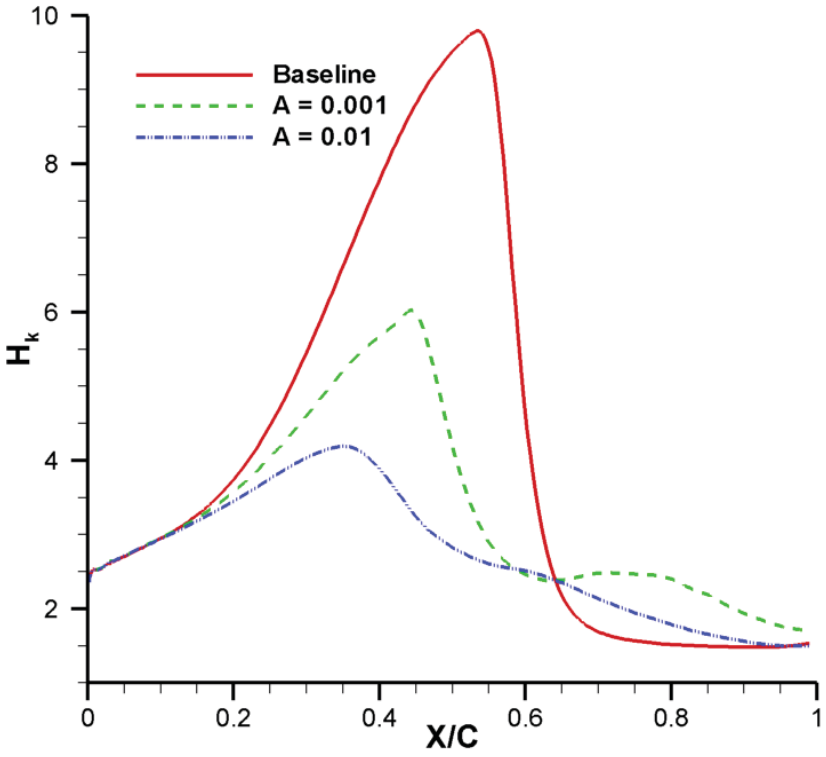

Figure A.14: Bondary layer kinmatic shape factor with leading edge disturbance

Appendix B: Instantaneous Spanwise Vorticity Time Sequences

Time sequences of instantaneous spanwise vorticity are given here for 4° angel of attack at Reynolds number $6x10^4$. In addition, time sequences for of instantaneous spanwise vorticity with the leading edge disturbance present are given. For detailed discussions regarding these time sequences see sections 5.1 and 5.4.

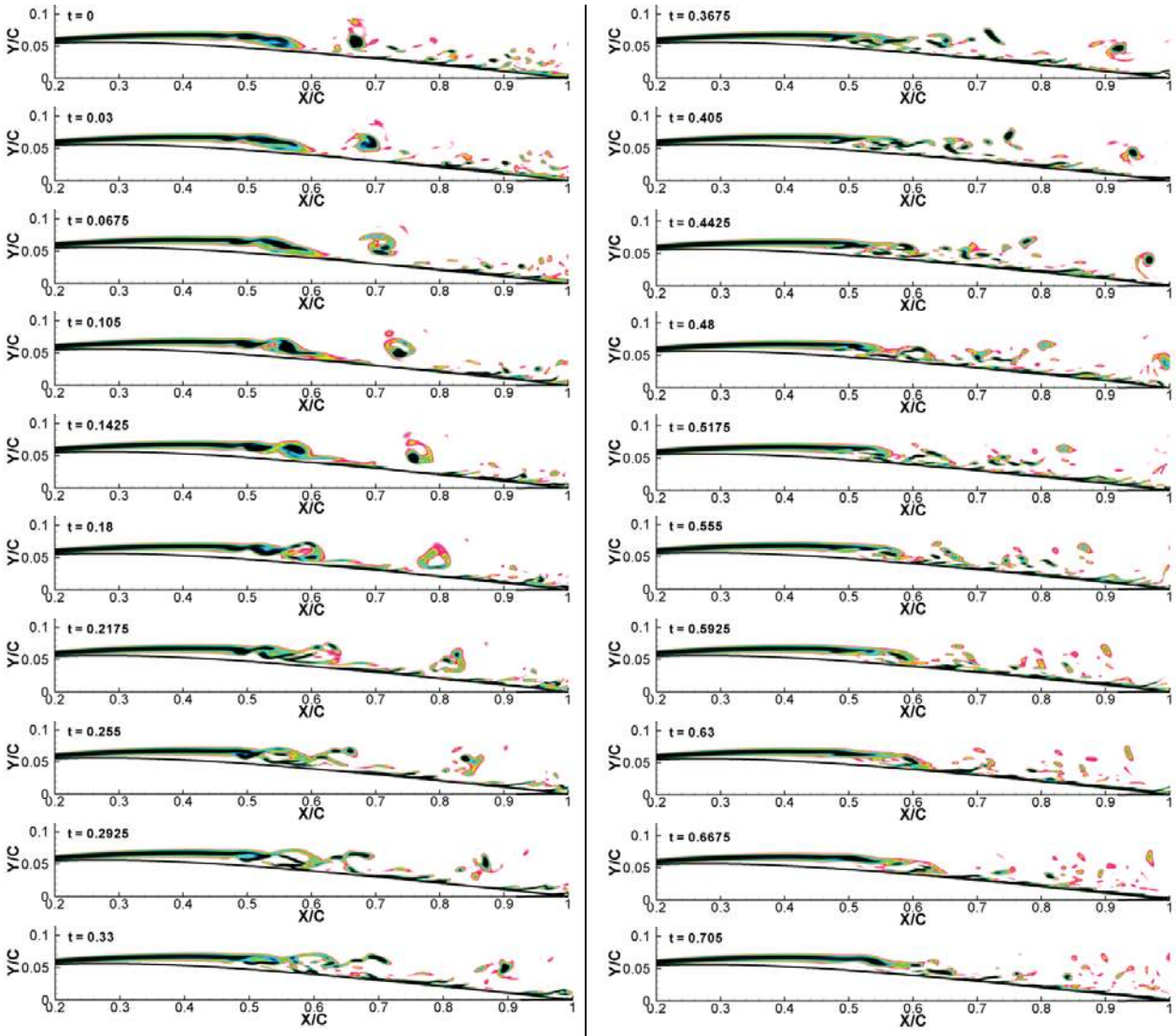

Figure B.1: Instantanous contours of spanwise vorticity component ($\alpha = 4°$, $Re = 6x10^4$)

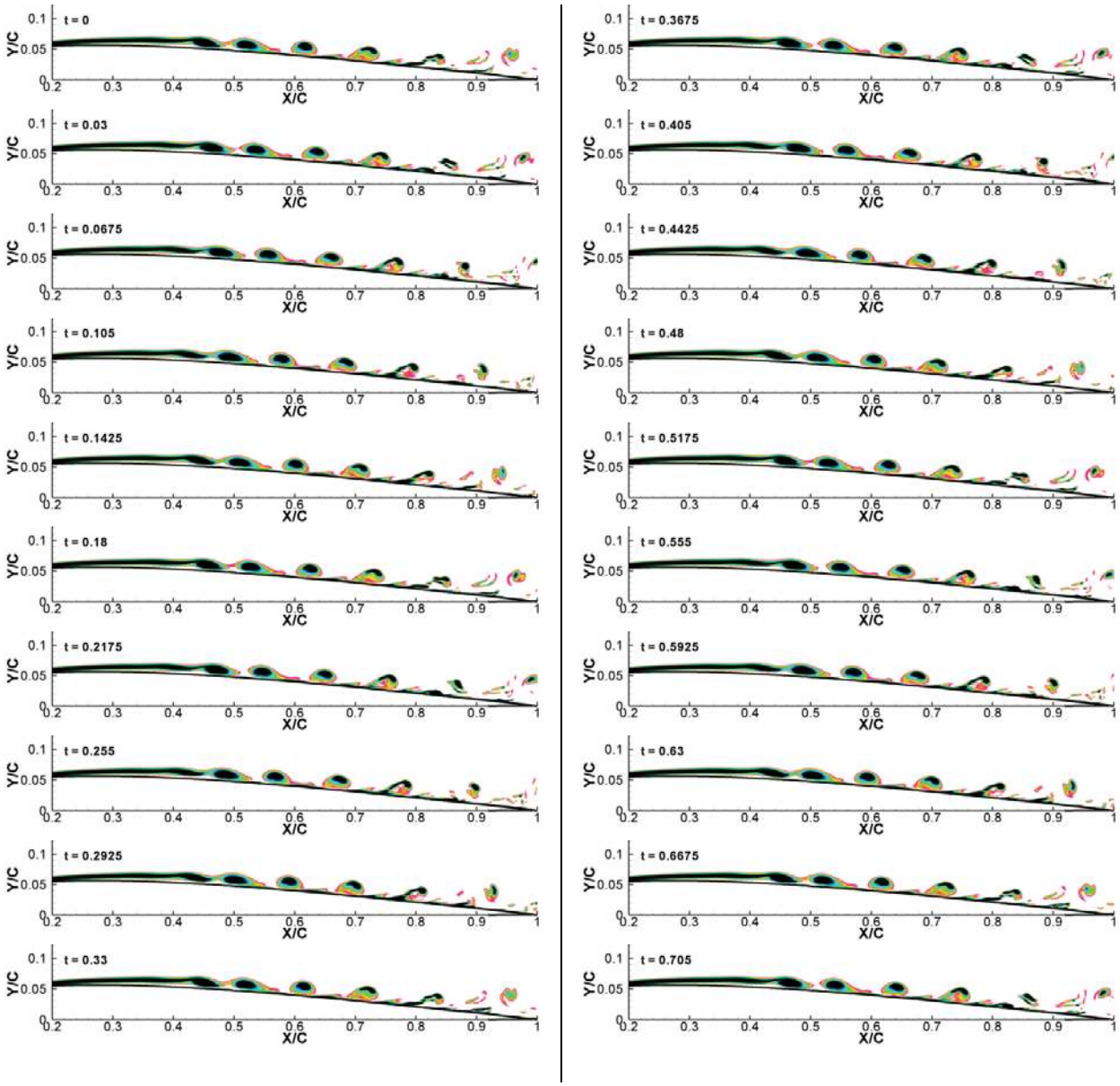

Figure B.2: Instantanous contours of spanwise vorticity component with leading edge disturbance ($\alpha = 4°$, $Re = 6x10^4$, $A = 0.001$)

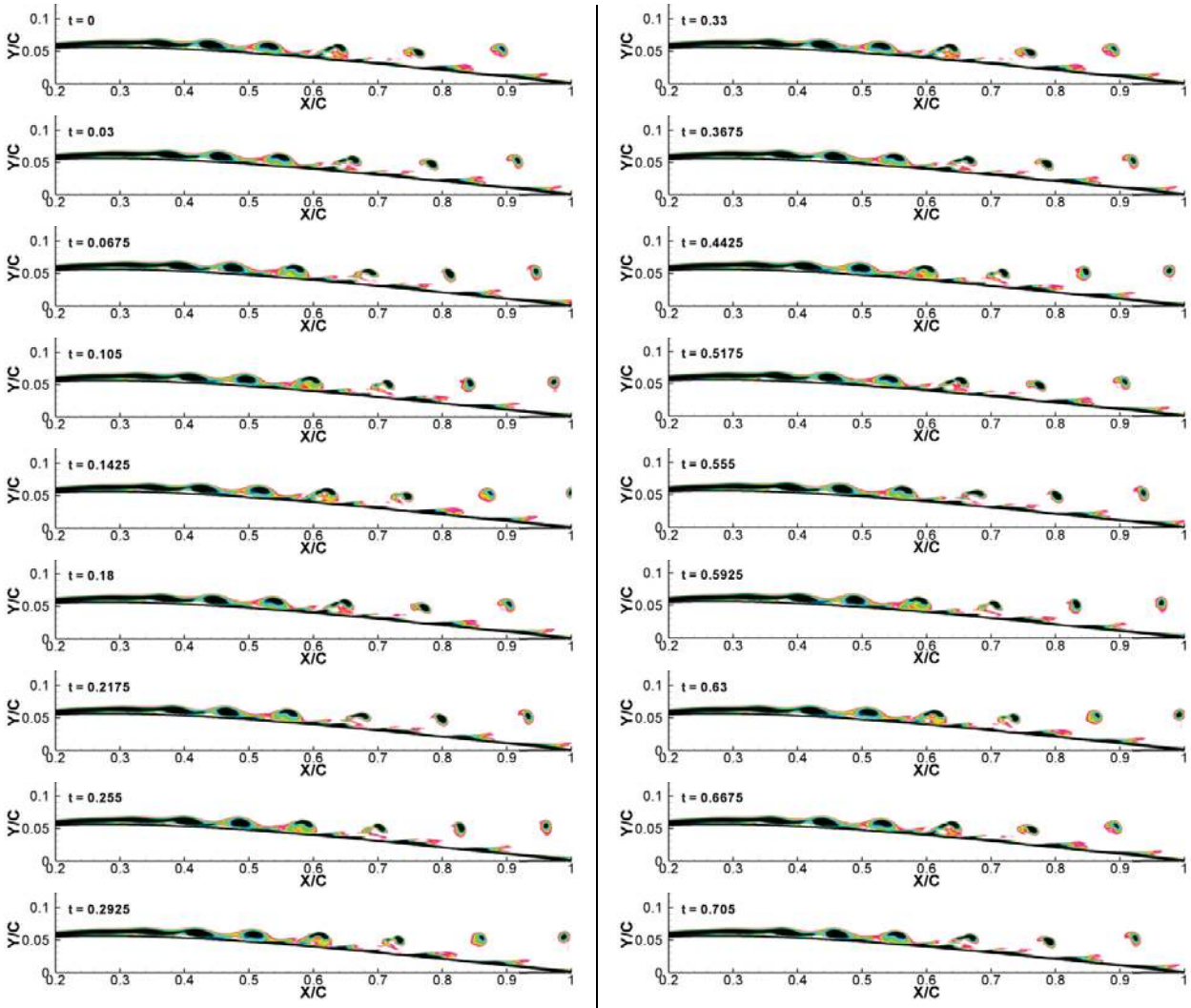

Figure B.3: Instantanous contours of spanwise vorticity component with leading edge disturbance ($\alpha = 4°$, $Re = 6x10^4$, $A = 0.01$)